Vapor Phase Synthesis of Smart Membranes for Macromolecule Separation Applications

by

Ali Tufani

Submitted to the Institute of Engineering and Natural Sciences

in partial fulfillment of

the requirements for the degree of

Doctor of Philosophy

Sabancı University
January 2018

Vapor Phase Synthesis of Smart Membranes for Macromolecule Separation Applications

Approved by:

Assoc. Prof. Dr. Gozde Ozaydin Ince
(Thesis Advisor)

Prof. Dr. Canan Atilgan

Prof. Dr. Ismail Koyuncu

Assoc. Prof. Dr. Gullu Kiziltas Sendur

Assoc. Prof. Dr. Lokman Uzun

Date of approval: 10 / 01 / 2018

Vapor Phase Synthesis of Smart Membranes for Macromolecule Separation Applications

Ali Tufani

MAT, PhD Thesis, 2018

Thesis Supervisor: Assoc. Prof. Gozde Ozaydin Ince

Keywords: Initiated Chemical Vapor Deposition (iCVD), Stimuli Responsive Membranes, Macromolecule Separation

ABSTRACT

Today, state-of-the-art synthesis and advanced purification at a reasonable price and in a short time is necessary to reach the high purity of molecules in chemicals and biochemical manufacturing industry. One of the most important methods is to use functional polymers in order to increase the permeability and selectivity of commonly used membranes. Smart membranes change their physicochemical properties in response to changes in their environment such as pH, temperature, ionic strength, light, electric and magnetic fields. The main goal of this thesis is to design and prepare different types of separation membranes via vapor polymerization methods to improve the permeability and selectivity of the membranes. Stimuli responsive polymers are used to functionalize the membranes for triggered control of permeation and tuning of the release kinetics. In the first chapter, nonporous, ultra-thin large area free-standing functional membranes are developed. The mesh size is tuned to control the permeability and selectivity of the membranes for separation of model dye molecules with different size and polarity. In the second part, hybrid membranes are produced by modifying AAO template pores using smart polymers. Shape, size and charge interactions between the membranes and macromolecules are the key factors in controlling the membrane selectivity via changing the membrane pore size at different pH values. Double-sided Janus membranes with two different pH responses are developed as gating membranes to control the flow of the protein molecules through the membrane. The key-shaped non-conformal coatings allow to control protein diffusion by blocking, delaying and releasing protein depending on the acidity of the medium. Furthermore, the shape of the nanochannels is another critical factor in separation of proteins by membranes. Membranes with symmetric

cylindrical and asymmetric conical functionalized nanochannels are developed to control the protein flux and separation. Finally, negatively charged and neutral membranes are fabricated to separate two proteins with the same size but different charges using pH responsive polymers.

Makromolekül Ayırma Uygulamaları için Buhar Fazında Sentezlenmiş Akıllı Membranlar

Ali Tufani

MAT, Doktora Tezi, 2018

Tez Danışmanı: Doç. Dr. Gozde Ozaydin Ince

Anahtar Kelimeler: Başlatılmış Kimyasal Buhar Biriktirme (iCVD), Uyarıya Duyarlı Membranlar, Makromolekül Ayrıştırma

Özet

Günümüzde, kimyasal ve biyokimyasal üretim sektöründe yüksek saflıkta moleküller elde etmek için maliyeti düşük ve kısa sürede sonuç veren ileri teknoloji sentez ve gelişmiş arıtma yöntemleri gerekmektedir. En önemli metotlardan biri, membranlarda geçirgenliği ve seçiciliği arttırmaya yönelik fonksiyonel polimerler kullanmaktır. Akıllı membranlar pH, sıcaklık, iyonik kuvvet, ışık, elektrik alan ve manyetik alan gibi çevresel değişimlere karşı fizikokimyasal özelliklerini değiştirirler. Bu çalışmada, membranların geçirgenliğini ve seçiciliğini arttırmak adına, buhar biriktirme yöntemleri ile farklı ayrıştırma membranlarını tasarlamak ve üretmek hedeflenmiştir. Uyarıya duyarlı polimerler, geçirgenliği kontrol etmek ve salınım kinetiğini ayarlamak amacıyla membranların fonksiyonlanması için kullanılmıştır. Birinci bölümde, gözeneksiz, aşırı-ince, geniş alanlı, desteksiz fonksiyonel membranlar geliştirilmiştir. Farklı boyut ve kutupsallıktaki model boya moleküllerinin ayrışmasında, membran geçirgenliği ve seçiciliğini kontrol etmek için gözenek boyutu ayarlanmıştır. İkinci kısımda, hibrit membranlar, AAO şablonlu gözeneklerin akıllı polimerler kullanılarak modifiye edilmesi ile üretilmiştir. Membranlar ve makromoleküller arası şekil, boyut ve yük etkileşimleri, farklı pH değerlerindeki membran gözenek boyutu kontrolü ile elde edilen membran seçiciliğinde en önemli faktörlerdir. İki farklı pH yanıtlı, çift taraflı Janus membranları, protein moleküllerinin membrane boyunca akışının kontrolü için geçit membranı olarak geliştirilmiştir. Anahtar şekilli konformal olmayan kaplamalar, protein difüzyonunun asit ortamına bağlı olarak protein engellenmesi, geciktirilmesi ve salınımı ile kontrol edilmesini sağlamıştır. Ek olarak, nanokanalların şekli, proteinlerin membranlar ile ayrıştırılmasında bir diğer kritik faktördür. Simetrik silindirik ve asimetrik konik şekilli fonksiyonlandırılmış nanokanallar,

protein akışı ve ayrıştırılmasını kontrol etmek amacıyla geliştirilmiştir. Son olarak, eksi yüklü ve yüksüz membranlar, aynı boyutlu fakat farklı yüklü iki proteinin ayrıştırılması için pH duyarlı polimerler ile üretilmiştir.

To My Parents

Marzieh Hamidian and Safar Ali Tufani

Acknowledgements

My first and foremost acknowledgement should and must go to my advisor, Dr. Gozde Ozaydin Ince, for her endless source of support and wisdom innovative ideas. Her endless reserves of patience kept me motivated throughout the long learning curves of the initial years. I was so lucky to work with her. Not only I learned the path to be a good scientist from her but also, she taught me how to educate and teach. I am grateful to my thesis committee members, professor Canan Atilgan, professor Ismail Koyuncu, Dr. Gullu Kiziltas Sendur and Dr. Lokman Uzun. I also wish to express my sincere gratitude to lab technicians Turgay Gonul, Bulent Koroglu, Serkan Bostan and Onur Serbest for their support and help during my time at Sabanci. I would like to thank my other colleague at Sabanci University who shared their knowledge with me as well as hands-on training in lab. My past and present group mates, Ridvan Demiryurek, Efe Armagan, Mehmet Can Zeybek, Omid Moradi and Sezin Sayin. I would like to acknowledge the past and present professors and staff in Materials Science and Nanoengineering group and SUNUM at Sabanci University for their continuous help and support. I was also lucky enough to know many people from other departments and groups. To all of my friends and colleagues your kindness will never be forgotten. Lastly, I thank my family Safar Ali, Marzieh, Fariba, Parivash, Parinaz and Maryam. I will always look up to the examples you set for me and am immensely thankful for your unwavering support and unconditional love throughout this journey.

TABLE OF CONTENTS

CHAPTER 1. INTRODUCTION AND BACKGROUND 1

1.1. Separation by the Membrane 1

1.2. Chemical Vapor Deposition (CVD) 5

1.3. Initiated Chemical Vapor Deposition (iCVD) 6

CHAPTER 2. EXPERIMENTAL METHODS 10

2.1. Membrane Fabrication 10

2.1.1 Deposition Set-up 10

2.1.2 Deposition Procedures 11

2.2. Material Characterization 13

2.2.1. Optical methods 13

2.2.1.1. Fourier Transform Infrared Spectroscopy (FTIR) 13

2.2.1.2. Ultraviolet–visible Spectroscopy (UV-vis) 13

2.2.1.3. Spectroscopic Ellipsometry 14

2.2.2. Structural methods 14

2.2.2.1. Scanning Electron Microscopy (SEM) and Energy-Dispersive X-Ray Spectroscopy (EDS) 14

2.2.2.2. Atomic Force Microscopy (AFM) 15

2.3. Membrane Performance Methods 16

2.3.1. Permegear Side-bi-side Diffusion Cells 16

2.3.2. Homemade Side-bi-side Diffusion Cells 17

2.3.3. High Pressure Permeation 18

CHAPTER 3. FREE-STANDING MEMBRANE 20

3.1. Introduction 20

3.2. Experiment Procedure 20

3.2.1. Membrane Preparation 20

3.2.1.1. Polymer Coating Characterization 21

3.2.1.2. Permeation Experiments 21

3.3. Results and Discussion 22

CHAPTER 4. HYBRID PH RESPONSIVE MEMBRANES 31

4.1. Introduction 31

4.2. Experimental Methods 31

4.2.1. pH Responsive Membrane Preparation 31
4.2.2. Charging of Membranes 32
4.2.3. Membrane Characterization 32
4.3. Results and Discussion 34
CHAPTER 5. JANUS MEMBRANES 47
5.1. Introduction 47
5.2. Experimental Methods 47
5.2.1. Membrane Preparation 47
5.2.2. Membrane Characterization 48
5.3. Results and Discussion 49
CHAPTER 6. SYMMETRIC-ASYMMETRIC MEMBRANES 61
6.1. Introduction 61
6.2. Experimental Methods 61
6.2.1. pH-responsive Membrane Preparation 61
6.2.2. Membrane Characterization 62
6.2.3. Permeation Experiments 62
6.3. Results and Discussion 62
CHAPTER 7. HYBRID AUNPS ATTACHED MEMBRANES 71
7.1. Introduction 71
7.2. Experimental Methods 71
7.2.1. Membrane Depositions 71
7.2.2. Negatively Charged AuNPs 72
7.2.3. Charging of Membranes 72
7.2.4. Membrane Characterization 72
7.2.5. Diffusion Experiments 72
7.3. Results and Discussion 73
CHAPTER 8. CONCLUSIONS 82
Bibliography 83

LIST OF FIGURES

Figure 1.1. Different types of separation via the membranes 2
Figure 1.2. Different types of stimuli responsive polymers according to external stimuli..... 3
Figure 1.3. Nylon membranes treated with pDVB were tested for LEP using a series of ethanol/water solutions..... 5
Figure 1.4. a) Schematic of the iCVD reactor and typical operating parameters b) Depiction of the iCVD mechanism. c) Free radical polymerization scheme..... 7
Figure 1.5. (a) Schematic of the quantities involved in an analysis of the sticking probability. (b) An impinging radical (i) can react with an adsorbed monomer if it strikes it directly (ii–a). If not, it will desorb back to the vapor phase within tens of microseconds (ii–b)..... 9
Figure 2.1. Picture of the iCVD system: a) precursor delivery section including jars, needle valve, MFC and piping b) reactor chamber with pressure gauge, mass flow controller, substrate temperature controller and He/Ne laser c) thermocouple controller panel d) filament part including array wrapped around the ceramics and thermocouple 12
Figure 2.2. Incidence of accelerating electron beam on the sample and generation of secondary electrons, back scattered electron and characteristic X-rays..... 15
Figure 2.3. Diagram of crucial AFM components. (a) shows a representation of the tip; it contains a probe straddled on a cantilever, and in (b) the cantilever easily bends even with a slight force on the tip 16
Figure 2.4. Permegear side-bi-side diffusion cell with heater/circulator ports, donor and receptor chambers, stir bars, cell clamp, sampling ports and tension knob. The hoses are used to guide water flow from heater/circulator ports to control the temperature..... 17
Figure 2.5. Homemade diffusion cell a) donor and receptor chambers, stir bars b) sampling ports and tension knob. c) the cell on the stirrer inside the cold room 18
Figure 2.6. a) High pressure Sterlitech cells with stirrer and Nitrogen tube b) membrane glued to the plastic holder c) Schematic picture of high pressure permeation and sample collection..... 19
Figure 3.1. (a) Free-standing p(HEMA) membrane and the white plastic frame surrounding it are shown. (b) Side-bi-side diffusion cell used for permeation tests is shown..... 22
Figure 3.2. FTIR spectra of the deposited uncrosslinked, high crosslinked (HX) and low crosslinked (LX) p(HEMA) membranes. The peaks representing the C=O stretching vibrational modes are shaded with horizontal lines, while the peaks representing the O-H vibrational modes are shaded with diagonal lines 23
Figure 3.3. (a) SEM image of the free-standing HX p(HEMA) membranes before the diffusion tests. (b) AFM surface images of the LX and HX p(HEMA) membranes before the diffusion tests. The RMS roughness of the samples is less than 5 nm 25
Figure 3.4. Plot of Eq. (5) where y(t) = -(V/A) *ln(1-c(t)/c (0)) showing the change in dye concentration as a function of time for low and high crosslinked samples tested with AY and Phl dyes. The slope of the plots gives the permeability coefficient, P..... 27
Figure 3.5. Plot of eq. (5) as a function of time showing the selectivity of the LX membranes tested with AY and PADPA dyes simultaneously 30
Figure 4.1. Schematic of the pH responsive membrane preparation. The uncoated AAO template is put on the stage in the iCVD chamber where the deposition takes place..... 32

Figure 4.2. FTIR spectra of the p(MAA-co-EGDMA) coating on the AAO. Spectra of p(MAA) and p(EGDMA) are also shown for comparison. The doublet carbonyl band of the copolymer film confirms copolymerization of MAA and EGDMA monomers 35
Figure 4.3. SEM images of cross-section of (a) polymer coated and (b) uncoated AAO and top-view of (c) polymer coated and (d) uncoated AAO. Polymer coating on the pore walls is visible in the cross-sectional view, confirming the penetration of the polymer into the AAO membrane 36
Figure 4.4. Pore size distribution of (a) uncoated AAO and (b) polymer coated AAO template as obtained from SEM images. The average pore size of the uncoated AAO is calculated to be as 110±13 nm, whereas the coated template has an average pore size of 85±20nm with a wider distribution of pore sizes 37
Figure 4.5. Water permeabilities of uncoated AAO template and p(MAA-co-EGDMA) coated AAO at pH 3 and pH 9 measured at different pressures. Highest permeabilities are obtained with the uncoated template due to larger pore size. On the other hand, for the coated templates permeabilities decreased at pH 9 compared to pH 3, due to the swollen pH responsive p(MAA-co-EGDMA) at high pH, decreasing the effective pore size 37
Figure 4.6. DLS analysis of the feed and permeate solutions at (a) pH 3 and (b) pH 9. The average size of permeates at pH 3 is larger than that at pH 9, where the pore openings are narrower due to the swollen polymer 39
Figure 4.7. Permeate flux of PAA solution as a function of time. The compact structure of PAA at pH 3 facilitates faster permeation, increasing the flux in uncoated membranes. Flux is reduced at coated membranes due to narrower pores. The further decline in the flux at pH 9 is due to the swollen polymer inside the pores 40
Figure 4.8. Concentration of PAA on the permeate side as a function of time. Diffusion of the PAA molecules is faster through the uncoated membranes, fastest diffusion is observed at pH 3 due to the compact structure of the PAA. In coated membranes, in addition to the PAA structure, polymer swelling also affects the permeation, with faster diffusion observed at pH 3 compared to pH 9 41
Figure 4.9. FTIR spectra of the p(MAA-co-EGDMA) film and p(MAA-co-EGDMA) film functionalized with -GO-NH_2 groups. The bands at 1609 cm^{-1} and 1512 cm^{-1} are attributed, respectively, to the stretching of C=C bond present in GO and bending vibrations of N-H groups, confirming successful functionalization of the surface with GO-NH_2 groups 42
Figure 4.10. Permeate flux of BSA solution as a function of time. The lowest flux was obtained with the polymer coated membranes at pH 3 as opposed to pH 9, indicating the adsorption of positively charged BSA on the membrane at pH 3 which leads to clogging of the pores. Introducing positive charges to the membrane with the -GO groups, leads to increased flux at pH 3 due to the electrostatic repulsion between BSA and the polymer. The hydrophilic nature of the -GO groups at pH 9 dominates the permeation mechanisms, resulting in higher flux values for GO functionalized membranes compared to unfunctionalized, overcoming the electrostatic interactions 43
Figure 4.11. BSA concentration in the permeate side as a function of time obtained from diffusion experiments. For both polymer coated AAO and GO functionalized AAO, concentration increase of BSA is similar at pH 3 and pH 9, indicating the contribution of other factors 45
Figure 5.1. FTIR spectra of the p(4VP-co-EGDMA) and p(MAA-co-EGDMA) thin films coated on different sides of the AAO membranes 49
Figure 5.2. SEM images of the cross section of the Janus membranes with p(4VP-co-EGDMA) coatings at different degrees of conformality. Highly non-conformal coatings (a,b) are obtained at P_m/P_{sat} values of

0.33, whereas conformal coatings (c) are obtained at P_m/P_{sat} of 0.16. For key-hole structures (d,e,f) deposition is performed at P_m/P_{sat} value of 0.23 51
Figure 5.3. (a) SEM image of the cross section of Janus membrane, showing p(4VP-co-EGDMA) coating on side II. (b) Al and C amount within the pores as a function of depth obtained from the EDS analyses, indicating the relative amount of polymer on pore walls. (c) Fit of Equation (3) (straight line) to data (squares) obtained from SEM images 52
Figure 5.4. Schematic of the Janus membrane composed of AAO template with non-conformal coatings of p(MAA-co-EGDMA) on side I and p(4VP-co-EGDMA) on side II. The membrane is placed in a diffusion cell with BSA in the feed side (A) and PBS in the permeate side (B) 54
Figure 5.5. Change in the cumulative BSA concentration as a function of time on the feed and the permeate sides when the pH of the feed and permeate sides are 9 and 9, respectively. The swollen polymer on side I blocks the protein molecules from entering the membrane 55
..... 56
Figure 5.6. Change in the cumulative BSA concentration as a function of time on the feed and the permeate sides when the pH of the feed and permeate sides are 3 and 3, respectively. The protein molecules are hindered from leaving the membrane due to swollen polymer on side II 56
Figure 5.7. Change in the cumulative BSA concentration as a function of time on the feed and the permeate sides when the pH of the feed and permeate sides are 9 and 3, respectively. Swollen polymers on both sides of the membrane close the pore openings, trapping the protein molecules inside 57
Figure 5.8. Change in the cumulative BSA concentration as a function of time on the feed and the permeate sides when the pH of the feed and permeate sides are 9 and 9, respectively. Upon pH change on the permeate side to 9, p(4VP-co-EGDMA) on side II collapses, unblocking the protein molecules which then diffuse to the permeate side 58
Figure 5.9. Pictures of the diffusion experiments performed with the rose bengal dye in side-by-side diffusion cell set-up. (a,b) Experiments performed at pH 9/pH 9 on both feed and permeate sides show there is leakage after 18 hours (b). (c,d) Experiments performed at pH 3/pH3 show that the membrane could successfully block the molecules for 24 hours (d). (e,f) Experiments performed at pH 9/pH 3 where both ends were open show that the concentration of molecules on the permeate side reached 0.04 g/L. (a,c,e) Pictures of the diffusion cells at the beginning of the experiments 59
Figure 6.1. FTIR spectra of the p(MAA-co-EGDMA) coating on Si wafer 63
Fig 6.2. SEM images of hybrid membranes a) bottom view of asymmetric AAO template b) top view of asymmetric AAO template c) symmetric AAO template deposited with p(MAA-co-EGDMA) conformally
..... 64
Figure 6.3. LYZ diffusion through the symmetric and asymmetric membrane at pH3 65
Figure 6.4. Equivalent circuit for a) the symmetric b) the asymmetric membranes 66
Figure 6.5. Hb diffusion through the symmetric and asymmetric membrane at pH3 67
Figure 6.6. LYZ diffusion through the symmetric and asymmetric membrane at pH6.8 68
Figure 6.7. Hb diffusion through the symmetric and asymmetric membrane at pH6.8 69
Figure 6.8. LYZ diffusion through the symmetric and asymmetric membrane at pH6.8 in mixed LYZ and Hb 70
Figure 7.1. Size distribution and zeta potential of AuNPs. 73
Figure 7.2. FTIR spectra of the p(NIPAAm-co-EGDMA) coating on AAO template 74
Figure 7.3. SEM image of the p(NIPAAm-co-EGDMA) coating on AAO template and attached AuNPs on a) the membrane top b) large scale the membrane top c) the walls of membrane pores 75

Figure 7.4. EDS analysis of the membrane. Carbon, aluminum, oxygen and gold distribution in the membrane..... 75
Figure 7.5. Negatively charged citrate-capped AuNPs electrostatically attached to p(NIPAAm-co-EGDMA) 76
Figure 7.6. Single diffusion of Hb and HSA through p(NIPAAm-co-EGDMA) and p(NIPAAm-co-EGDMA)-Au- at pH 3 77
Figure 7.7. Water permeability of uncoated AAO template, p(NIPAAm-co-EGDMA) coated AAO and p(NIPAAm-co-EGDMA)-Au- coated AAO..... 79
Figure 7.8. Single diffusion of Hb and HSA through p(NIPAAm-co-EGDMA) and p(NIPAAm-co-EGDMA)-Au- at pH 9 79
Figure 7.9. Mixed diffusion of Hb and HSA through p(NIPAAm-co-EGDMA) and p(NIPAAm-co-EGDMA)-Au- a) at pH 4.7 b) at pH6.8 80

LIST OF TABLES

Table 3.1. Deposition parameters and the crosslink ratios of the iCVD deposited p(HEMA) free-standing films are given..... 23
Table 3.2. Permeability and diffusion coefficients of model dyes tested on membranes with different mesh sizes..... 28

ABBREVIATIONS

4VP: 4 vinylpyridine

AAO: Aluminum Anodic Oxide

AFM: Atomic Force Microscopy

AuNP: Gold Nanoparticle

AY: Alizarin Yellow

BSA: Bovine Serum Albumin

CVD: Chemical Vapor Deposition

DLS: Dynamic Light Scattering

DNA: Deoxyribonucleic Acid

DVP: Divinylbenzene

EDS: Energy-dispersive X-ray spectroscopy

EGDMA: Ethylene Glycol Dimethacrylate

FTIR: Fourier Transform Infrared Spectroscopy

GO: Graphene Oxide

Hb: Hemoglobin Human

HEMA: 2-Hydroxyethyl Methacrylate

HP: Hagen-Poiseuille

HSA: Human Serum Albumin

HWCVD: Hot Wire Chemical Vapor Deposition

iCVD: initiated Chemical Vapor Deposition

LCST: Low Critical Solution Temperature

LYZ: Lysozyme

MAA: Methacrylic Acid

MFC: Mass Flow Controller

NIPAAm: N-isopropylacrylamide

PAA: Polyacrylic Acid

PADPA: 4-Phenylazodiphenylamin

PBS: Phosphate-Buffered Saline

PECVD: Plasma Enhanced Chemical Vapor Deposition

PFDA: 1H,1H,2H,2H-Perfluorodecyl Acrylate

Phl: Phloroglucinol

PVDF: Polyvinyldene Fluoride

sccm: Standard Cubic Centimeters

SEM: Scanning Electron Microscopy

SFD: Single-File Diffusion

TBPO: tert Butyl Peroxide

UV: Ultra Violet

UV-vis: Ultraviolet–Visible Spectroscopy

CHAPTER 1. INTRODUCTION AND BACKGROUND

1.1. Separation by the Membrane

In general membranes are used to separate the molecules, based on different properties of the molecules, such as chemical structure, size or charge. Depending on the size of the separated molecules, separation via membrane can be classified as molecular (~2 - 20 nm), macromolecular (~ 30 - 800 nm) and particle (~ 1 - 1000 μm) and their usage areas and methods vary depending on these categories. Molecular separation is frequently used in drug transport, protein chromatography, virus or DNA studies, especially when it is used in areas such as desalination of water, gas separation, and dialysis. Among the molecular separation techniques, distillation, membrane-based filtration, centrifugation or electrophoresis are the most commonly used techniques [1, 2]. Recently, molecular sieves, magnetic nanoparticles, or techniques using microfluidic channels have begun to develop to reduce the energy used in separation, at the same time with high selectivity [3-5]. separation techniques include membrane-based techniques have advantages over other techniques due to lack of additives, ability to be made at low temperatures, low energy consumption, and ability to be made on an industrial scale, thus their use in different areas increases [6-8].

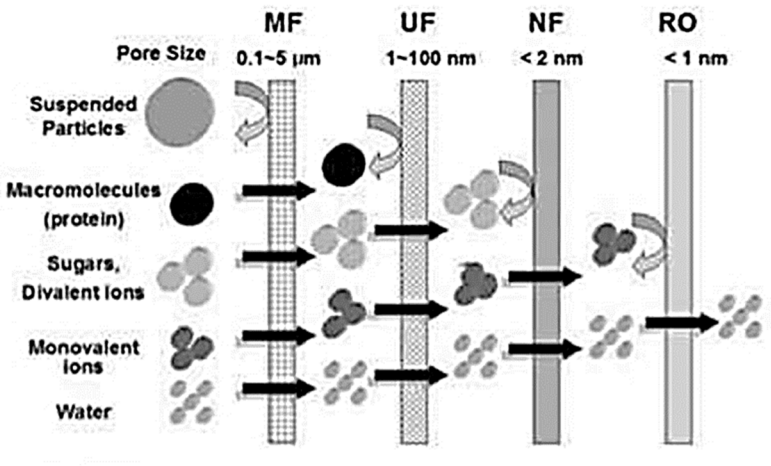

Figure 1.1. Different types of separation via the membranes [1]

Separation in membranes is based on the transport of molecules at different rates through the membranes, or by the selectivity to pass some molecules through the membranes according to their structures. Transport in the membranes is achieved by creating a pressure, concentration or electric field difference in membrane thickness. The factor that affects the rate of transport and selectivity in non-porous membranes is the interaction between the molecules being separated and the membrane material. In porous membranes, transport rate and selectivity are usually controlled by pore size, and separation is achieved by passing only small molecules through the membrane pore size. Separation of molecules by size is an effective method, but it is insufficient in separating molecules at similar size and selectivity is low. To increase selectivity, it is possible to separate the molecules according to their structural properties or their charge, by functionalization the pores and using the interaction between the surface of the pores and the molecules [9]. Porous membranes used for separation are usually formed by polymers with porous structure [10], with nanofibers [11] or by functionalization of pores of porous substrates [12]. Among different separation techniques, the separation technique using the functionalization of porous substrates is more advantageous than other techniques because of the low cost of the substrates, the ability to control the pore size and ease of functionality to get precise permeability and selectivity [12]. In separation applications, control of the permeability of the pores has been achieved by changing the pore diameter by using the pores with inorganic materials [13]. However, since it is necessary to

functionalize the pores to increase the selectivity, recent studies have concentrated on the pore coating of polymer materials [14]. Especially through the use of smart polymers ....Therefore, such polymers in applications demanding active response such as drug delivery applications has seen much usage [15]. Smart polymers are polymers that undergo physical or chemical changes are respond to an external stimulus such as temperature, pH, light [16].

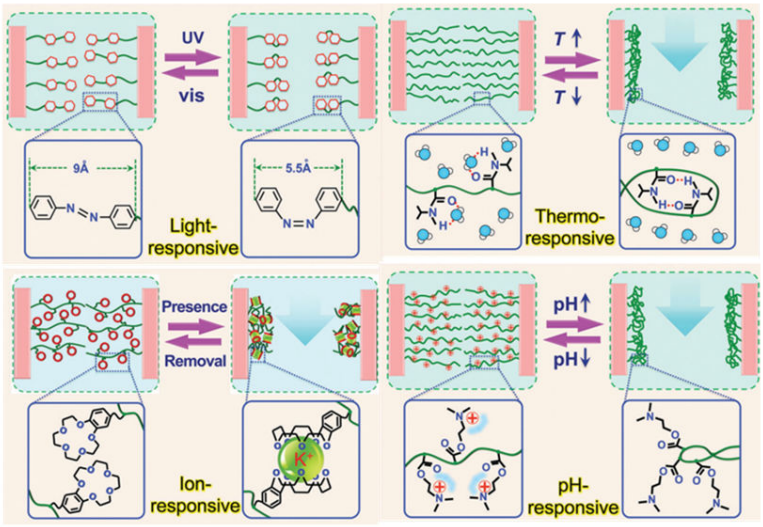

Figure 1.2. Different types of stimuli responsive polymers according to external stimuli [16]

The response mechanisms to the stimulus and the changes in the polymer structure are dependent on the chemical structure of the polymer and the external stimulus. For example, pH-sensitive polymers have ionizable pendants groups that can protonate and deprotonate depending on the pH change [17]. The pH-dependent change in net charge in suspended groups triggers physical changes in the polymer system. Temperature responsive polymers have a certain critical solution temperature at which phase changes or separations are observed. For example, poly (N-isopropylacrylamide) (PNIPAAm), undergoes a reversible volumetric phase transition at low critical solution temperature (LCST) because of the conversion of coils to globules [18]. While the hydrated polymer chains under LCST give the surface hydrophilic properties, the increase in hydrophobic interactions on the LCST leads to consequent dehydration and hence to a hydrophobic structure. Thanks to the ability to control the reaction of smart polymers via external stimuli based on their chemical structure, their use in a variety of areas such as controlled drug release, sensors and micromotors has recently become widespread [19, 20]. Functionalization of membrane pores with the use of smart polymers recently has been developed. The functionalization of the pores

generally involves covering the pore surfaces and changing the pore diameters or filling the pores with polymers and changing the barrier properties. Filling of the pores with functional polymers can be achieved by an immersion coating method, but coating polymers are limited [21]. In addition, it is not possible to cover the pore walls and to change the pore diameters to the desired size since the precise thickness control cannot be achieved. Functionalization of pore walls by functional polymers can be achieved by different methods. Gold is deposited inside the pore walls using a current-free chemical coating technique, then functionalized in the thiol solution [22]. The pores of the AAO membranes is functionalized with silica and pH-sensitive poly (acrylic acid) using the sol-gel method [23]. However, the problems of these techniques are that the polymers that can be bonded to the surface are limited and the bonding pores need to be modified with thin films in advance. Instead, techniques that provide direct coating of polymers to pore surfaces are more advantageous. For example, the pores can be coated with thin film by layer coating technique [24], but since the layer-by-layer coating technique involves polycation and polyanion bonding to the surface, the polymers that can be coated are limited to charged polymers and cannot use for smart polymers. Grafting polymerization techniques are the most commonly used techniques for coating membrane pores with smart polymers. Temperature-responsive PNIPAAM polymer is deposited on the pore walls of polycarbonate membranes using plasma-induced graft polymerization technique, to control water flow at varying temperatures [25]. In addition, the PNIPAAm is coated on the pore walls by immersing the membranes inside the NIPAAm solutions including photoinitiator, then exposing the membranes to UV rays [26]. It is possible to control pore sized by changing solution concentration and irradiation time. Nanoparticles with charged or functional groups can also be integrated to provide additional functionality with the smart polymers. Attaching nanoparticles on the surface can be achieved by activating the pores in a binding manner [27] or by embedding the coated polymer matrix [28]. To use the functionalized membranes as a molecular sieve, it is necessary to cover the polymers inside the pores homogeneously, to avoid problems such as blockage of the pores. Therefore, the technique of coating the pores with polymers is very important. The pore clogging due to the capillary forces is a significant problem in the liquid based coating techniques which require the membranes to be immersed in the solution, like grafting polymerization techniques, but this problem can be solved by vapor-based polymer coating techniques [29].

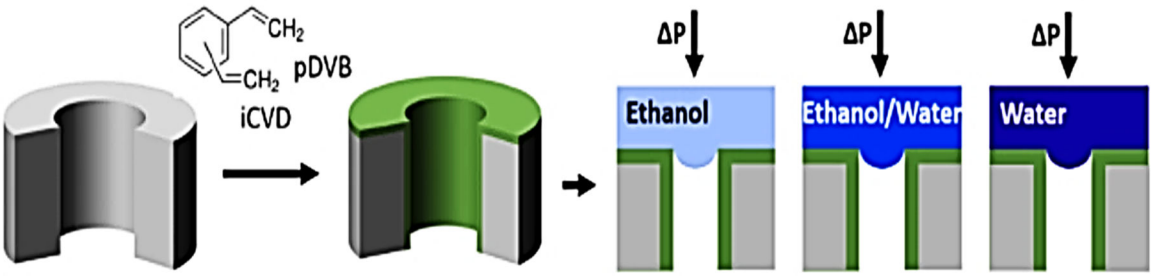

Figure 1.3. Nylon membranes treated with pDVB were tested for LEP using a series of ethanol/water solutions [83]

1.2. Chemical Vapor Deposition (CVD)

Chemical vapor deposition (CVD) is a thin film deposition method to produce coatings [30], nanotubes and fibers [31]. This method used reaction or decomposition of relatively high vapor pressure gases exposed on the substrate to produce the coating on it. CVD technique is a suited method to modify surface properties of bulk materials [30] or deposit thin film devices like thin film transistors [32, 33], photovoltaic cells [34, 35], and separation membrane [36]. In CVD process, reactants are in gas state, so this vapor phase technique is completely different than solution based techniques and has its own advantages including slow film growth rate to control and get precise film thickness, control chemical composition of films via tuning precursors flux ratio, clean final product, since it is a solvent-less process [37] and conformality [38, 39].

CVD technique is also used to produce polymer coatings as vapor phase polymerization. Vapor phase polymerization can be categorized in four methods according to polymerization mechanism [40] 1) step polymerization 2) chain polymerization 3) activated monomer polymerization, and 4) activated substrate polymerization. In step polymerization, monomers and reactive group vapors are introduced inside the chamber to deposit thin film on the substrate via condensation polymerization mechanism. Chain polymerization uses an initiator in vapor phase to dissociate as activated initiator. Then, chain growth polymerization occurs by adsorption of monomers and activated initiator on the substrate surface to form a polymer thin film. In activated monomer polymerization, monomers are activated by thermal or electromagnetic energy to generate activated species. Then these activated species undergo chain linking or crosslinking to create polymer thin films. For activated substrate polymerization, at first the substrate is activated,

following monomer vapors are introduced on the substage, and the reaction among the activated substrate and monomers produce polymer thin film.

The most important CVD techniques for polymer depositions are plasma enhanced CVD (PECVD) and hot wire CVD (HWCVD). PECVD utilizes plasma to enhance bombardment of the precursors, generation of a mixture of ions, atoms, radicals and electrons to polymerization with free radical polymerization [41, 42]. Deposition in this method is done at lower temperature but plasma high energy usually destroys the monomers desired functional groups or creation of side functional groups or undesired crosslinking. Moreover, deposition rate is high, and it is difficult to control it [43-45].

1.3. Initiated Chemical Vapor Deposition (iCVD)

iCVD can be consider as a kind of common hot wire chemical vapor deposition (HWCVD) technique. In HWCVD is used resistively heated filament wire to thermal decomposition of gas species passing through these hot array of filament, then activated species are adsorbed on the cooled substrate located in a small distance from the filament to form the thin film [46, 47]. In contrast with HWCVD method, in iCVD technique an initiator is introduced inside the vacuum chamber with monomers, too. In iCVD, monomers are heated to vaporize. These vapor state monomers and the initiator are introduced into low pressure (~0.1-10 mTorr) chamber with array of resistively heated Nichrome filaments (~180-280°C) and cooled substrate stage below them. The filament temperature is enough to decompose initiator to create activated free radical but not sufficient to decompose the monomer species. The low substrate temperature makes iCVD a suitable technique to deposit on the delicate, heat and solvent sensitive substrates such as plastics, fabrics, and pharmaceutics [48, 49]. The polymerization mechanism by iCVD can be divided into three steps. 1) decomposition of an initiator in the vapor phase to form primary free radicals, 2) diffusion and adsorption of primary free radicals and monomers from the vapor phase onto a cooled surface, and 3) polymerization of monomers on the surface to form a polymer coating. These primary radicals first attack to adsorbed monomers on the surface of substrate to change them into activated free monomers, then these active radical centers propagate by adding more and more monomer units to form longer polymer chains (propagation). The polymer chains are

terminated by combining two propagated polymer chains, or one propagated polymer chain and one activated free monomer or two activated free monomers [50, 51].

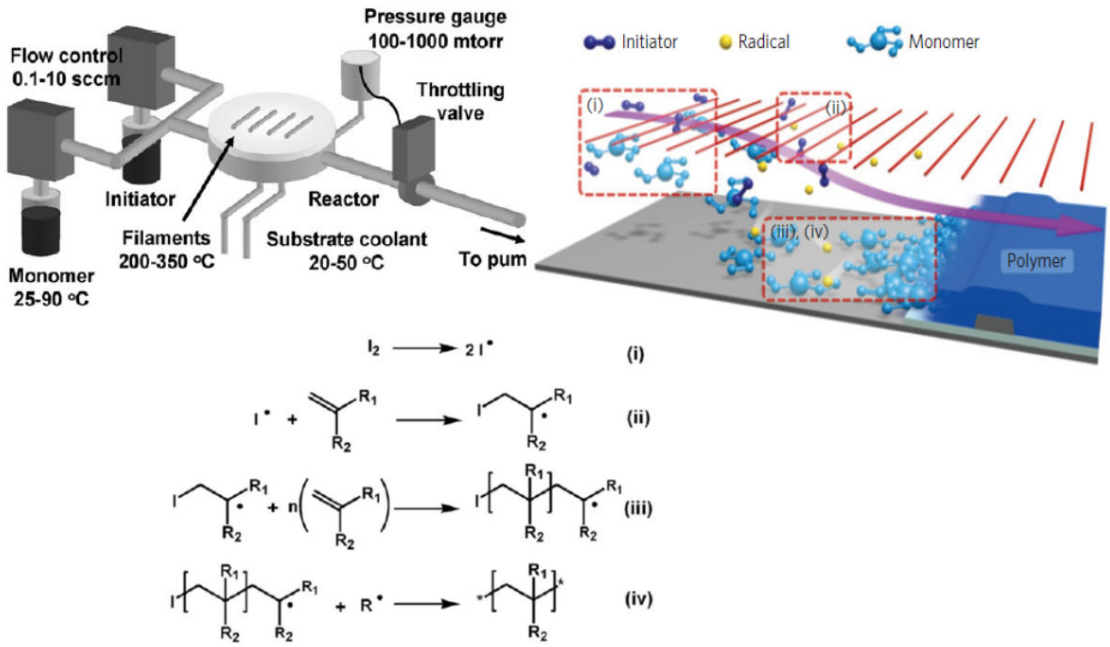

Figure 1.4. a) Schematic of the iCVD reactor and typical operating parameters b) Depiction of the iCVD mechanism. c) Free radical polymerization scheme [50]

Tuning iCVD parameters such as monomer and initiator flow rates and ratios, substrate temperature and vacuum chamber pressure triggers to produce exceptionally clean polymers with precise stoichiometric chemical composition and tunable molecular weight with no residual solvents or impurities, and the most important thing, deposition into complex topological geometries. iCVD, is utilized to synthesize variety of polymers including polytetrafluoroethylene [52, 53] acrylates [54, 55] methacrylates [56, 57], styrene [58, 59], vinyl [60, 61] and siloxane [62] in the form of copolymers [63, 64], and crosslinked ones [65, 66].

Thanks to the variety of polymers, copolymers, and crosslinked polymers synthesized via iCVD it is suitable to applications such as drug delivery [67, 68], sensors [69, 70], antimicrobial [30, 71], polymer electrolytes and polyelectrolytes [72, 73] and membranes [74, 75].

In solution polymerization methods, due to surface tension forces, lack of wettability, solution viscosity blockage of the structure and non-conformal coating will be achieved. In contrast, in iCVD because no liquids during polymerization process is used, conformal coatings to deposit complex geometries such as silicon membranes [48], gold microwires [76], elctrospun fibers [77], carbon nanotubes [77], and mesoporous titania nanoparticles [78] in nanoscales can be achieved. To get conformality, two parameters should be considered [79]. The ratio of the monomer partial pressure to the monomer saturation pressure is the first parameter. The monomer saturation pressure, is dependent on the substrate temperature and can be calculate using the Clausius-Clapeyron equation [54]. Low value of this ratio means, the monomer can diffuse inside the trench more before adsorbing on the surface and high conformality. In conformality, the important parameter is step coverage, the ratio of the film thickness at the bottom to the film thickness on the top of the trench [gm] and less step coverage means less conformality. In iCVD monomers and activated initiator diffuse to the pores from the top side of them to polymerization therefore, with increasing the distance from the top of the pores polymerization rate, film thickness decreases because of depletion of activated initiator and the rate of activated initiator depletion from the pore surfaces depends on sticking coefficient [80], and low sticking coefficient indicates conformal coatings. For a monomer or initiator which diffuse from the surface to inside the pores in depth L, number of collusion with the wall of pore is n times and for each collision the sticking coefficient of the monomer is Γ. Thus, the step coverage can be estimated as:

$$S = \frac{(1-\Gamma)^n}{(1-\Gamma)^0} = (1-\Gamma)^n \qquad (1.1)$$

The number of collusions can be estimated as $n=Z.\tau$ where Z is the frequency of wall-molecule collusion and τ is required time to molecule diffusion to the bottom of the pores. For larger Knudsen numbers, $Z=v_{gas}/w$, where vgas is the thermal velocity of the gas molecules and w is the width of the pore and $\tau=L^2/D$ where D is the diffusion coefficient. Diffusion coefficient inside the pore when $K_n>1$ is $D=2.1w.v_{gas}$. So

$$n = \frac{1}{2.1}\left(\frac{L}{w}\right)^2 \qquad (1.2)$$

$$LnS = -0.48\Gamma\left(\frac{L}{w}\right)^2 \qquad (1.3)$$

According to above equations when monomer saturation pressure increases, i.e. lower P_m/P_{sat}, sticking coefficient decreases leads to better step coverage and conformal coatings.

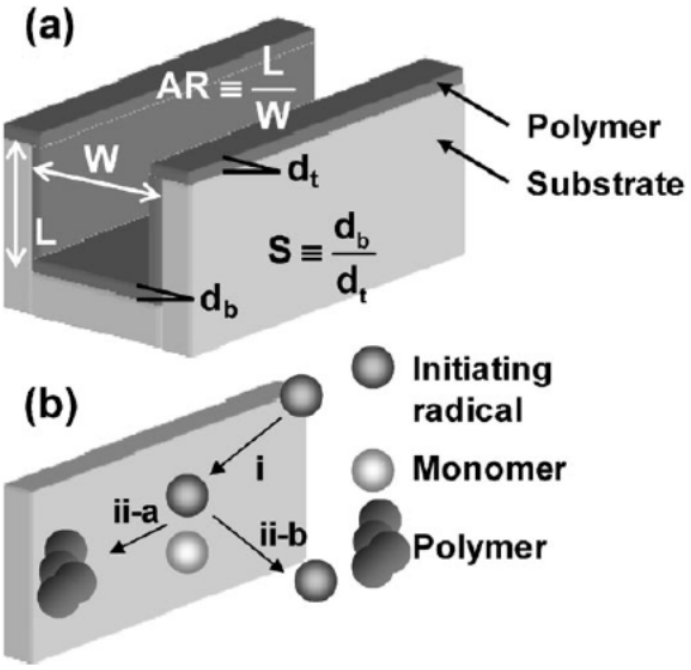

Figure 1.5. (a) Schematic of the quantities involved in an analysis of the sticking probability. (b) An impinging radical (i) can react with an adsorbed monomer if it strikes it directly (ii–a). If not, it will desorb back to the vapor phase within tens of microseconds (ii–b) [80]

Asatekin et al. have shown that the iCVD technique can be used for separation of molecules by deposition of a hydrophobic polymer inside the AAO templates conformally [81]. Matin et al. used iCVD to modify the surface of commercial reverse osmosis membranes using 2-hydroxyethyl methacrylate-co-perfluorodecyl acrylate (HEMA-co-PFDA) to evaluate antifouling properties of the membrane with sodium alginate as a model organic foulant [82]. Warsinger et al. [83] used iCVD technique to create superhydrophobicity with deposition perfluorodecyl acrylate on polyvinyldene fluoride (PVDF) membranes to study the effects of surface energy on fouling. Servi et al. studied the effects of iCVD film thickness and conformality on the permeability and wetting of membrane distillation [80]. Electrospun polytrimethyl hexamethylene terephthalamide (PA6(3) T) fibers is coated conformally with poly1H,1H,2H,2H-perfluorodecyl acrylate (PPFDA) to change the fiber surface properties using iCVD for desalination applications [84].

CHAPTER 2. EXPERIMENTAL METHODS

2.1. Membrane Fabrication

In this thesis, two different types of membranes are developed and studied. Free-standing polymeric membranes are fabricated by depositing polymer thin films on a Si wafer with a sacrificial coating and subsequently, removing the sacrificial layer to release the polymeric membrane. The second type of membrane is the hybrid membranes obtained by coating the pores of commercial AAO templates with polymers. In both cases, initiated chemical vapor (iCVD) deposition technique is used to deposit the polymer. In this section, the details of iCVD set-up and technique will be given. Details of membranes developed for specific studies will be presented at the beginning of each chapter. In this chapter, in addition to the deposition technique, characterization methods and the membrane permeation experiments will also be detailed.

2.1.1 Deposition Set-up

The iCVD deposition system includes three major sections; the precursor delivery section, the chemical reaction reactor and the exhaust system. In the precursor delivery section, to have enough monomer flow rate, the monomers inside the jars should be heated using heating tapes wrapped around the jars. The temperature and heating rate can be controlled by thermocouples installed in the bottom of the jar. Ideally, the monomer vapor pressure in the jar should be between 1-10 Torr to achieve flow towards the vacuum chamber due to pressure gradient. The temperature to heat the monomers to achieve the target pressure is determined by the Clausius-Clapeyron equation using the monomer vapor pressures at two different temperatures. The flow rate of monomers from the jar into the reactor is adjusted using needle valves and the flow rates of N_2 and initiator are controlled by mass flow controllers (MFC). The flow rates in standard cubic centimeters (sccm) are determined by monitoring the pressure increase in the sealed reactor in short time intervals in the temperature range of 40-45°C. The background leak in the system is also calibrated in the same way and is accounted for in the calculations of monomer flow rates.

The pipe lines which connect the jars to the chamber are heated up by wrapping a heating tape around them to avoid monomer vapor condensation and consequent clogging of the pipes. The reactor chamber is a 20-liter cylindrical stainless-steel vacuum chamber that is heated with heating tapes to 40^{o}C. The substrate holder is the stainless-steel stage at the bottom of the chamber and the temperature control of the stage is achieved by the embedded water lines at the back of the stage.

The chamber also includes a set of filament array, consisting of parallel NiCr (80%Ni, 20%Cr) wires located 2-3cm above the substrate holder. The filament temperature is monitored using a type-K thermocouple connected directly to one of the wires. For the experiments reported in this thesis, the temperature range of the filaments is 250-270^{o}C. The vacuum of the chamber is maintained by a mechanical pump and the pressure is monitored continuously using a pressure gauge. The base pressure of the chamber is 5 mTorr and the process pressures during deposition are in the range of 100-1000 mTorr.

The real-time monitoring of the polymer film thickness during deposition is done using a Helium/Neon (He/Ne) laser interferometry set up. The entrance and the exit of the laser beam into the reactor is through two transparent quartz windows on top the chamber. He/Ne laser beam (632.8 nm) reflects from the thin film and because the beam that is reflected from the top of the thin film and the one that is reflected at the thin film-substrate interface have different phases, they show alternating constructive and destructive interference as the film grows thicker. The oscillations in the laser signal detected by the detector can then be converted to thickness. The real-time monitoring of the coating thickness allows stopping the deposition once the target thickness is reached.

2.1.2 Deposition Procedures

In order to introduce the monomer vapors inside the chamber, the monomer flow rate should be calibrated to find P_m/P_{sat} to decide about polymerization rate. At first, the leak of the system is measured. The leak comes inside the chamber through the system port. The leak should be subtracted from the precursors to get real flow rate of precursors. For this purpose, the vacuum chamber is cut from the vacuum pump and the pressure increase is monitored by passing the time. Plotting time-pressure curve gives us dp/dt to calculate leak flow considering the chamber temperature and volume. The flow rate of monomers, initiator and Nitrogen gas should be

calculated. For this, at first on/off and needle valves are opened completely for two minutes to allow extra pressure of preheated monomers inside the jar to evacuate, then using the needle valve, the flow rate of monomer is calibrated. The needle valve is opened for specific turns then the chamber is cut from the vacuum pump and chamber pressure increase is monitored each five second for two minutes. The slop of time-pressure is used to calculate monomer in that specific needle valve turns considering the flow rate of the leak. This procedure is continued for several different turns. The same method is used for the other monomers, initiator and Nitrogen gas but for initiator and N_2, calibration for one minute is enough. After calibration of precursor, according to flow rates, the composition of copolymers can be determined. Using the substrate temperature and deposition total pressure the deposition rate can be adjusted according to P_m/P_{sat} ratio. For slow deposition rate, P_m/P_{sat} ratio should be near 0.1 by increasing substrate temperature or decreasing total deposition pressure or both parameters. To get fast deposition, P_m/P_{sat} ratio should be near 0.7 by reducing the substrate temperature, enhancing total pressure of both.

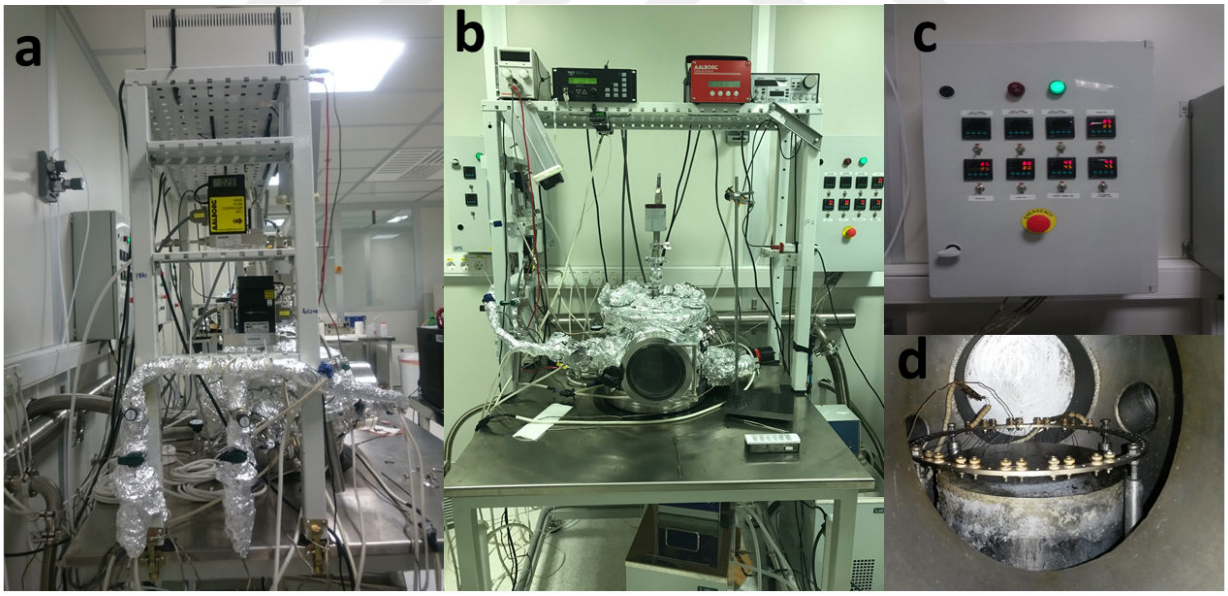

Figure 2.1. Picture of the iCVD system: a) precursor delivery section including jars, needle valve, MFC and piping b) reactor chamber with pressure gauge, mass flow controller, substrate temperature controller and He/Ne laser c) thermocouple controller panel d) filament part including array wrapped around the ceramics and thermocouple

To start deposition, the substrate is placed on the temperature controlling stage, the laser is adjusted to get reflection from the substrate to the laser detector to control this film thickness in situ during the deposition. To start deposition, at first the filament temperature is increased to 120°C, then N_2

and initiator are introduced inside the temperature. Meanwhile, the monomers are introduced inside the reactor while the needle valves turn in a specific number of turns and the pressure is adjusted the target pressure. Finally, the filament is set at a temperature higher than 230°C. The deposition is monitored in situ by the laser to reach desired thickness. After that, at first flow of monomers are cut, the filament temperature decreases, then initiator flow is cut, and the pump is opened completely to vent the rest precursors inside the reactors. Finally, the flow of N_2 is cut before venting the chamber to get the sample.

2.2. Material Characterization

The characterization studies involve characterization of the structure and performance of the polymer thin films on Si surface, free-standing polymer thin films and hybrid membranes.

2.2.1. Optical methods

2.2.1.1. Fourier Transform Infrared Spectroscopy (FTIR)

FTIR is used for the characterization of the chemical composition of the polymer thin films. The chemical bonds have specific wavelength to absorb infrared radiation and vibration [85]. Every molecule or bonding has specific vibration energies, so they have a specific absorption peak in the FTIR spectrum, as long as they are asymmetrical bonds. Each molecule has a specific vibrational frequency to absorb the radiation. N_2 purging is used to avoid CO_2 and H_2O peaks from air on the thin film spectra. For thin films, at first the background absorption of the substrate (Si wafer) is collected, then this is subtracted from the adsorption of the thin film on the substrate by the software.

2.2.1.2. Ultraviolet–visible Spectroscopy (UV-vis)

UV-vis is absorption spectroscopy or reflectance spectroscopy in the ultraviolet-visible spectral region. In this region of the electromagnetic spectrum, atoms and molecules undergo electronic transitions. The absorption or reflectance in the visible range can be understood from their colors. Absorption spectroscopy and fluorescence spectroscopy are near the same, with the difference that fluorescence faces with transitions from the excited state to the ground state, while absorption measures transitions from the ground state to the excited state [86]. Π-electrons or non-bonding electrons (n-electrons) in the molecules absorb the ultraviolet or visible light to get energy for

exciting these electrons to higher anti-bonding molecular orbitals [86]. When light is incident on matter, part of light is absorbed inside the molecules and electrons are excited to higher energy level. The amount of absorption at different wavelengths by a material is detected via a spectrometer and absorbance (A) versus wavelength (λ) is plotted as a spectrum. λ_{max} is the wavelength at which the sample absorbs the maximum amount of light [86].

2.2.1.3. Spectroscopic Ellipsometry

Spectroscopic ellipsometry is a non-destructive optical technique that allows for the measurements of sample properties based on the changes in polarization of the light that is reflected from the sample such as film thickness, refractive index, and extinction coefficient. If all photons of a light beam are oriented in the same direction the light is referred to as polarized light. Ellipsometry uses polarized waves and two waves with the same frequency combine in 90 degrees phase difference. The amount of the light ellipticity changes when it is reflected from the sample. Ellipsometric measurements are done as a function of wavelength, or the incidence angle, or both. Generally, ellipsometers contain a light source, a polarizer, to polarize the light on the sample, and a detector to measure the amount of light polarization after reflection from the sample [87].

2.2.2. Structural methods

2.2.2.1. Scanning Electron Microscopy (SEM) and Energy-Dispersive X-Ray Spectroscopy (EDS)

SEM get images from a sample by using secondary electrons, back scattered electron and characteristic X-rays enter in the detectors in the vacuum chamber. Electrons are accelerated from an electron gun. SEM uses electromagnetic lenses to focus the electron. There is a scanning coil along the path of electron inside the chamber. The scanning coil is used to control electrons direction which helps to focus the electron beam on a region on the surface of the sample. When electron beam hits the sample surface it interacts with the electrons of the sample on the surface and inside the sample. The backscattered electrons (BSE) when collected at the detector, its signals are used to understand the distribution of different elements in the sample. The secondary electrons are generated from knocking of the outer electrons of surface atoms on the sample surface. They are collected at the SE detector and are used to get topography of the sample. The characteristic x-ray is another type of emission that occurs due to the interaction between the accelerated electron and the electrons in the inner shell of the atoms. This interaction causes the inner shell electrons

to be removed and replaced by higher energy electron resulting in the release of energy in a form of x-ray emission. The composition and measurement of the abundance of various elements in the sample are identified with the help of the characteristic x-rays detected at the x-ray detector [88].

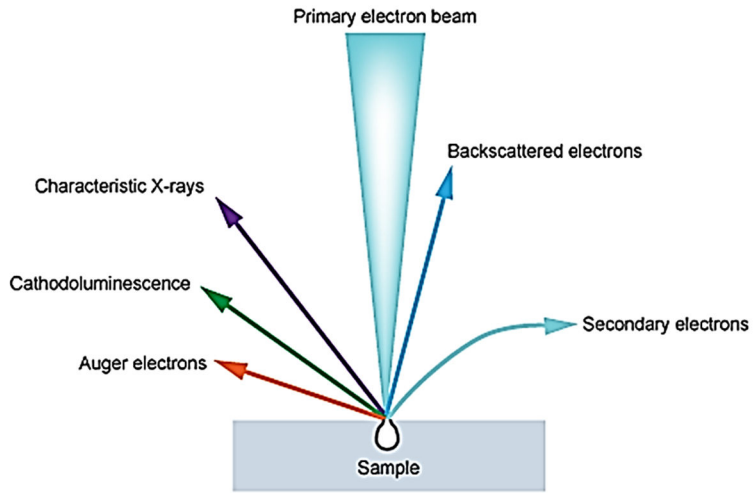

Figure 2.2. Incidence of accelerating electron beam on the sample and generation of secondary electrons, back scattered electron and characteristic X-rays

2.2.2.2. Atomic Force Microscopy (AFM)

Atomic force microscopy is used to measure sample heights, surface frictions and topographies. AFM consists of a probe tip attached to a piezo cantilever, a laser diode, a position sensitive detector and a feedback loop. The interaction force during measurement is converted to signals used in creating a corresponding image for the surface and height of the sample. The principle of atomic force microscopy is based on the force between the probe tip and sample surface. It also uses both the forces of attraction and repulsion. The forces between the probe and sample are kept constant irrespective of the surface topography. This can be achieved through a feedback loop, which constantly adjusts the interacting force. The photodiode is a laser source which directs the beam of light on the back of the cantilever. The reflected light is collected by the positioned sensitive detector. The detector uses this information for creating an image. The photo sensitive detector is divided into four segments; this tracks the position of the laser spot on the detector and thus measuring the angular deflections of the cantilever [89].

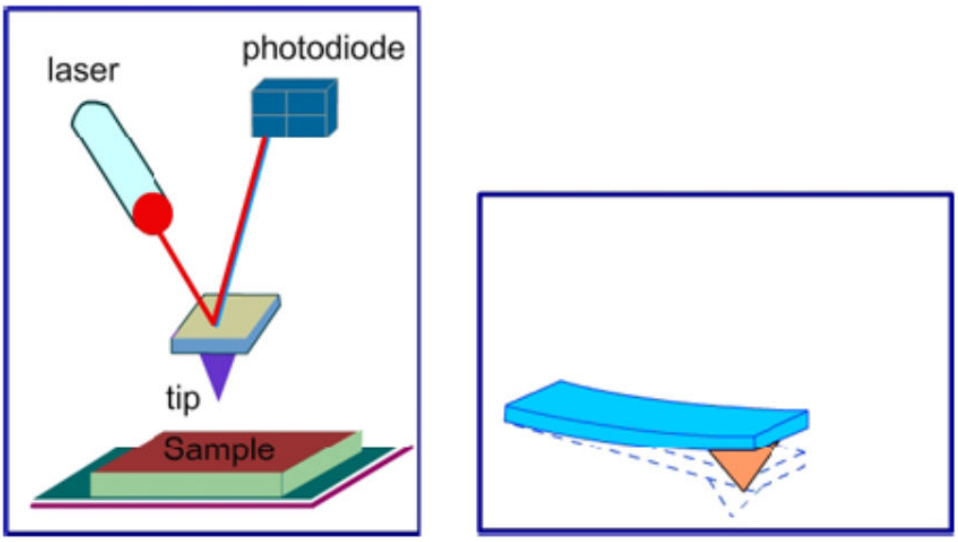

Figure 2.3. Diagram of crucial AFM components. (a) shows a representation of the tip; it contains a probe straddled on a cantilever, and in (b) the cantilever easily bends even with a slight force on the tip

2.3. Membrane Performance Methods

2.3.1. Permegear Side-bi-side Diffusion Cells

Permeation and diffusion studies of the macromolecules are performed in a Permegear side-bi-side diffusion cell. The diameters of the cells are 30mm and the volume of each cell is 50mL. The cell contains, heater/circulator ports, donor and receptor chambers, stir bars, cell clamp, sampling ports and tension knob. The membrane is placed between the two chambers and fixed using tension knob. The experiment temperature is adjusted using water flow through the heater/ circulator ports inside the water jacket around the chambers by a chiller. Samples are taken via sampling ports for UV-Vis tests. The liquid inside the chambers is stirred using stir bar during the experiments to keep the solutions homogeneous in all parts of the chambers.

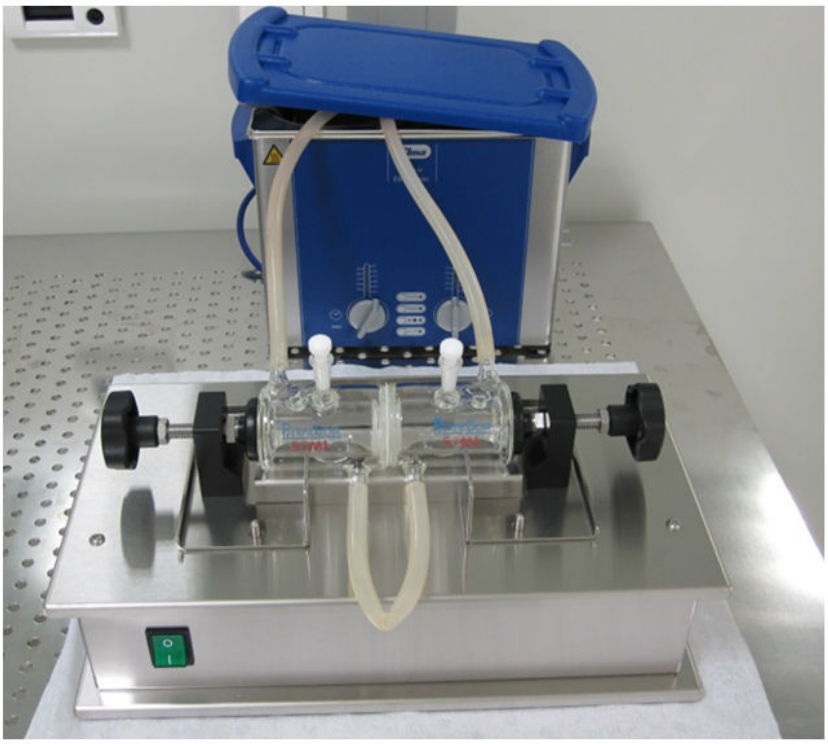

Figure 2.4. Permegear side-bi-side diffusion cell with heater/circulator ports, donor and receptor chambers, stir bars, cell clamp, sampling ports and tension knob. The hoses are used to guide water flow from heater/circulator ports to control the temperature

2.3.2. Homemade Side-bi-side Diffusion Cells

For the diffusion tests of the protein through the membrane, a homemade side-bi-side diffusion cell is used. The cell is 10mm in diameter, has a volume of 3mL and is made of Teflon. The cell consists of donor and receptor chamber, stir bars, sampling ports and clamp. The membrane is placed between two chambers then two chambers are fixed by the clamp and put on the stirrer. To avoid protein denaturation during experiments, the cell was put in cold room where its temperature was kept at 4°C. Samples are sampled from the sampling ports using a syringe.

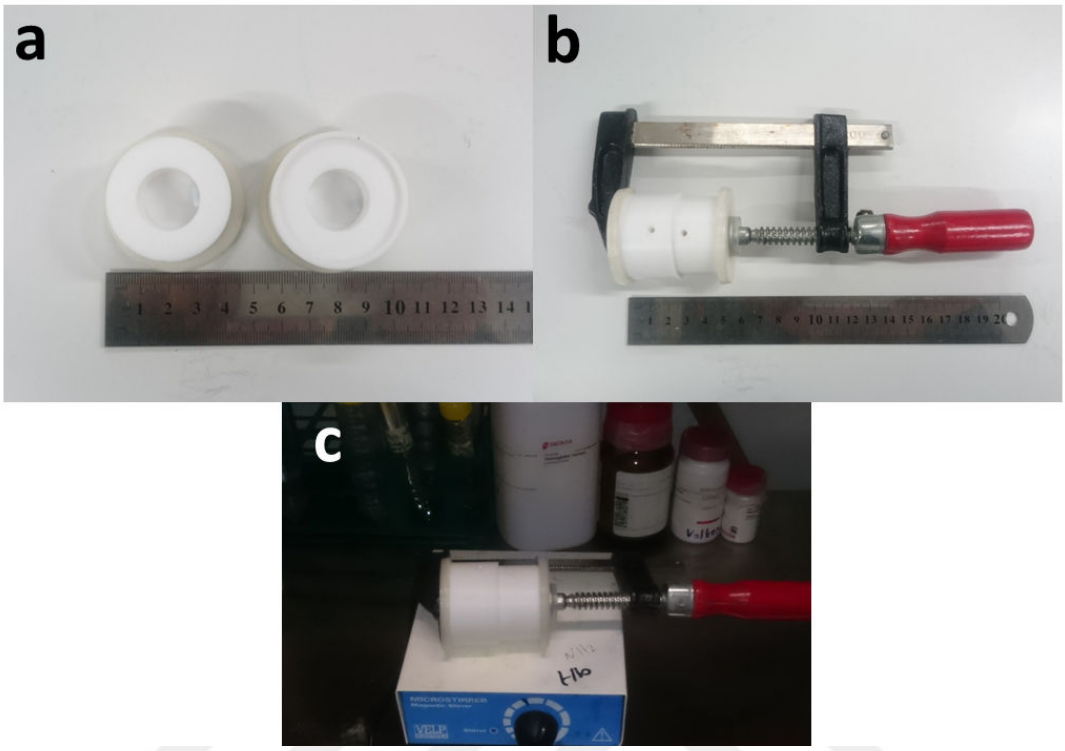

Figure 2.5. Homemade diffusion cell a) donor and receptor chambers, stir bars b) sampling ports and tension knob. c) the cell on the stirrer inside the cold room

2.3.3. High Pressure Permeation

Hydrodynamic permeability tests of the composite membranes were performed using a high-pressure diffusion test set-up (Sterlitech cells). For this purpose, high pressure Sterlitech cells are filled with water and nitrogen gas, is delivered to the system under different pressures. The pressure used during the test is systematically increased to 5bar. The weight of the water accumulated in the filter cell is measured via precise weighing at certain time intervals and the water flux is determined. The permeabilities of the produced membranes were tested with pure water, proteins, and polyacrylic acid permeates.

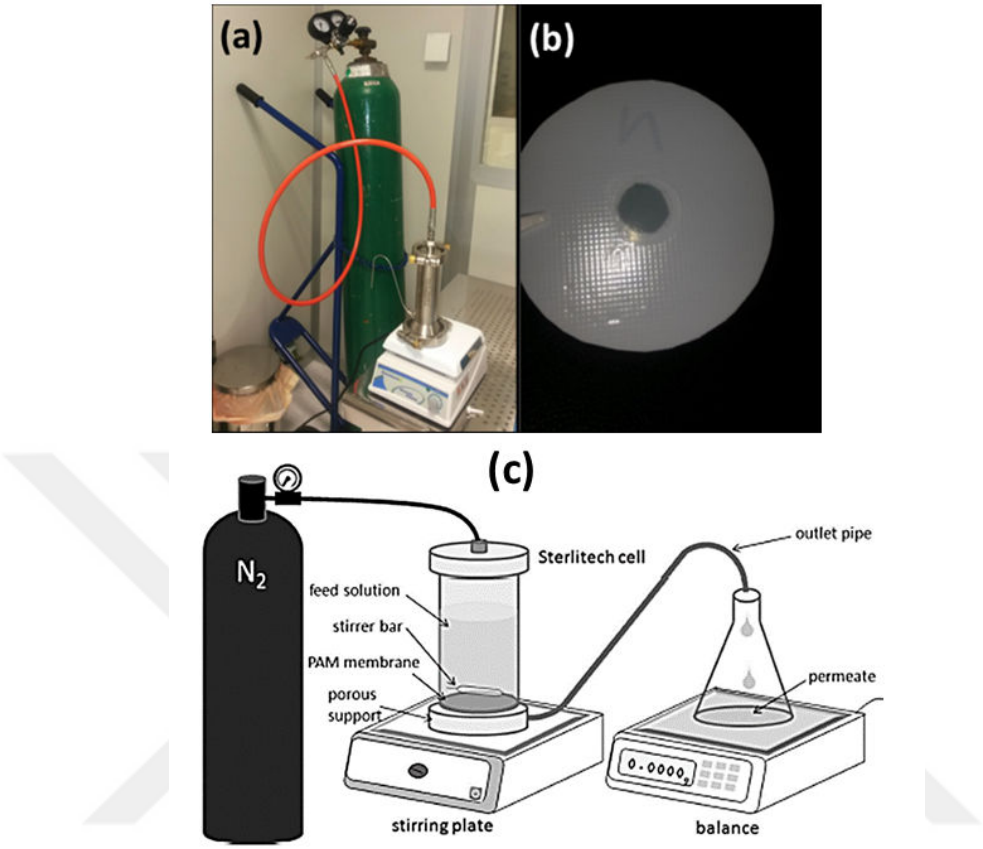

Figure 2.6. a) High pressure Sterlitech cells with stirrer and Nitrogen tube b) membrane glued to the plastic holder c) Schematic picture of high pressure permeation and sample collection

CHAPTER 3. FREE-STANDING MEMBRANE

3.1. Introduction

The aims of this chapter is to develop and characterize nonporous, ultra-thin free-standing membranes of functional p(HEMA) polymers with tunable mesh size to control the diffusion of model dye molecules. The permeability and selectivity of the separating membranes are the critical factors affecting the performance, thereby making the studies involving improvements of membrane properties quite important. Due to the difficulties in synthesizing free-standing polymer thin films with different mesh sizes using conventional fabrication techniques, reports on the permeability properties of free-standing polymers are limited. In this Chapter, a systematic study on fabrication of p(HEMA) membranes with different mesh sizes is presented. Tuning the mesh size allowed to control the permeation of small molecules with different size and polarities and via systematic diffusion studies, permeation and diffusion coefficients of the molecules were obtained. Difference in polarities of the permeants enabled selective permeation of the small molecules through the membranes.

3.2. Experiment Methods

3.2.1. Membrane Preparation

Free-standing polymer thin film membranes were prepared by depositing the polymer thin film on a sacrificial layer using iCVD and subsequently removing the sacrificial layer. The sacri- ficial layer was prepared by spin coating of Polyacrylic Acid (PAA) solution (2.5 g PAA and 7.5 g water) on a Si wafer at 1500 rpm for 15 s followed by baking spin coated solution for 2-3 min on a hot plate at 80-100°C. p(HEMA) thin films with 1000 nm thickness were then coated on the sacrificial layer using iCVD. The monomer HEMA, the cross-linking EGDMA, the initiator TBPO were used as received, without further purification. HEMA and EGDMA were vaporized in the jars at 70°C and 80°C, respectively and TBPO was at room temperature. The vapors were then delivered to the vacuum chamber from different ports. The flowrates of N_2 and TBPO were fixed at 1 sccm while the flowrates of the monomers were varied between 0.05 and 0.5 sccm to obtain polymers

with different crosslink ratios. The operating pressure was set to 250 mTorr and the filament and stage temperatures were kept at 270°C and 30°C, respectively during the depositions. The thickness of the samples was monitored real-time using a laser interferometry system and the deposition was stopped at a film thickness of 1000 nm. After the iCVD process, a plastic holder of 5 cm diameter with a 2cm diameter hole at the center was glued on the polymer layer surface (Figure 3.1.a) and then the sample was immersed in DI water to dissolve the PAA layer. The p(HEMA) layer was detached from the Si substrate following the removal of PAA layer.

3.2.1.1. Polymer Coating Characterization

Fourier transform infrared (FT-IR) (Thermo-Nicolet iS10 FTIR) measurements were performed in normal transmission mode. Spectra were acquired over the range of 400-4000 cm^{-1} with a 4 cm^{-1} resolution for 64 scans. All spectra were baseline corrected and normalized to a thickness of 1000 nm. Accurate measurements of film thickness were performed using a spectroscopic ellipsometer (M2000 Spectroscopic Ellipsometer J. A.Wollam Co., Inc.). All thickness measurements were made at 65, 70, and 75 incidence angle using wavelengths ranging from 315 to 718 nm. The Cauchy model was used to fit data. The swelling ratios of the polymer films were measured in a heated liquid cell with nominal angle of incidence of 75 degrees. The change in thickness of the films as water was introduced, was recorded as a function of time. The swelling ratio was then calculated by t_0/t, where t_0 and t are the thicknesses of the dry and swollen polymers, respectively. The swelling experiments were repeated multiple times and the samples were dried after each experiment. The elastic moduli of the films were measured using the peak force quantitative nanomechanics (QNM) mode of the Multi-Mode AFM. First, force curves on the polymer surface were obtained at different locations and then, Hertzian fit modeling was applied to these force-versus-separation curves.

3.2.1.2. Permeation Experiments

Permeation studies of dye molecules through the polymer membranes were performed in a side-by-side diffusion cell (50 mL PermeGear Side-bi-Side Diffusion Cell) with an effective membrane area, A, of 3.14 cm2 at atmospheric pressure (Figure 3.1.b). The free-standing polymer membrane was placed between two cylindrical glass chambers of 50 mL volume. One chamber was filled with feed solution and the other chamber was filled with DI water, solutions in both chambers

were stirred continuously by magnets throughout the experiments. The experiments were performed at 25°C and 50°C. The feed solutions were prepared at different dye concentrations. The model dyes used for the experiments were Phloroglucinol (Phl), Alizarin Yellow (AY) and 4-Phenylazodiphenylamine (PADPA). Three different dye solutions were used in the experiments: Phl (0.6 g/L), AY (0.07 g/L) and AY1PADPA (0.07 g/L each). Permeation rate of the dye molecules were calculated by measuring the dye concentration on the permeate side periodically. This was done by taking 3.5 mL of the permeate solution and performing UV-Vis measurements (Shimadzu UV-3150). After the measurements the solution was poured back into the permeate chamber. To find the solute partition coefficient, K, which was used to calculate the diffusion coefficient, the membranes were immersed in dye solution for 7 days and the ratio of the dye concentration in the membrane to the concentration in the solution was calculated.

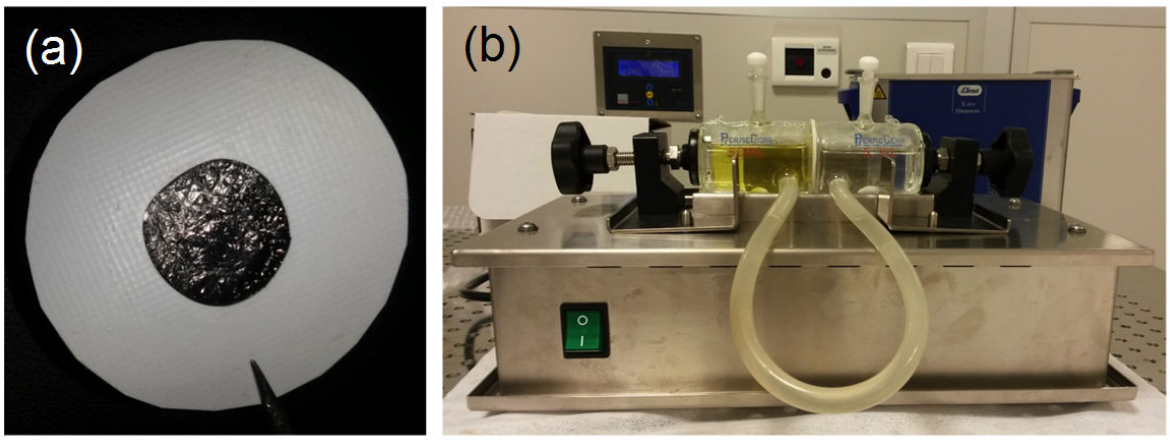

Figure 3.1. (a) Free-standing p(HEMA) membrane and the white plastic frame surrounding it are shown. (b) Side-bi-side diffusion cell used for permeation tests is shown

3.3. Results and Discussion

The thickness-normalized and baseline-corrected FTIR spectra of the p(HEMA) thin films with different crosslink ratios are shown in Figure 3.2. The peaks observed at 3550-3050 cm^{-1} and 1750-1690 cm^{-1} correspond to the vibrational modes of O-H stretching and C=O stretching respectively. Intensity of the O-H stretching peak decreases with respect to C=O stretching peak as the EGDMA ratio in the feed is increased, confirming an increase in the crosslink ratio. The crosslink percentages of the deposited films are calculated using the FTIR spectra where the areas under the peaks are proportional to the concentrations of C=O or O-H groups in the films, assuming similar

bond oscillator strengths for both HEMA and EGDMA [90]. The ratio of EGDMA to HEMA in the film, which is related to the crosslink ratio, can be found using:

$$\frac{\text{EGDMA}}{\text{HEMA}} = \frac{(A_{C=O} - rA_{O-H})/2}{rA_{O-H}} \tag{3.1}$$

where A represents the area under the peak of the corresponding vibrational mode in the copolymer films and r is the ratio of $A_{C=O}$ to A_{O-H} in the linear p(HEMA) film. Table I shows the crosslink ratios of the deposited p(HEMA) films.

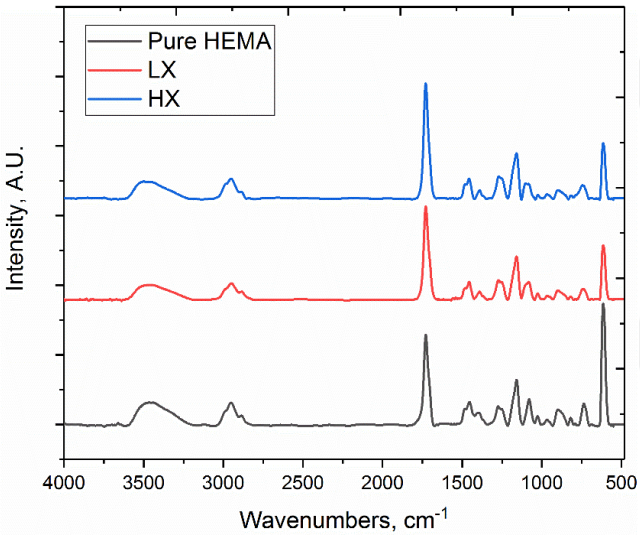

Figure 3.2. FTIR spectra of the deposited uncrosslinked, high crosslinked (HX) and low crosslinked (LX) p(HEMA) membranes. The peaks representing the C=O stretching vibrational modes are shaded with horizontal lines, while the peaks representing the O-H vibrational modes are shaded with diagonal lines

Table 3-1. Deposition parameters and the crosslink ratios of the iCVD deposited p(HEMA) free-standing films are given

Samples	Flow Rate (sccm)		P_m/P_{sat}		Crosslink Ratio
	HEMA	EGDMA	HEMA	EGDMA	
LX	0.5	0.086	0.182	0.404	0.32
HX	0.5	0.14	0.179	0.646	0.47

The reactivity ratios of the monomer precursors are used to determine the chemical composition of the copolymer films. The reactivity ratios are calculated using the Fineman-Ross copolymer

equation modified to account for the two vinyl groups of the EGDMA monomer, which is given by [91]:

$$\frac{f'_{EGDMA}(1-2F_{EGDMA})}{F_{EGDMA}(1-f'_{EGDMA})} = r_{HEMA} + \left[\frac{f'^{2}_{EGDMA}(F_{EGDMA}-1)}{F_{EGDMA}(1-f'_{EGDMA})^{2}}\right] r_{EGDMA} \quad (3.2)$$

In iCVD, polymerization mechanism takes place on the surface, therefore the rate of polymerization depends on the surface monomer concentration f', instead of gas monomer concentration f_{EGDMA} which is generally used in the Fineman-Ross relation. In eq. (2), f'_{EGDMA} and FEGDMA correspond to the surface mole fraction of EGDMA monomer and the mole fraction of the EGDMA in the polymer, respectively, whereas r_{EGDMA} and r_{HEMA} correspond to the reactivity ratios of the monomers. The mole fraction of the EGDMA is determined from the FTIR analysis as described in the previous section. In Henry's law limit for low surface concentrations, the BET isotherm predicts linear relation between the amount of monomer on the surface and the P_m/P_{sat} values, where P_m is the partial and P_{sat} is the saturation pressures of the monomer [54]. Thus, partial and saturation pressures of the monomers can be used to obtain the f 0 EGDMA and f 0 HEMA values. Using eq. (2), the reactivity ratios of EGDMA and HEMA are found as 0.169 and 0.886 respectively, confirming copolymerization.

Figure 3.3(a) shows the SEM image of a free-standing membrane. The AFM surface images of the low (LX) and high crosslinked (HX) polymer films show that the films are uniform with no phase segregation and the surface roughness is below 5 nm [Figure 3.3(b)]. Furthermore, the elastic moduli of the membranes are measured as 28.64 MPa for high crosslinked and 21.67 MPa for low crosslinked films by using the QNM mode of the AFM.

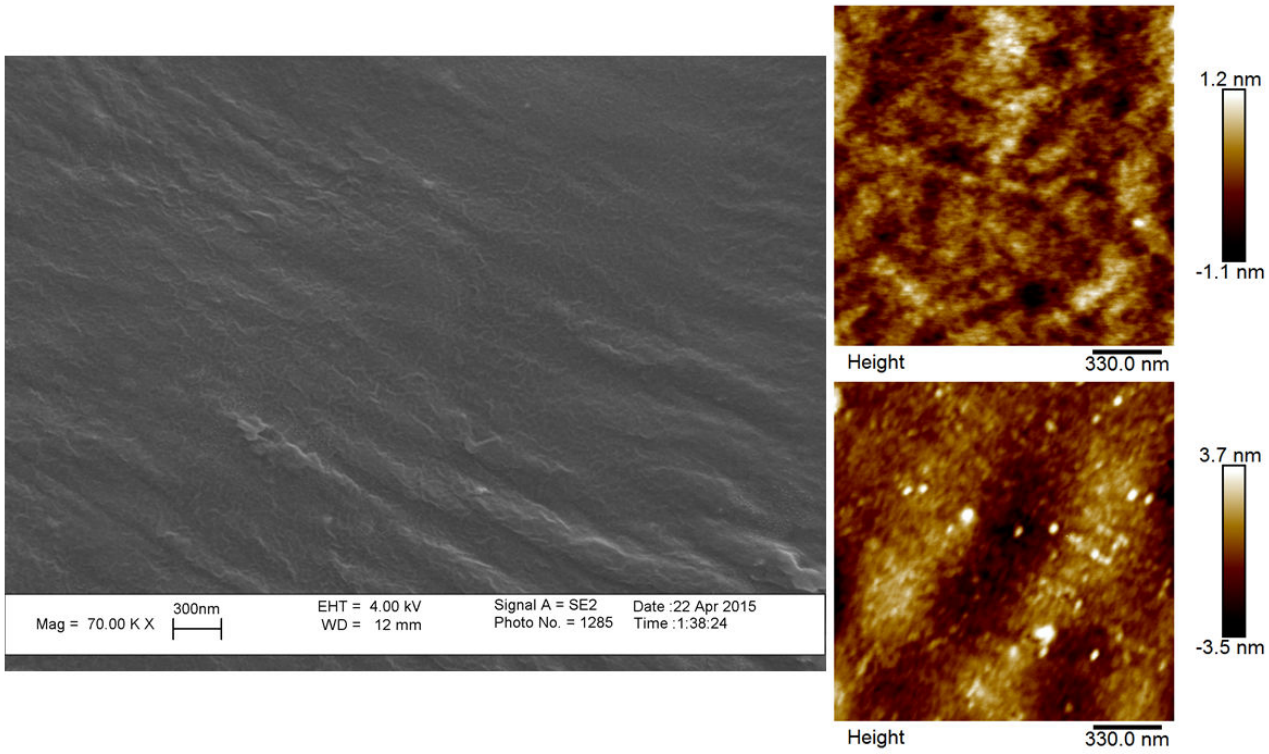

Figure 3.3. (a) SEM image of the free-standing HX p(HEMA) membranes before the diffusion tests. (b) AFM surface images of the LX and HX p(HEMA) membranes before the diffusion tests. The RMS roughness of the samples is less than 5 nm

If the membranes are carefully handled avoiding cracks, the membranes can be reused in the permeation studies, confirming their stability. The permeation of the molecules through the membrane depends on the relative sizes of the molecules to that of the mesh size of the polymer. Therefore, tuning the mesh size of the polymer via adjusting the crosslink ratio enables control of the permeation mechanism. The average molecular weight, M_C between crosslinks, which is related to the mesh size, ξ can be calculated using [92]:

$$\frac{1}{M_C}=\frac{1}{M_n}-\frac{\frac{v}{V}[Ln(1-v_s)+v_s+\chi v_s^2][1-\frac{M_r}{2M_C}(v_s)^{2/3}]^3}{[v_s^{\frac{1}{3}}-\frac{1}{2}v_s][1+\frac{M_r}{2M_C}v_s^{1/3}]^2} \quad (3.3)$$

where M_n is the number average molecular weight which is large enough so that the first term on the right-hand side can be neglected [93]. V is the molar volume of water (18 cm^3/mol), M_r is the molecular weight of the HEMA repeat unit (130 g/mol) and ν is the specific volume of p(HEMA) (0.87 cm^3/g). χ is the Flory-Huggins interaction parameter and is taken as 0.681 in this study for p(HEMA) polymers crosslinked with EGDMA [94]. The swelling ratios of the polymers, denoted

as ν_s, are obtained from ellipsometry measurements and they are 0.69 and 0.75 for low and high crosslinked samples, respectively. The ellipsometry measurements are performed on polymer films deposited on Si substrates. Repeating the swelling tests multiple times confirms that the swelling of the films is reversible. Reports on the effects of substrate confinement on the swelling of the polymer films exist in literature, reporting less swelling observed in surface-attached polymer films compared to that of nonattached films [95]. Furthermore, reports on the spin-coated films show that surface confinement effects on the swelling ratio are negligible for the nonattached ultra-thin films [96]. In the study presented here the polymer films are directly deposited and physiosorbed on the substrate without any surface attachments, which would affect the polymer chain mobilization. The values of M_C for low and high crosslinked samples are determined as 152.43 g/mol and 127.34 g/mol, using Eq. (3). The mesh size of the deposited polymers, ξ can be determined using the relation:

$$\xi = \nu_s^{-1/3} l \left(\frac{2M_C}{M_r}\right)^{1/2} C_n^{1/2} \tag{3.4}$$

Where C_n is the characteristic ratio for HEMA which is taken as 0.69 [97] and l is the C-C bond length which is 0.154 nm. The mesh sizes of the low and high crosslinked samples are, then, calculated as 0.651 nm and 0.575 nm, respectively. The larger mesh size observed at low EGDMA content is due to low crosslinking of the films confirming that the mesh size can be controlled by tuning the chemical composition. As the HEMA content in the films increased, dissolution of the polymer films was observed. The dissolution of the uncrosslinked pHEMA films can be attributed to the low molecular weight of the deposited films. Dissolution of the uncrosslinked pHEMA films is not observed at ultrahigh molecular weights of 820,000 g/mol due to the entanglement of the long polymer chains [98]. The molecular weight of the deposited films, on the other hand, can be controlled by changing the ratio of initiator/monomer flowrates. Initiator to monomer flowrate ratios of 20, as used in our study, give short- chained, low MW polymers, compared with ultrahigh MW polymers obtained at initiator to monomer flowrate ratios of 0.5 [98]. Tuning of the mesh size is critical for membrane applications that rely on size exclusion. In the study reported here, the size selection characteristics of the membranes are studied using hydrophilic model dyes and the permeation through the free-standing polymer films with different mesh sizes are monitored using a diffusion cell. As the model dyes, hydrophilic alizarin yellow molecules and larger

phloroglucinol molecules and relatively hydrophobic 4-Phenylazodiphenylamine molecules are used.

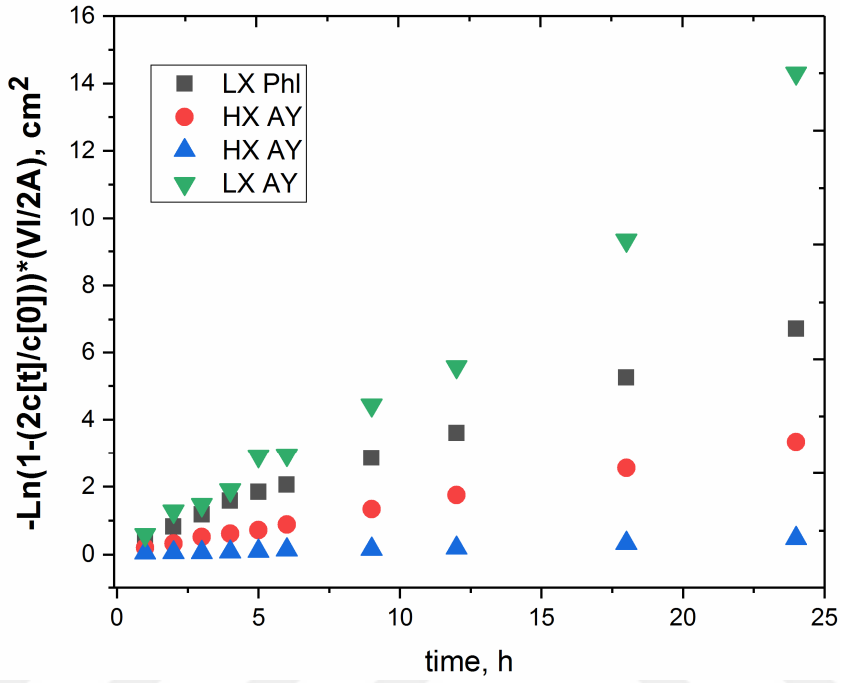

Figure 3.4. Plot of Eq. (5) where y(t) = -(V/A) *ln(1-c(t)/c (0)) showing the change in dye concentration as a function of time for low and high crosslinked samples tested with AY and Phl dyes. The slope of the plots gives the permeability coefficient, P

The change in dye concentration as a function of time on the receptor end is recorded and the solute permeability coefficient, P, is determined using:

$$\mathrm{Ln}\left(1-\frac{2c[t]}{c[0]}\right) = -\left(\frac{2AP}{V}\right)t \qquad (3.5)$$

where c [0] is the initial dye concentration in the donor cell, c[t] is the concentration at time t in the receptor cell, V is the cell volume (50 mL) and A is the effective membrane area (3.14cm^2). Figure 3.4 shows the change in dye concentration in the receptor cell as a function of time for low and high crosslinked samples. The permeability coefficient, P, can be determined from the slope using Eq. (5) for each dye tested with membranes of different mesh sizes. The solute diffusion coefficient, D, can then be calculated using:

$$D = \frac{P\delta}{K} \quad (3.6)$$

where δ is equilibrium membrane thickness (as obtained from the swelling cell ellipsometer experiments) and K is the partition coefficient. The equilibrium thickness values are measured as 1660 nm and 1820 nm, for high and low crosslinked membranes. *K* values are obtained as 0.048 and 0.041 for AY ad Phl, respectively. Table 2 shows the P and D values obtained for different dyes and mesh sizes.

Table 3.2. Permeability and diffusion coefficients of model dyes tested on membranes with different mesh sizes

Sample	**Mesh Size(nm)**	**Dye**	**Temperature(°C)**	**Permeability Coefficient (x10^{-5} cm/s)**	**Diffusion Coefficient (x10^{-7} cm^2/s)**
HX	0.575	Phl	25	1.5	0.61
LX	0.651	Phl	25	3.13	0.95
HX	0.575	AY	25	1.27	0.44
LX	0.651	AY	25	4.48	1.71
LX	0.651	AY	50	8.3	3.16
LX	0.651	AY 4PAP	25	1.25 0.30	0.24 0.008

Critical dye dimensions that affect the permeation of the dye molecules through the polymer are the solvent excluded diameter and the total polar surface area. The former is related to size exclusion and the relative diameter compared to mesh size of the polymer affects diffusion of the dye. On the other hand, total polar surface area which is the sum of surface areas of all polar groups is related to the hydrophilicity of the polymer; larger surface area indicating increased hydrophilicity. Solvent excluded sizes of AY and Phl are reported as 197.179 Å^3 and 90.42 Å^3, and total polar surface areas are134.06 Å^2 and 60.69 Å^2, respectively [81]. Comparing the values, AY molecules are larger and more hydrophilic than Phl molecules. The mesh size of the polymer is another factor that affects the permeation of the dye. As the mesh size increases the dye molecules can easily diffuse through the membrane due to increased free volume, therefore higher

permeation rates are observed. Under the same conditions, both AY and Phl dyes have larger permeability and diffusion coefficients in low crosslinked (LX) polymer membranes compared to that of the highly crosslinked (HX) membranes, with smaller mesh size. For the LX membranes with large mesh size, permeation coefficient of the larger dye AY is higher than that of the smaller dye Phl. Although polarity is also effective in improving the permeation of AY dyes in hydrophilic polymer, the main factor is the interplay between different entropies. While the entropy of mixing favors the smaller dyes to diffuse inside the pores of the polymer, the loss of conformation entropy leads to faster diffusion of larger dye molecules through the polymer mesh. Therefore, the higher permeation and diffusion coefficients of AY compared to that of Phl molecules in the LX membranes can be explained by loss of conformation entropy favoring faster diffusion of AY molecules through the p(HEMA) mesh. On the other hand, for the HX membranes, AY had slightly lower permeation coefficient compared to Phl. This can be attributed to the smaller mesh sizes of the HX membranes. For dyes that are larger than the mesh size, size exclusion principle applies and the polymer acts as a molecular sieve, permitting only smaller dyes. For the two dyes studied here, the size of the larger dye AY is comparable to the mesh size of the highly crosslinked polymer membrane, leading to significantly reduced permeation of AY, compared to Phl which is smaller than the mesh size. The effect of temperature on the diffusion rate of the AY dye is studied by repeating the same experiments at different temperatures. An increase in temperature of 25ºC, increased the diffusion coefficient in accordance with $D \propto \exp(-\frac{1}{RT})$ [99]. The selectivity of the membranes with respect to permeant polarity is tested using AY and 4-Phenylazodiphenylamine (PADPA), which is similar to AY in size but significantly more hydrophobic, lacking the -OH and -NO2 groups of AY. The feed solution used in the permeation studies, contains both dyes with same concentrations. Figure 3.5 shows the individual permeation rates of AY and PADPA dyes through LX membranes. Although both dyes are permeable, faster permeation of AY molecules can be attributed to the polarity of the hydrophilic AY molecules. The selective nature of the hydrophilic membranes is also confirmed by permeation coefficient of AY that is observed to be approximately 30 times larger than that of PADPA as shown in Table II. The selectivity of the membranes with respect to polarity can further be improved by adding polar functionalities to the polymer, which increase interaction with the polar dye molecules.

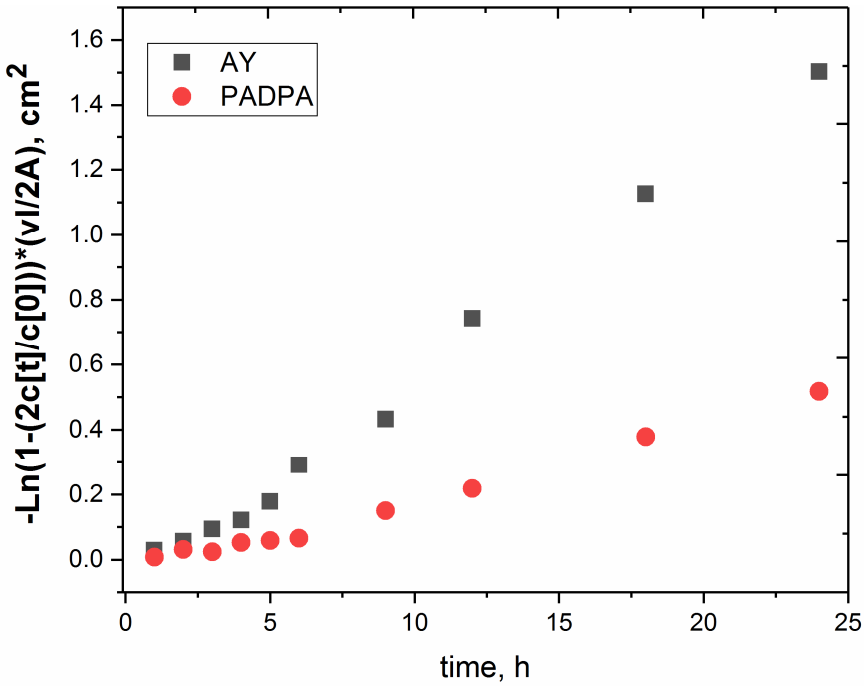

Figure 3.5. Plot of eq. (5) as a function of time showing the selectivity of the LX membranes tested with AY and PADPA dyes simultaneously

CHAPTER 4. HYBRID PH RESPONSIVE MEMBRANES

4.1. Introduction

Utilization of membranes for separation of macromolecules has gained wide interest in the last decade, especially after the development of smart membranes with tunable properties for improved separation performance. Variations in permeate water flux were observed at different pH values, confirming the pH responsive behavior of the membrane. Changes in the pore size due to swelling of the polymer facilitated size selective separation of nanoparticles. Experiments performed using PAA showed that the shape of the permeate was a factor in permeation, with flexible, compact structures having higher flux. Upon increasing the pH, the swollen polymer in the pores led to slower permeation of the PAA molecules independent of the structure, though the effect was more pronounced on rigid, extended structures. Permeation studies of the model protein BSA showed that in addition to pore size charge the BSA molecules and the membrane pores interaction significantly affected the permeation rate of BSA. The ability to tune the pore size through pH for the improved control of permeability, as demonstrated in this work, will enable the utilization of these smart membranes in challenging macromolecule separation applications.

4.2. Experimental Methods

4.2.1. pH Responsive Membrane Preparation

Membranes were fabricated by conformally coating the pores of track etched AAO membranes with pH responsive polymers via the iCVD technique (Figure 4.1). Polymer depositions on the AAO membranes were performed in a custom-built iCVD chamber at a base pressure of 5 mTorr. Monomer vapors, initiator and the N_2 gas were delivered to the chamber through different ports. The monomer vapor flowrates were controlled by needle valves, whereas the flowrates of initiator and N_2 gas were controlled by mass flow controller. A heated filament array was placed above the sample stage for thermal decomposition of the initiator molecules. The substrate temperature was controlled by backstage cooling throughout the deposition process. For the depositions reported

in this study, the flowrates used were 1.4 sccm for MAA, 0.15 sccm for EGDMA, 1.8 sccm for TBPO and 1 sccm for N_2. The pressure of chamber was adjusted to 370 mTorr during deposition. The filament and substrate temperatures were kept at 200ºC and 30ºC, respectively during deposition. For conformal coating of the pores, the ratios of the partial pressures of monomers to the saturation pressures were kept around 0.2 to ensure low surface monomer concentration and slower deposition rates.

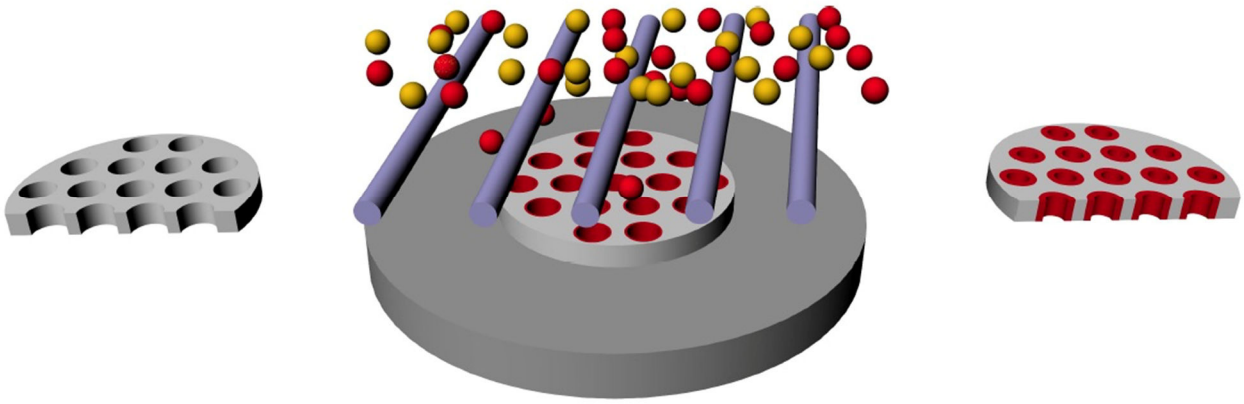

Figure 4.1. Schematic of the pH responsive membrane preparation. The uncoated AAO template is put on the stage in the iCVD chamber where the deposition takes place

4.2.2. Charging of Membranes

In order to impart excess charge to the membrane pores, graphene oxide-NH_2 flakes were attached to the inner walls of the pores after polymer coating. 1 mg/mL of GO-NH_2 flakes was first dispersed in DI water using sonicator for 6 hours. Membranes were then immersed in solution for 24 hours, followed by washing in DI water and drying at room temperature for 24 hours.

4.2.3. Membrane Characterization

The chemical composition of the polymers coated inside the AAO pores was studied by Fourier transform infrared (Thermo-Nicolet iS10 FTIR) spectroscopy. FTIR spectra were acquired over the range of 400-4000 cm^{-1} with a 4 cm^{-1} resolution for 64 scans. The membrane surface and the pores were imaged using a Field Emission Scanning Electron Microscope (Zeiss, SUPRA VP 35) at 4 kV accelerating voltage. The contact angle measurements of the uncoated and coated AAO templates were performed using a tensiometer (KSV Sigma70). The AAO templates used in this study were hydrophilic with a surface contact angle of 69 degrees. The surface zeta potential of

the uncoated and coated AAO templates were determined using a zeta potential analyzer (Zeta sizer ZS, Malvern).

The effect of pH on the swelling of the polymer films was studied by monitoring the real-time thickness changes of the p(MAA) thin films using a spectroscopic ellipsometer (M2000 Spectroscopic Ellipsometere J.A. Wollam Co. Inc.). The real-time swelling experiments were performed at pH 3 and pH 9 in a heated liquid cell with nominal angle of incidence of 75 degrees. The sample was placed in the liquid cell, which was then filled with water, and the thickness of the film was measured continuously throughout this process. The swelling percentage of the films was then calculated using $((T_f-T_0)/T_0 \times 100)$, where T_f is the thickness at the swollen state and T_0 is the dry state thickness.

Permeation Experiments

Prior to permeation experiments, membranes were compacted by filtering deionized water at 3 bars for 30 minutes. Permeation of water and three different permeants (Polystyrene nanoparticles, Poly Acrylic Acid macromolecules, BSA proteins) through the membranes and the effect of the pH on the membrane performance were investigated. The DI water permeation experiments were performed at pH 3 and pH 9, at room temperature and at a pressure of 1 bar.

Permeation of nanoparticles: 5µL of polystyrene beads was mixed with 100 mL of DI water and the pH of solution was adjusted to pH 3 and pH 9 using NaOH and HCl. Hydrodynamic permeation tests were performed in a dead-end Sterlitech cell at room temperature. The feed solution was pressurized with N_2 at 1 bar. Dynamic light scattering (Malvern Instruments, Ltd.) measurements were performed to determine particle sizes before and after filtration.

Permeation of macromolecules: 100 mg Poly Acrylic Acid (PAA), with molecular mass of 100 kDa, was first dissolved in 200 mL DI water and the pH of solution was adjusted using HCl and NaOH. The permeability tests were performed as explained before. The permeant weight was measured periodically throughout the experiment and the permeate flux was calculated.

Permeation of a model protein: To study the protein permeation through the functionalized pH responsive membranes hydrodynamic permeation and diffusion tests were performed. For hydrodynamic permeation tests, 15 mg of BSA protein was dissolved in 150 mL DI water whereas

for diffusion tests, 100 mg of BSA protein was dissolved inside 100 mL of the DI water. The pH of solutions was adjusted to pH 3 and pH 9 using NaOH and HCl. The hydrodynamic permeation tests were performed as detailed before. Diffusion studies of BSA through the AAO membranes were performed in a side-by-side diffusion cell with an effective membrane area of 0.785 cm^2 at atmospheric pressure. One cell was filled with BSA feed solution and the other cell was filled with DI water and the solutions in both chambers were stirred continuously by magnets throughout the experiments. The experiments were performed at pH 3 and pH 9 and the pH of both the feed and the permeate chambers was maintained the same. BSA concentration in permeate side was periodically monitored by taking 2 mL of solution and characterizing using a NanoDrop 2000/2000c spectrophotometer (Thermo Fishe Scientific).

4.3. Results and Discussion

FTIR analysis of polymers on the AAO template confirms the successful copolymerization of MAA with EGDMA as shown in Figure 4.2. The band at 1380 cm^{-1} corresponds to the methyl bending vibration, whereas the band at 1430 cm^{-1} corresponds to CH_3 deformation mode. C-H stretching vibration appears at 2850-3000 cm^{-1}. The bands at 1700 cm^{-1} and 1730 cm^{-1} arise from the C=O stretching vibrations of MAA and EGDMA, respectively [68].

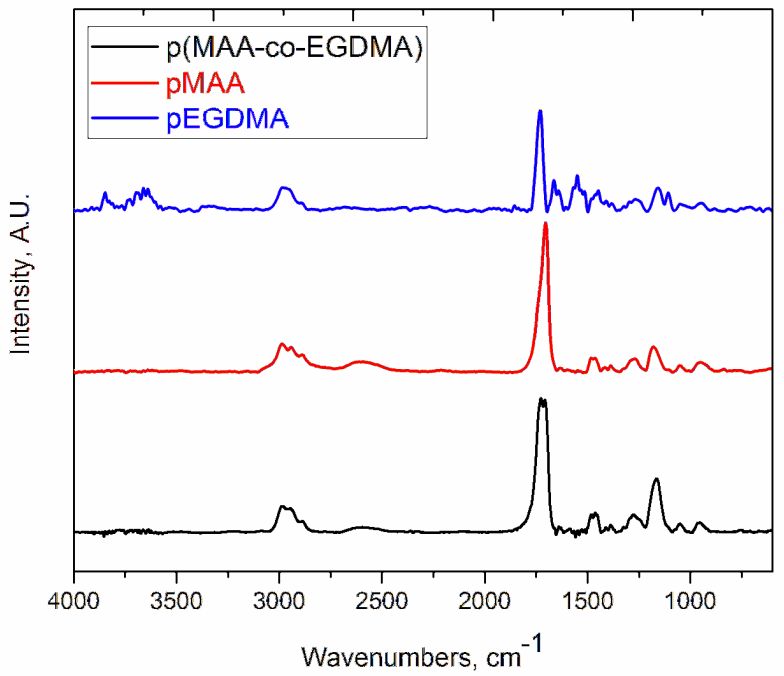

Figure 4.2. FTIR spectra of the p(MAA-co-EGDMA) coating on the AAO. Spectra of p(MAA) and p(EGDMA) are also shown for comparison. The doublet carbonyl band of the copolymer film confirms copolymerization of MAA and EGDMA monomers

The EGDMA content of the coatings is calculated from the band areas of the C=O bonds and is estimated to be approximately 46%. The real-time ellipsometry studies performed on p(MAA) thin-films with 46% EGDMA content show that the polymer film swells 38% at pH 9 while the swelling is only 5% at pH 3, confirming the pH dependent behavior of the p(MAA) polymer even at these high crosslink ratios. The pH dependent physical changes the p(MAA) polymer undergoes are attributed to the electrostatic repulsion among the chains. At pH values higher than the pKa of the p(MAA), which is a weak polycarboxylic acid with pKa of 6-7, the ionizable carboxyl groups dissociate into carboxylate ions carrying a negative charge.

The electrostatic repulsion among these segments leads to the extension of the chains, thus swelling of the polymer. At lower pH values, on the other hand, the acidic groups will be protonated and will not be ionized. For the unionized system, the hydrophobic interactions will dominate, resulting in the exclusion of water molecules and thus collapse of the polymer chains [100, 101].

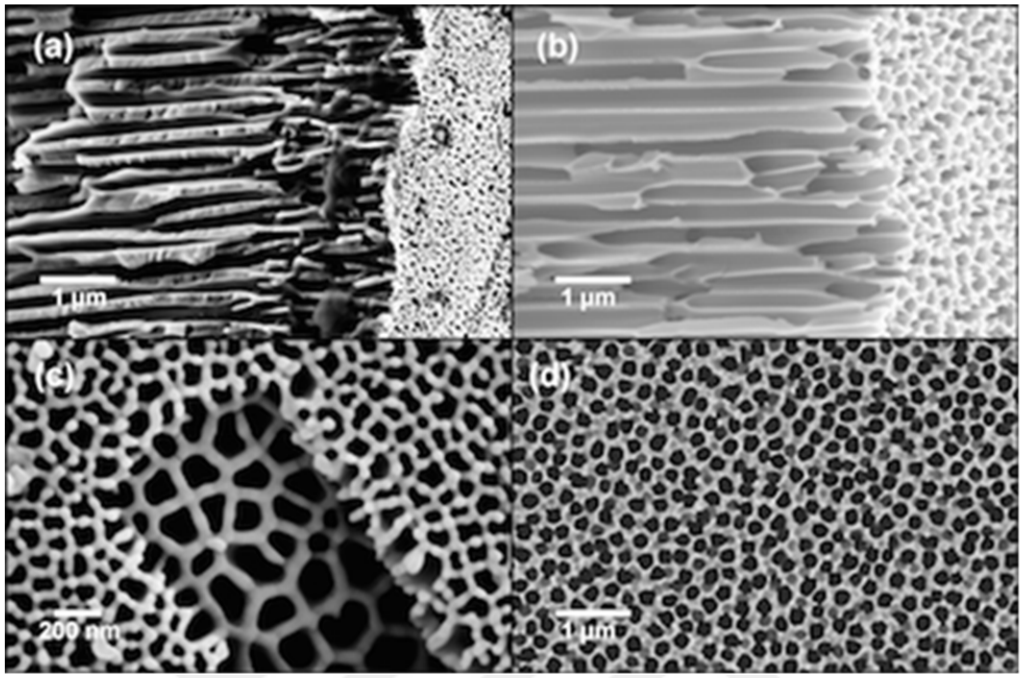

Figure 4.3. SEM images of cross-section of (a) polymer coated and (b) uncoated AAO and top-view of (c) polymer coated and (d) uncoated AAO. Polymer coating on the pore walls is visible in the cross-sectional view, confirming the penetration of the polymer into the AAO membrane

The hybrid membranes are fabricated by coating the inner pores of the AAO templates with the pH responsive p(MAA) polymer. The SEM images of the uncoated and coated membranes are shown in Figure 4.3. The polymer film thickness on the pore walls is estimated by comparing the average pore sizes before and after the polymer deposition. The average pore size is calculated from the SEM images using the Image J software. The software uses the differences in the contrast to determine the location and the size of the pores [102]. Histograms of the pore sizes on the uncoated and coated AAO templates are shown in Figure 4.4. The average pore sizes on uncoated and coated AAO template (in the dry state) are calculated as 110±13 nm and 85±20 nm, respectively, indicating a polymer film thickness of approximately 25 nm. Furthermore, the coated templates have a wider distribution of pore sizes compared to the uncoated templates.

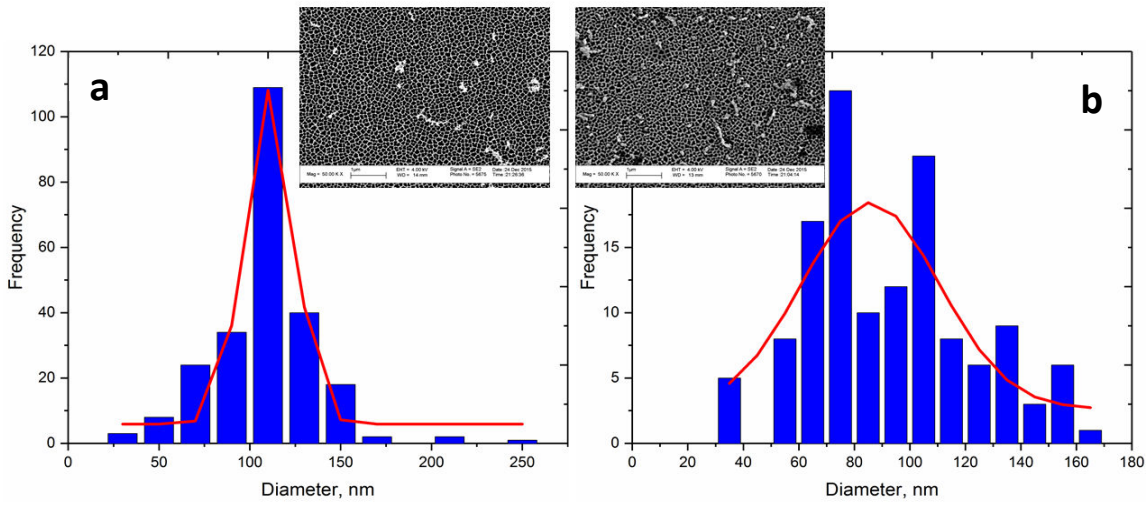

Figure 4.4. Pore size distribution of (a) uncoated AAO and (b) polymer coated AAO template as obtained from SEM images. The average pore size of the uncoated AAO is calculated to be as 110±13 nm, whereas the coated template has an average pore size of 85±20nm with a wider distribution of pore sizes

The effect of the polymer coating on the water permeation performance of the membranes was investigated. The water permeabilities of uncoated and polymer coated AAO membranes at acidic and basic conditions are determined via measuring the flux of DI water passing through the membrane at different applied pressures (Figure 4.5).

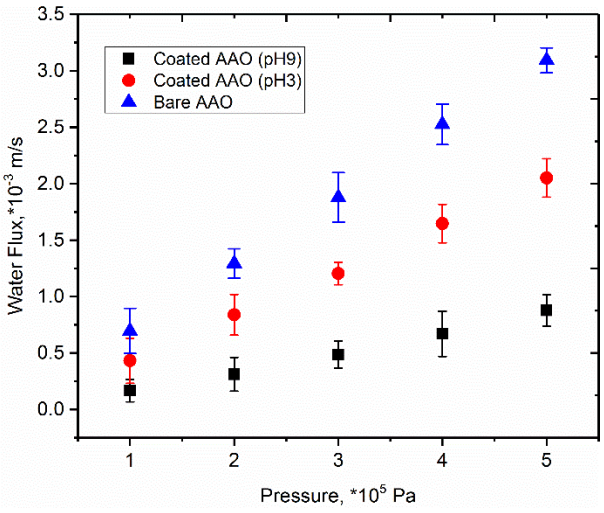

Figure 4.5. Water permeabilities of uncoated AAO template and p(MAA-co-EGDMA) coated AAO at pH 3 and pH 9 measured at different pressures. Highest permeabilities are obtained with the uncoated template due to larger pore size. On the other hand, for the coated templates permeabilities decreased at pH 9 compared to pH 3, due to the swollen pH responsive p(MAA-co-EGDMA) at high pH, decreasing the effective pore size

The higher water permeabilities obtained at pH 3 compared to that at pH 9 can be related to the larger pore sizes at low pH values due to the shrinking of the polymer layer on the pore walls. The highest water fluxes are observed with uncoated AAO membranes due to the larger pore sizes in the absence of polymer coatings. On the other hand, as the applied pressure increased, water flux increased for all membranes. The strongest pressure dependency was observed with the uncoated AAO and the dependency decreased as the pore size increased allowing higher flux. To calculate the pore size of membranes at swelling and collapsed states, Hagen-Poiseuille (HP) equation was used:

$$J = \frac{V}{A\Delta t} = \frac{\varepsilon r^2}{8\eta}\frac{\Delta P}{L} (\varepsilon = n\pi r^2 / A) \quad (4.1)$$

where V is the volumetric flow rate, A is the membrane area (0.785 cm^2), J is the flux, n is the number of pores per unit area of membrane (which is measured by imageJ software as $8x10^8$ per cm^2), r is the average pore radius, η is the water viscosity ($8.9x10^{-4}$ Pa.s), ΔP is the pressure difference across the membrane, and L is the average length of the pores (50 μm). From HP equation the calculated pore size of p(MAA-co-EGDMA) at pH 9 is approximately 83 nm and at pH 3 is 106 nm and for uncoated AAO template, the calculated pore size is 118 nm. The pore sizes calculated using HP formulation are in good agreement with the pore sizes obtained using the Image J software. The gating performance of the membranes was investigated via filtration experiments of polystyrene beads at different pH conditions. DLS measurements performed at pH 3 and pH 9 before the filtration experiments confirmed that the pH did not have a significant effect on the nanoparticle size. The zeta potentials of the nanoparticles, on the other hand, were measured as 3.97 mV and -38.5 mV at pH 3 and pH 9, respectively. The size distributions of the nanoparticles (NP) in the feed and permeate solutions as obtained by DLS measurements are shown in Figure 4.6. The average size of the NPs in the feed solution was measured to be within the range of 50-190 nm. The average size of the NPs on the permeate side, on the other hand, was measured to be within the range of 37-106 nm and 29-91 nm, after filtration by membranes at pH 3 and pH 9, respectively.

The results show that at pH 3, the polymer in the collapsed state allows larger NPs to permeate through the membrane pores due to larger pore size of approximately 106 nm. On the other hand, at pH 9 the effective pore size reduces to approximately 83 nm due to swollen polymer layer,

impeding the permeation of NPs with larger sizes. At high pH, electrostatic repulsion between the polymer coating with negative charge and the negatively charged surface of the nanoparticles (with zeta potential of -38.5 mV) should also be considered. However, in the filtration experiments, the high pressure applied would have a stronger impact on the filtration of nanoparticles than the electrostatic interaction. Therefore, the rejection of larger nanoparticles at pH 9 can be attributed mainly to the reduced pore size due to swollen polymer. These observations confirm that the size of the filtrated permeants can be controlled by tuning the pH of the medium.

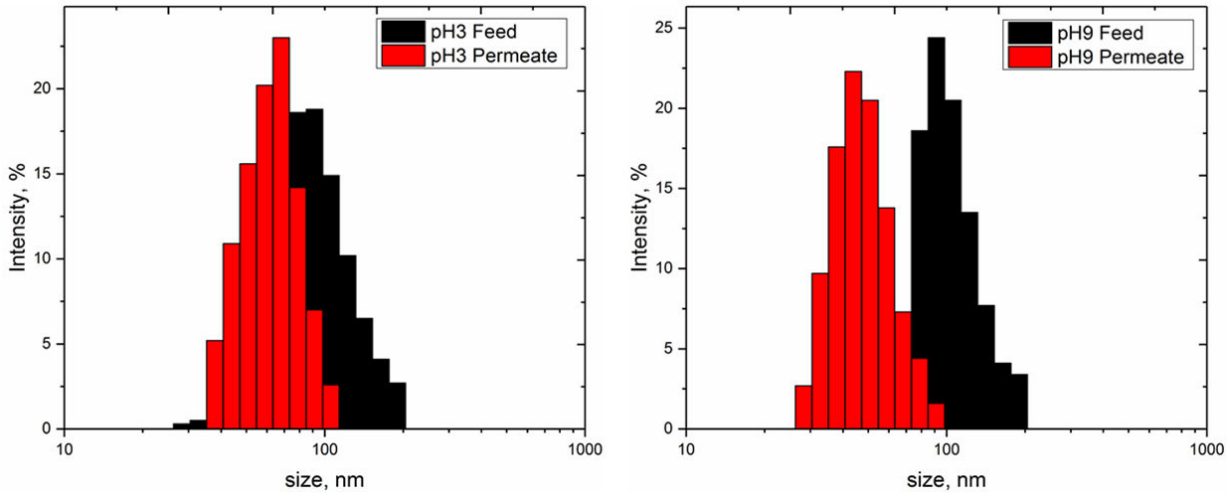

Figure 4.6. DLS analysis of the feed and permeate solutions at (a) pH 3 and (b) pH 9. The average size of permeates at pH 3 is larger than that at pH 9, where the pore openings are narrower due to the swollen polymer

In addition to the PS NPs, permeation of PAA molecules (with molar mass of 100 kDa) through the membranes at different pH conditions was also investigated to exploring the effect of permeate shape on the permeation. PAA is reported to exhibit pH dependent conformational changes above a molar mass of 16.5 kDA [103]. Figure 4.7 shows the flux of PAA solution as a function of time through uncoated and polymer coated membranes at pH 3 and pH 9 obtained by the high-pressure filtration experiments. Initially there is a fast drop in the flux during the first 40 minutes of the experiment, after which the flux levels off. This trend is observed for all samples and this reduction in flux can be attributed to the accumulation of the PAA molecules at the pore openings because of applied pressure. The sharpest decrease is observed with the coated membranes at pH 9 where the swollen polymer may trap the PAA molecules. The highest steady-state flux values are obtained with uncoated AAO membranes due to uncoated, larger pores, with highest flux observed

at pH 3. PAA exhibits a pH-dependent conformational change, displaying a coil-to- globule transition at pH 5. At high pH, deprotonation of the carboxylic groups ionizes the polymer and the electrostatic repulsion among the chains leads to an open, coil-like structure [103]. At low pH, PAA is uncharged, adopting a compact, globular conformational structure. This flexible, compact structure can easily diffuse through the pores, resulting in higher permeate flux compared to that at pH 9, where PAA has inflexible, extended, coil shape. Due to this inflexible, coil shape, the PAA cannot easily diffuse through the pores, but instead forms a thick layer on membrane surface, partially clogging the pores. Similar behavior is observed with the responsive polymer coated AAO membranes, where flux is higher at low pH. In addition to the PAA shape, pH response of the polymer coating is another factor that controls the flux. The swollen polymer at pH 9 reduces the pore size, further decreasing the flux. Flux observed at pH 3 with the coated membrane is comparable to the flux of uncoated membrane at pH 9, indicating the significance of permeate shape besides the pore size.

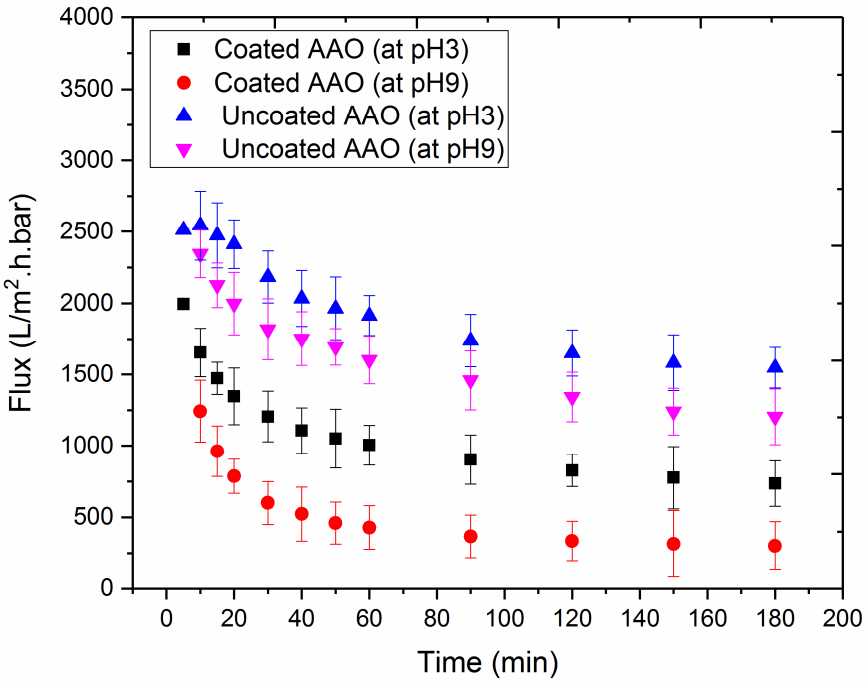

Figure 4.7. Permeate flux of PAA solution as a function of time. The compact structure of PAA at pH 3 facilitates faster permeation, increasing the flux in uncoated membranes. Flux is reduced at coated membranes due to narrower pores. The further decline in the flux at pH 9 is due to the swollen polymer inside the pores

Effects of PAA shape on the diffusion through the membranes are studied using side-by-side diffusion cells. Figure 4.8 shows the concentration of permeated PAA at different pH values as a function of time. Diffusion of PAA molecules is observed to be faster with uncoated AAO membranes, fastest diffusion occurring at pH 3, where PAA adopts a flexible, compact structure. At pH 9, PAA has inflexible, extended structure with reduced permeation rates through the membranes. On the other hand, diffusion of PAA through the coated membranes is slower compared to the uncoated membranes due to reduced pore size. Diffusion is significantly low at pH 9 because of polymer swelling at these high pH values.

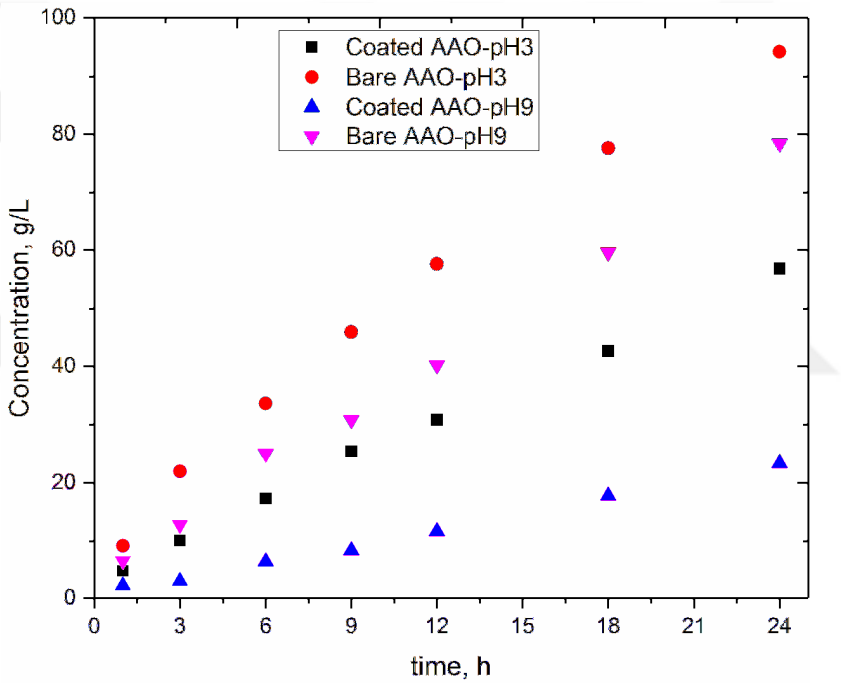

Figure 4.8. Concentration of PAA on the permeate side as a function of time. Diffusion of the PAA molecules is faster through the uncoated membranes, fastest diffusion is observed at pH 3 due to the compact structure of the PAA. In coated membranes, in addition to the PAA structure, polymer swelling also affects the permeation, with faster diffusion observed at pH 3 compared to pH 9

Permeation of a model protein, BSA, through the membranes at different pH conditions was also investigated for further characterization of the membrane performance. Hydrodynamic and diffusion tests were performed using BSA solution as the feed. Effect of membrane surface charge on the permeation of BSA molecules was also investigated using GO-NH_2 functionalized membranes. Figure 4.9 shows FTIR spectra of unfunctionalized and GO-NH_2 functionalized AAO

surfaces. The absorption bands at 1050 cm^{-1} and 1727 cm^{-1} are attributed to C–O in hydroxyl and C=O in carboxyl groups. The bands at 1225 cm^{-1} and 830 cm^{-1} are associated with symmetrical and asymmetrical stretching vibration of ether group [104, 105]. The band at 1609 cm^{-1} is due to the stretching of C=C bond present in GO. The sharp band 1512 cm^{-1} is attributed to the bending vibrations of N-H groups, confirming the attachment of N-H group to the carboxyl group of MAA, and thus functionalization of the surface with the GO-NH_2 groups.

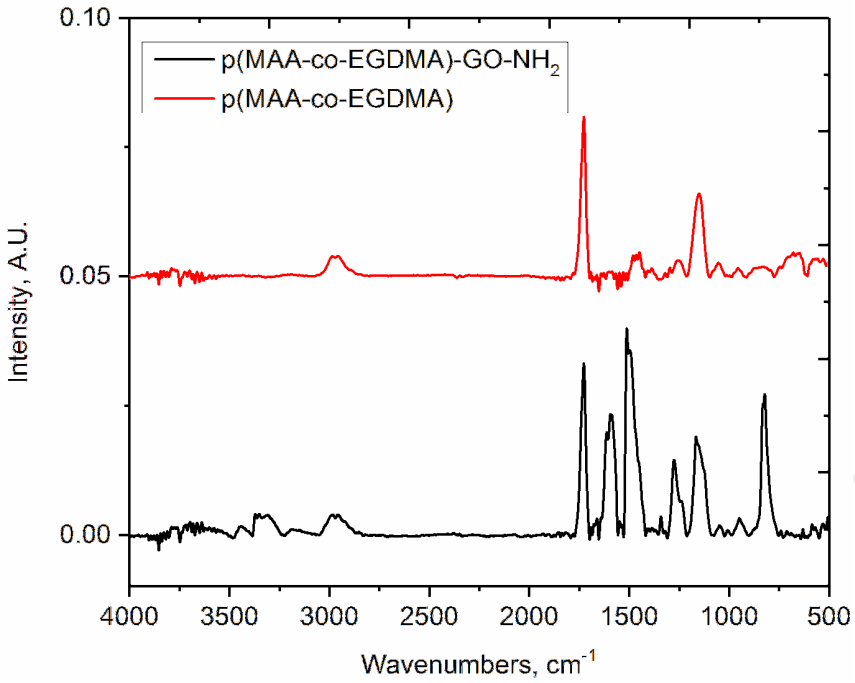

Figure 4.9. FTIR spectra of the p(MAA-co-EGDMA) film and p(MAA-co-EGDMA) film functionalized with -GO-NH2 groups. The bands at 1609 cm-1 and 1512 cm-1 are attributed, respectively, to the stretching of C=C bond present in GO and bending vibrations of N-H groups, confirming successful functionalization of the surface with GO-NH2 groups

Water permeation experiments were performed, initially, to study the effects of GO-NH_2 attachment on the pore size. The water permeability values obtained from these experiments were similar; $0.2x10^{-8}$ m/(Pa.s) for the unfunctionalized and $0.27x10^{-8}$ m/(Pa.s) for the GO-NH_2 functionalized AAO templates, confirming that the attachment of the GO-NH_2 on the pore walls did not significantly reduce the pore size.

The flux of BSA solution in hydrodynamic filtration tests was calculated according to:

$$L_P = m/\rho tAp \tag{4.2}$$

where m is the mass of permeate, with density ρ, collected for time t through the membrane area A at pressure p [106]. Figure 4.10 shows the flux of BSA solution as a function of time at pH 3 and pH 9 through the functionalized and unfunctionalized membranes.

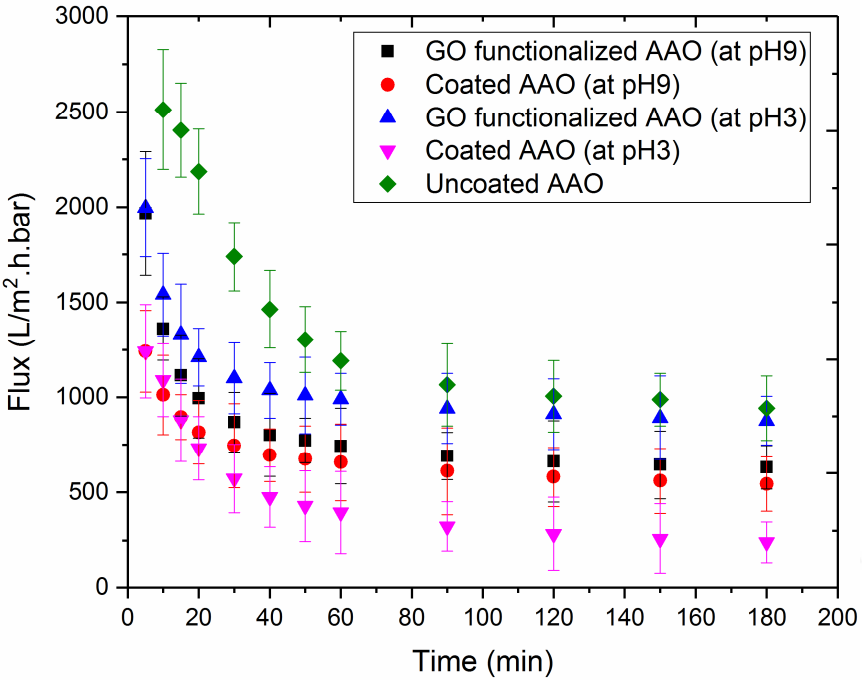

Figure 4.10. Permeate flux of BSA solution as a function of time. The lowest flux was obtained with the polymer coated membranes at pH 3 as opposed to pH 9, indicating the adsorption of positively charged BSA on the membrane at pH 3 which leads to clogging of the pores. Introducing positive charges to the membrane with the -GO groups, leads to increased flux at pH 3 due to the electrostatic repulsion between BSA and the polymer. The hydrophilic nature of the -GO groups at pH 9 dominates the permeation mechanisms, resulting in higher flux values for GO functionalized membranes compared to unfunctionalized, overcoming the electrostatic interactions

In all membranes, a sharp decrease in the flux of solution is observed at early times and after approximately 60 minutes the flux reaches a steady state. The decrease in the flux observed in the early stages of filtration can be attributed to the BSA molecules nonselectively attaching on the pore openings initially, reducing the flux. The highest steady state flux is observed at uncoated AAO membranes due to large pore sizes in the absence of polymer coating on the walls. For the polymer coated, unfunctionalized membranes, the flux at pH 3 is observed to be lower than the flux at pH 9. The fact that the flux is lower at pH 3 despite the larger pores due to collapsed polymer

at this low pH value indicates the dominance of another factor. The isoelectric point of BSA protein appears around pH of 4.9 [107], above which BSA becomes negatively charged. At pH 9, there is a strong electrostatic repulsion between the negatively charged BSA and the membrane surface, which is also negatively charged due to the ionization of the carboxylic groups. This repulsion prevents adsorption of the BSA molecules on the pore walls and subsequent clogging of the pores. Furthermore, polymer surface hydrophilicity is increased due to the hydrogen bonding between the ionized carboxyl groups and water molecules at this high pH value, hindering attachment of BSA molecules [108, 109]. On the other hand, at pH 3, the hydrophobic interaction between the positively charged BSA molecules and the neutral polymer surface prompts adsorption of the protein molecules on the walls. Following this initial solute-membrane interaction, solute-solute interactions dominate, leading to further accumulation of BSA molecules on the walls [110, 111]. The filtration experiments indicate that the solute-membrane interactions are more dominant than the pore size effect in controlling the flux of the permeate. Sinha *et al.,* in their study with poly (acrylic acid-co-polyethylene glycol methyl ether methacrylate) based membranes, reported higher rejection of BSA molecules at pH 9 compared to pH 3 [112]. They attributed the increased rejection to the electrostatic repulsion between the BSA molecules and the polymer in the membrane matrix, in addition to the reduced pore size due to swelling of the polymer. However, in this study the higher flux obtained at pH 9 compared to that of pH 3 is attributed to the reduced adsorption of BSA on the pore walls, which reduces pore clogging. This discrepancy between the two studies can be explained by the difference in the pore sizes. In the small pores used by Sinha *et al*., the electrostatic repulsions between the BSA molecules and the polymer will be more dominant, increasing the rejection of negatively charged BSA at pH 9. On the other hand, the size of the pores used in this study is significantly larger than BSA; therefore, the electrostatic interactions will be effective only on the pore walls. These interactions may reduce the BSA attachment on the walls but will not have a strong impact on the BSA flux through the membrane. Functionalization of the polymer with GO–NH_2 particles imparts positive charges to the polymer surface as a result of the protonation of the –NH_2 group and the higher pKa of the amino group[113, 114]. At pH 3, the zeta potential of the polymer is measured as -6.7 mV, whereas the zeta potential of the GO-NH_2 functionalized polymer is 40.16 mV. Similarly, at pH 9, after functionalization with GO-NH_2 the zeta potential of the membranes changed from -39.36 mV to 26.46 mV, confirming that functionalization with GO-NH_2 imparts excess positive charges to the surface. At

pH 3, both BSA and the polymer surface are positively charged so the electrostatic repulsion forces reduce adsorption of BSA molecules. At pH 9, on the other hand, negatively charged BSA molecules adsorb readily on the positively charged membrane surface, significantly reducing the flux compared to that at pH 3. The hydrophilic nature of the graphene oxide particles leads to the higher fluxes observed both at pH 3 and pH 9 compared to unfunctionalized membranes without GO [115, 116]. Following the high-pressure filtration experiments, diffusion of BSA through the membrane pores were studied. Figure 4.11 shows the cumulative concentration of BSA molecules diffused through the membrane at pH 3 and pH 9.

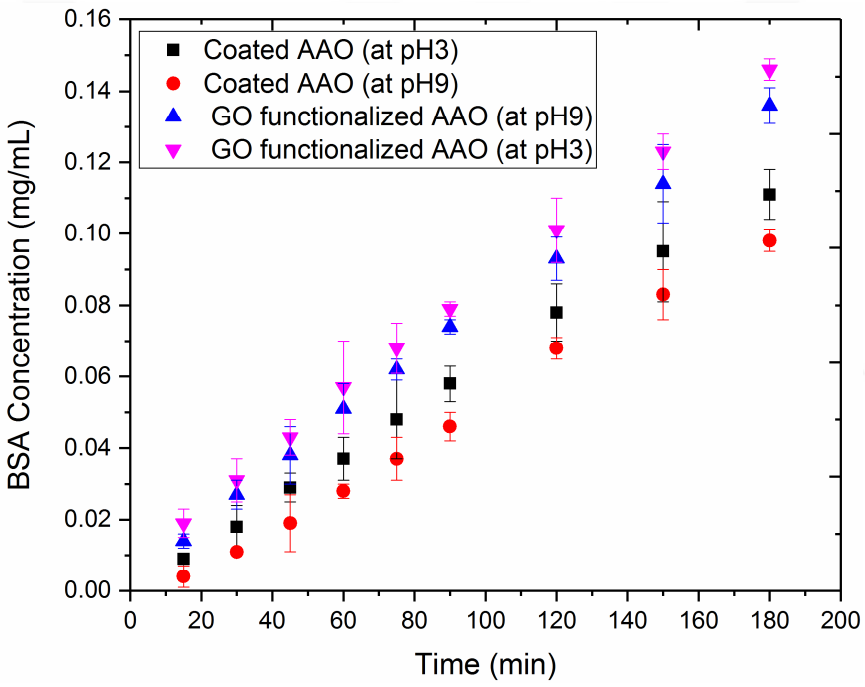

Figure 4.11. BSA concentration in the permeate side as a function of time obtained from diffusion experiments. For both polymer coated AAO and GO functionalized AAO, concentration increase of BSA is similar at pH 3 and pH 9, indicating the contribution of other factors

Depending on the pH of the medium, BSA protein adopts a different conformational structure [117, 118]. Within the pH range of 4 to 9, the shape BSA molecule attains is independent of pH and concentration [118]. In the compact state at pH 4-9, the length of a BSA molecule is 8.3 nm, whereas in the extended form at pH 3 it is 26.7 nm [117]. Permeation of BSA at pH 3 is like that at pH 9, despite the larger size of BSA at low pH. This is due to the larger pore size at pH 3 where the polymer on the walls is in the collapsed state, leading to faster diffusion [119]. In addition to

the shape of the protein, the charges of the BSA and the polymer surface also determine the diffusion of the protein through the membrane. At pH 9, the electrostatic repulsion forces between the negatively charged BSA molecules and the polymer hinder the diffusion of BSA through the membrane pores. Furthermore, the reduced pore sizes at pH 9 due to the swelling of the polymer, impedes the BSA diffusion. At pH 3 adsorption of positively charged BSA on the neutral polymer surface is expected which would reduce the diffusion of the protein, however similar diffusion rates with pH 9 suggests that the conformational structure of the protein has a higher impact on the permeation than the charge. Similar pH dependency is observed with the GO functionalized membranes, though the overall BSA concentration is higher compared to that of the unfunctionalized membranes, which can be attributed to the increased hydrophilicity of the membranes in the presence of GO particles [116, 117]. Overall, it is concluded that charge difference has a stronger impact on the diffusion rates than the swelling of the polymer, which affects the pore size.

CHAPTER 5. JANUS MEMBRANES

5.1. Introduction

Janus membranes with sides that respond differently to pH changes in the environment were developed as gating membranes for controlled permeation of protein molecules. Gating response of these membranes was achieved by coating both sides of the membranes with different pH responsive polymers using iCVD. By tuning the monomer surface concentrations, non-conformal coatings with keyhole shapes were obtained which facilitated blocking of the pores upon swelling of the polymer in response to pH changes. Through separate control of the pH on different sides of the membranes, diffusion of the BSA molecules through the membranes could be blocked, delayed and released on demand.

5.2. Experimental Methods

5.2.1. Membrane Preparation

p(MAA-co-EGDMA) and p(4VP-co-EGDMA) were coated separately on two sides of the track etched AAO membranes via non-conformal iCVD to obtain the key-hole structures at both ends of the pores. For this purpose, first, AAO templates were coated with p(MAA-co-EGDMA) on one side and the other side was coated with p(4VP-co-EGDMA), subsequently. Monomers MAA and EGDMA were vaporized inside metal jars at 40 ^{o}C and 85 ^{o}C, respectively, and 4VP and TBPO were kept at room temperature. For p(4VP-co-EGDMA), 4VP and EGDMA flowrates were 7 and 0.15 sccm, respectively while for p(MAA-co-EGDMA), MAA and EGDMA flowrates were 1.73 and 0.16 sccm, respectively. The flowrates of N_2 and initiator were fixed at 1 sccm. The filament and substrate temperatures were kept at 240^{o}C and 25^{o}C, respectively during deposition. Finally, to get the key-hole structures, depositions were performed at 600 mTorr and at 500 mTorr, for p(4VP-co-EGDMA) and p(MAA-co-EGDMA) coatings, respectively. The thickness of the coatings on both openings was approximately 60 nm as measured by SEM.

5.2.2. Membrane Characterization

The chemical composition analysis of the polymers coated inside the AAO pores was performed by Fourier transform infrared (Thermo-Nicolet iS10 FTIR) spectroscopy in normal transmission mode. FTIR spectra were acquired over the range of 400-4000 cm^{-1} with a 4 cm^{-1} resolution for 64 scans. The membrane pores are imaged using a Field Emission Scanning Electron Microscope (Zeiss, SUPRA VP 35) at 4 kV accelerating voltage. EDS analysis was performed to determine the depth of the polymer coating inside the pores at 10kV accelerating voltage and 8.5mm working distance.

The swelling of the polymer films at various pH values was measured in a heated liquid cell with a nominal angle of incidence of 75 degrees by using a spectroscopic ellipsometer (M2000 Spectroscopic Ellipsometer J.A. Wollam Co. Inc.). The changes in the thickness of the films were monitored real-time for 60 minutes at room temperature. The Cauchy model was used to fit the thickness data at wavelengths ranging from 315 to 718nm. The swelling percentage was calculated using $((t-t_0)/t_0)\,x100$, where t is the thickness at the swollen state and t_0 is the dry state thickness.

5.2.3. Permeation Experiments

Diffusion studies of BSA through the Janus membranes were performed at 4 ºC in a side-by-side diffusion cell with an effective membrane area of 0.785 cm^2 and a chamber volume of 5mL. 1mg/mL BSA in 10mM PBS buffer solution was filled in feed side while the permeate side was filled with 10mM PBS buffer solution and the solutions in both cells were stirred continuously by magnets throughout the experiments. The experiments were performed at pH 3 and pH 9 to control the swelling of the polymers on the feed or the permeate sides and activate the gating response. BSA concentration in the feed and permeate sides was measured using a NanoDrop 2000/2000c spectrophotometer (Thermo Fishe Scientific) at specific time intervals. Diffusion studies with rose Bengal is performed in a 50mL PermeGear side-bi-side diffusion cell. 150 mg of dye is dissolved in 100 mL of DI water and added into the feed side of the cell, whereas the permeate side contained only DI water. Experiments are performed at pH3 and pH9 and the diffusion of the dye molecules are observed via the color change in the permeate side.

5.3. Results and Discussion

FTIR spectra of the p(4VP-co-EGDMA) and p(MAA-co-EGDMA) thin films are shown in Figure 5.1. The bands at 2980 and 2920 cm^{-1} belong to CH_2 asymmetric and symmetric stretching modes, respectively for p4VP [120]. The absorption bands at 1600, 1560, 1500 and 1415 cm^{-1} correspond to vibration of pyridine ring [121] . The absorption bands at 1070 and 960 cm^{-1} indicate in-plane and out of -plane rings C-H bending, respectively [120, 121]. The bands at 1730 cm^{-1} arise from the C=O stretching vibrations of EGDMA [68]. The band at 1380 cm^{-1} corresponds to the methyl bending vibration, whereas the band at 1430 cm^{-1} corresponds to CH_3 deformation mode. C-H stretching vibration appears at 2850-3000 cm^{-1}. The bands at 1700 cm^{-1} and 1730 cm^{-1} arise from the C=O stretching vibrations of MAA and EGDMA, respectively. FTIR results show successful copolymerization of MAA and 4VP with EGDMA.

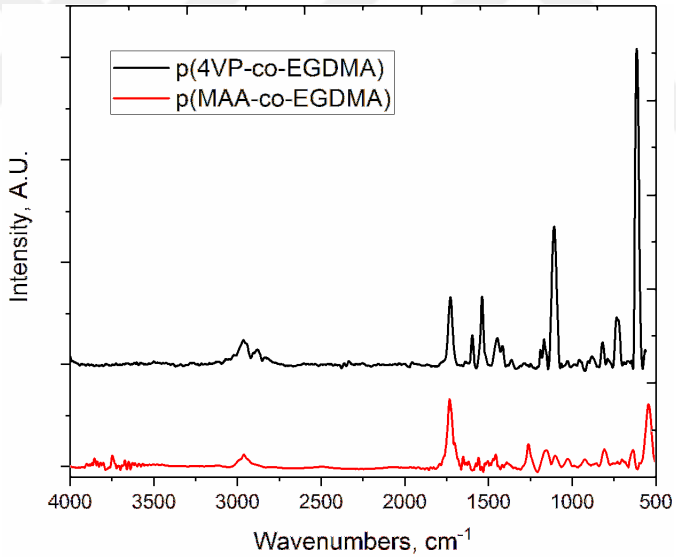

Figure 5.1. FTIR spectra of the p(4VP-co-EGDMA) and p(MAA-co-EGDMA) thin films coated on different sides of the AAO membranes

Figure 5.2 shows SEM images of p(4VP-co-EGDMA) coatings deposited under different deposition conditions for the fabrication of conformal and non-conformal coating and key-hole structures. Coatings with varying degrees of conformality could be achieved by changing the P_m/P_{sat} values from 0.33 to 0.16 (Figure 5.2). The keyhole structure was obtained by maintaining the P_m/P_{sat} value at 0.24. At high P_m/P_{sat} value of 0.33 in the non-conformal regime, the fast deposition rates result in the formation of a thick polymer layer on top of the pores (Figure 5.2(a)

and 2(b)). On the other hand, at the P_m/P_{sat} value of 0.16, deposition rate is significantly slower, enabling precursor diffusion inside the pores, leading to conformal coating of the pores as seen in Figure 5.2(c). The gating effect as reported in this study is achieved by setting the P_m/P_{sat} ratio to 0.24 in order to obtain non-conformal coatings at the pore openings. By keeping the P_m/P_{sat} ratio less than 0.33 and film thickness below 200 nm, keyhole shaped coatings are achieved (Figure 5.2(d)) as opposed to thick polymer layer on top. Figure 5.2(e) and 2(f) show the pore openings with non-conformal, keyhole shaped polymer coating. For p(MAA-co-EGDMA) coatings, keyhole structures were obtained by performing the iCVD depositions at P_m/P_{sat} value of 0.2. The penetration depth of the polymer coating within the pores on both sides is investigated by EDS analysis. The SEM image and the EDS analysis of the cross-section of the Janus membrane are shown in Figure 5.3 (a) and (b) respectively. In the EDS analysis, C signal from the polymer and Al signal from the AAO template are monitored at different locations along the pore depth. A significant decline in the C signal at approximately 1800 nm is observed indicating a sharp thickness change in the polymer coating on both sides due to non-conformal coating. The fact that the C signal intensity does not completely disappear shows that the polymer coating could penetrate deeper into the pores, but the bulk of the polymer coating remains within the 1800nm depth. It should be noted that C exists in the vacuum system, therefore, C signal also involves C from the environment. However, this background C is constant throughout the pore depth, therefore the sharp decline in the C amount is attributed to the polymer. At the low process pressures maintained during iCVD depositions of the membranes, the diffusion of the monomer and radical molecules in the pores is expected to be in the Knudsen regime, which assumes collisions of the precursor molecules with the pore walls dominate collisions among the precursor molecules. As a result, the step coverage, S_x, is directly affected by the aspect ratio of the surface and the sticking coefficient of the precursor and is defined as [80]:

$$S_x = \frac{r_0 - r_x}{r_0 - r_t} \tag{5.1}$$

where r_x is the pore radius at a distance x from the top, r_0 is initial pore radius and r_t is pore radius at the top after polymer coating. The pore profile which is determined by the polymer thickness as a function of depth in non-conformal iCVD depositions is given as [80]:

$$r_x = r_0 - S_L^{\left(\frac{x}{L}\right)^2}(r_0 - r_t) \tag{5.2}$$

where S_L is the step coverage at L and L is the depth of the polymer coating in the pore [80]. The initial pore radius r_0 is taken as 50 nm and r_t is measured as 20±5 nm on the SEM image of p(4VP-co-EGDMA) on side II. The pore radii, r_x, at different depths in the pore are measured on the SEM images of the cross-section of side II.

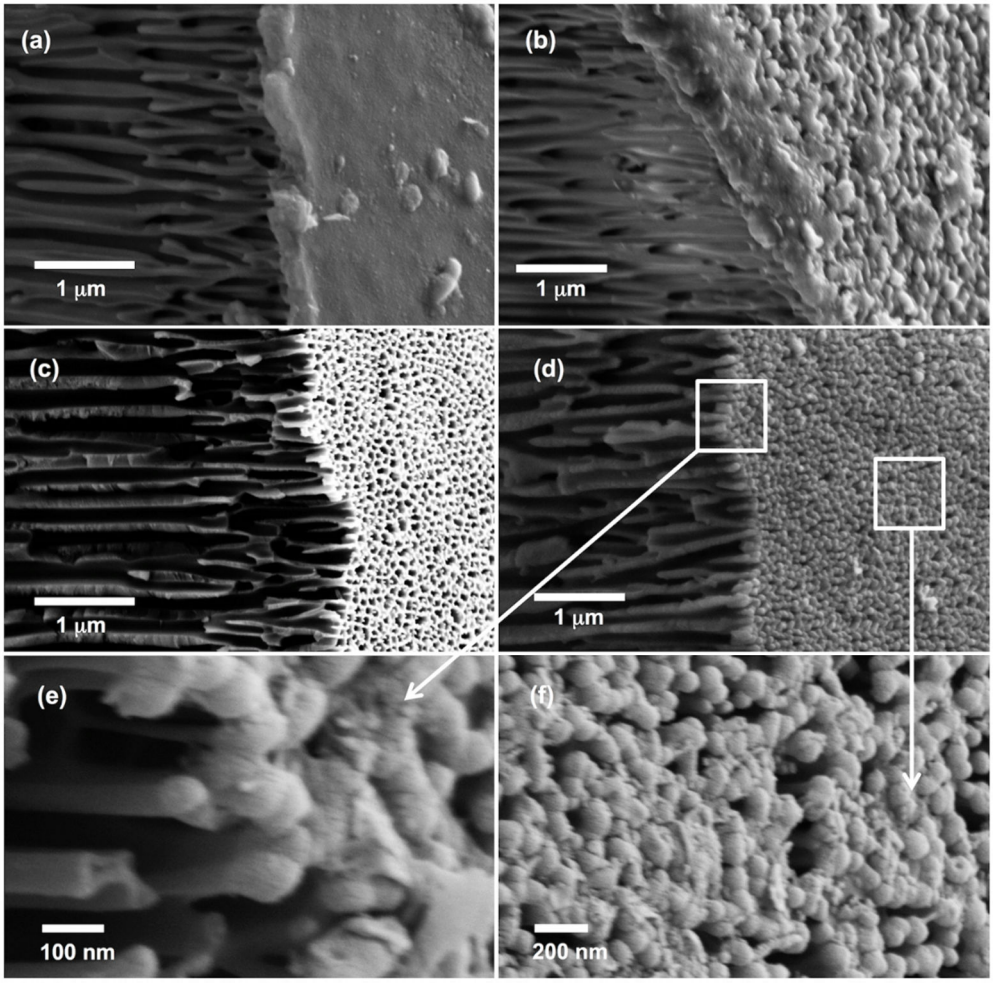

Figure 5.2. SEM images of the cross section of the Janus membranes with p(4VP-co-EGDMA) coatings at different degrees of conformality. Highly non-conformal coatings (a,b) are obtained at Pm/Psat values of 0.33, whereas conformal coatings (c) are obtained at Pm/Psat of 0.16. For key-hole structures (d,e,f) deposition is performed at Pm/Psat value of 0.23

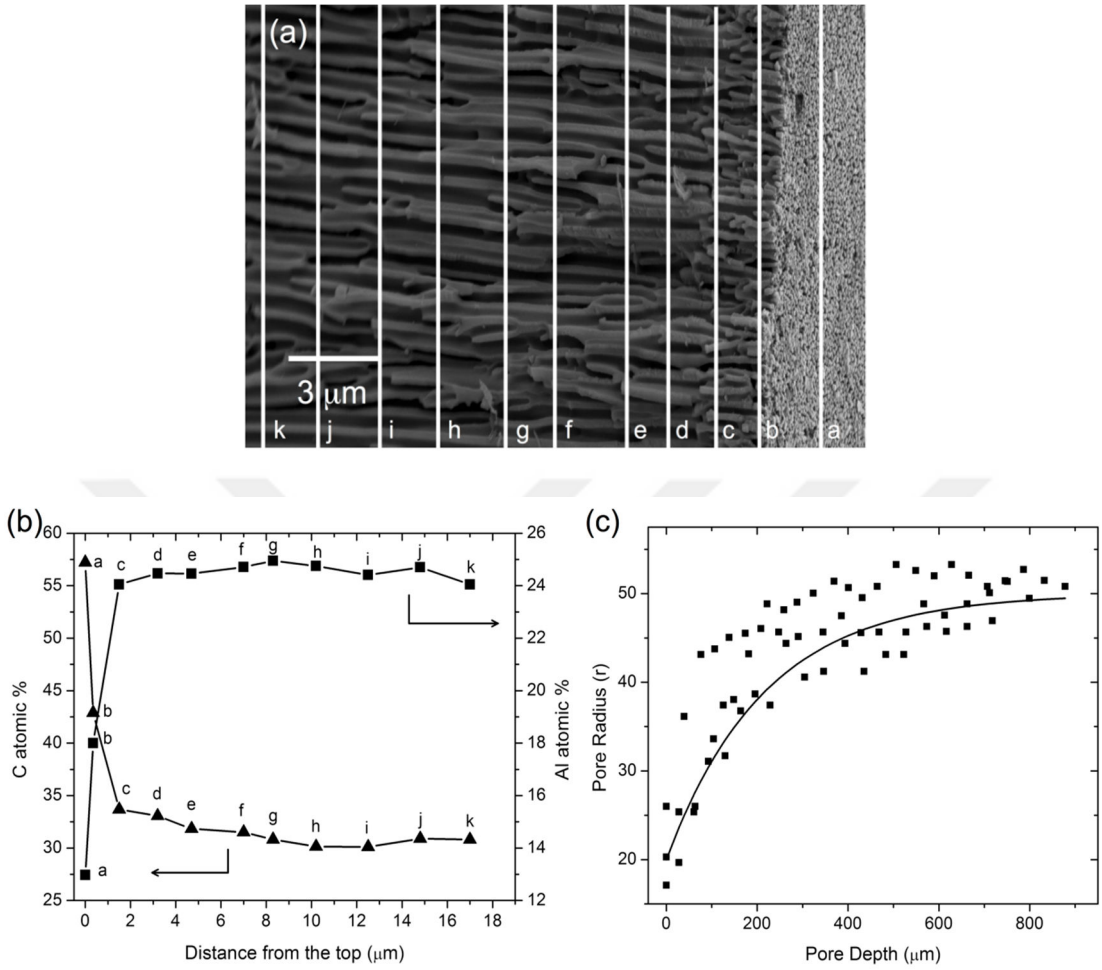

Figure 5.3. (a) SEM image of the cross section of Janus membrane, showing p(4VP-co-EGDMA) coating on side II. (b) Al and C amount within the pores as a function of depth obtained from the EDS analyses, indicating the relative amount of polymer on pore walls. (c) Fit of Equation (3) (straight line) to data (squares) obtained from SEM images

Using Equation 1, the step coverages, S_x, at pore depths of 60, 350 and 660 nm are calculated as 0.83, 0.2 and 0.1, respectively. The depth of the polymer coating, L, and the step coverage, S_L, can be calculated by fitting Equation (2) to the pore profile (Figure 5.2(c)), r_x, and solving for L and S_L. The values of r_x can be obtained from the SEM images down to approximately 800 nm below which the coating thickness cannot be measured visually. The coating depth L and the step coverage S_L are calculated as 1800±20 nm and 0.01±0.003 respectively. This significantly low step coverage confirms that the polymer coating inside the pores is highly non-conformal.

Conformality is achieved when the diffusion of the precursor molecules down the pores dominate polymerization at the pore openings. The dominant mechanism can be determined by using the

Thiele modulus, φ, which is the square root of the ratio of the reaction rate to the rate of diffusion [122] and is defined as [81]:

$$\Phi^2 = \frac{2\nu L^2}{rc_0 D} \tag{5.3}$$

where ν is the deposition rate and c_0 is the monomer concentration at the pore opening. D is the Knudsen diffusivity and in a cylindrical pore, D is given as [123]:

$$\mathrm{D} = \frac{2\mathrm{r}}{3}\left(\frac{8\mathrm{RT}}{\mathrm{M}}\right)^{1/2} \tag{5.4}$$

where R is the gas constant, T is the process temperature and M is the monomer molecular weight. For the depositions presented in this study, D values are calculated as $1.43\text{x}10^{-5}$ m^2/sec and $1.43\text{x}10^{-5}$ m^2/sec, for 4VP and MAA monomers. The deposition rates are $7.3\text{x}10^{-7}$ and $5.1\text{x}10^{-7}$ mol/m^2/sec and the monomer concentrations are $2.3\text{x}10^{-4}$ and $5.6\text{x}10^{-5}$ mol/m^3 for 4VP and MAA, respectively. Using D in Equation (3), Thiele moduli for 4VP and MAA are calculated as 4.8 and 7.5 which indicate faster consumption of the monomers at the pore openings compared to the diffusion rates of the monomers inside the pores, leading to non-conformal depositions.

The ellipsometry studies on p(MAA-co-EGDMA) thin-films coated on Si wafers show that the swelling percentage of the copolymer films is 34% at pH 9, whereas only 2% at pH 3, confirming the pH dependent behavior of the p(MAA-co-EGDMA) polymer. The pH dependent physical changes the p(MAA-co-EGDMA) polymer undergoes are attributed to the electrostatic repulsion among the chains. At pH values higher than the pKa of the p(MAA-co-EGDMA), which is a weak polycarboxylic acid with pKa of 6-7, the ionizable carboxyl groups dissociate into carboxylate ions carrying a negative charge. The electrostatic repulsion among these segments leads to the extension of the chains, thus swelling of the polymer. At lower pH values, on the other hand, the acidic groups will be protonated and will not be ionized. For the unionized system, the hydrophobic interactions will dominate, resulting in the exclusion of water molecules and thus collapse of the polymer chains [100, 101]. On the other hand, the swelling percentage of the p(4VP-co-EGDMA) films on Si wafer was 5% at pH 9 and 50% at pH 3, displaying an opposite pH response to that of the p(MAA-co-EGDMA) polymer. The pKa of the p(4VP-co-EGDMA) is 4.7 and at pH 3, due to protonation of pyridine groups in 4VP chains, they get positive charge.

Therefore, these chains are stretched to minimize charge repulsion while at pH 9 deprotonation of 4VP segments leads to coiled conformation [124].

The gating performance of the Janus membranes was tested by monitoring the diffusion of BSA molecules under different pH conditions. The diffusion tests were performed in a side-by-side diffusion cell with the membrane at the center (Figure 5.4); side I of the membrane (with p(MAA-co-EGDMA) coating) facing the feed side of the cell which contains the BSA solution and side II of the membrane (with p(4VP-co-EGDMA) coating) facing the permeate side which contains 10mM PBS solution. The gating behavior could be controlled by changing the pH of the solution on each side to trigger the volume change of the polymer on the respective side of the membrane.

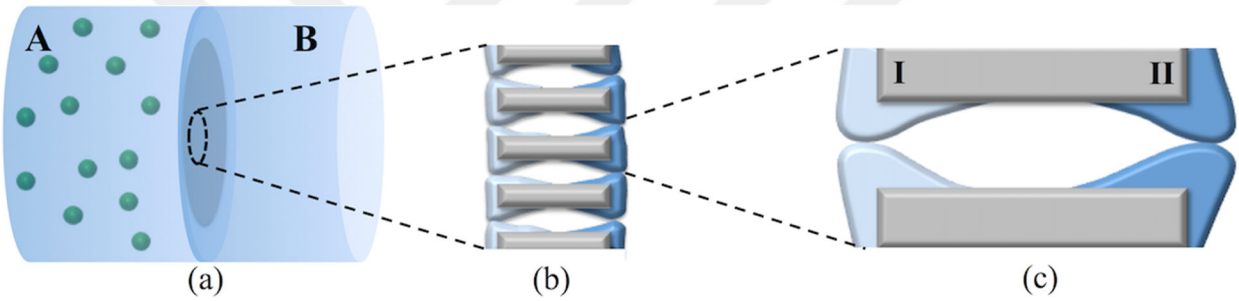

Figure 5.4. Schematic of the Janus membrane composed of AAO template with non-conformal coatings of p(MAA-co-EGDMA) on side I and p(4VP-co-EGDMA) on side II. The membrane is placed in a diffusion cell with BSA in the feed side (A) and PBS in the permeate side (B)

The operation of the Janus membrane is observed by monitoring the BSA concentration on either side of the membrane. Figure 5.5 shows the BSA concentration on the feed and the permeate side as a function of time when the BSA solution at the feed side is at pH 9 and the PBS solution at the permeate side is at pH 9. At pH 9, p(MAA-co-EGDMA) on side I of the membrane is protonated and swollen blocking the pores on the feed side while p(4VP-co-EGDMA) on side II is deprotonated and collapsed, keeping the pores open on the permeate side [125-128]. This allows the BSA molecules to be stored in the feed side, with no significant diffusion to the permeate side. UV-Vis measurements show that the BSA concentration did not change in side I, whereas in side II, no BSA was observed even after 12 hours (Figure 5.5). The results show that the protein molecules were blocked from entering the permeate side, indicating successful blocking of the pores on side I. Before the next step, both sides of the membrane were rinsed with 10mM PBS solution to remove the excess protein molecules.

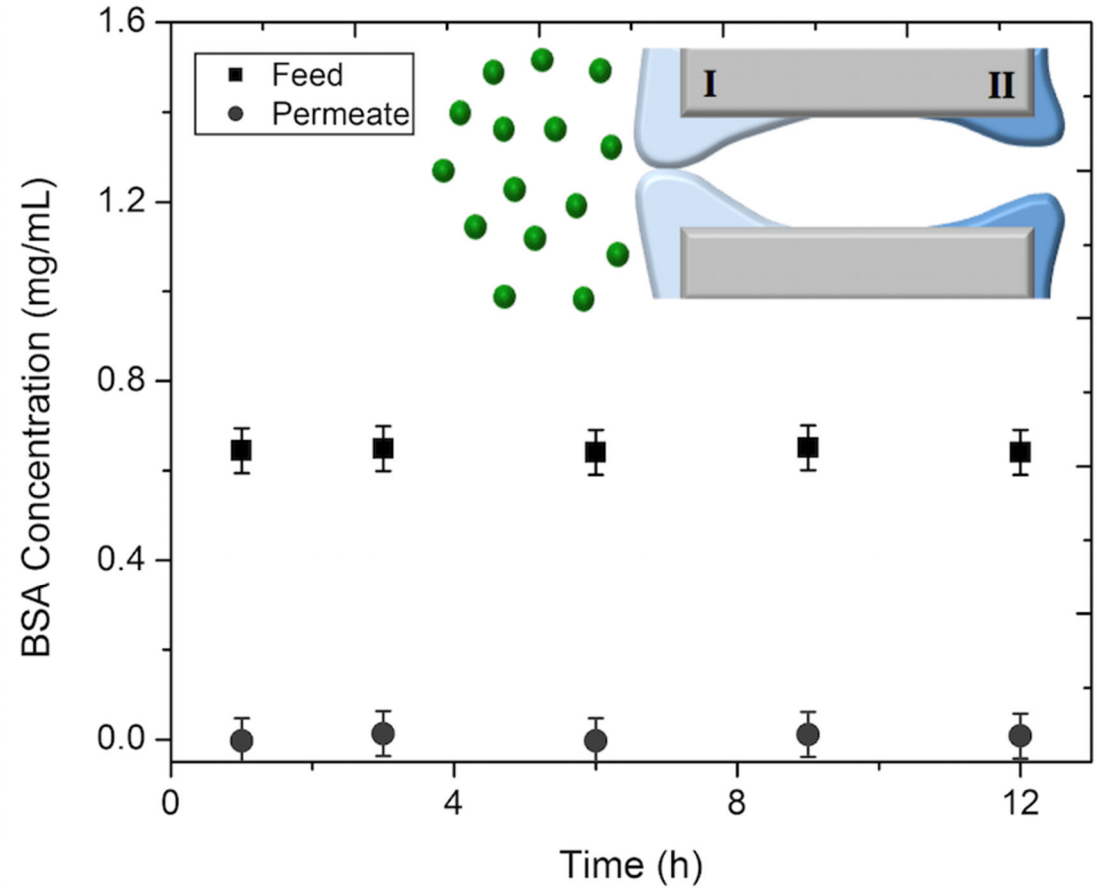

Figure 5.5. Change in the cumulative BSA concentration as a function of time on the feed and the permeate sides when the pH of the feed and permeate sides are 9 and 9, respectively. The swollen polymer on side I blocks the protein molecules from entering the membrane

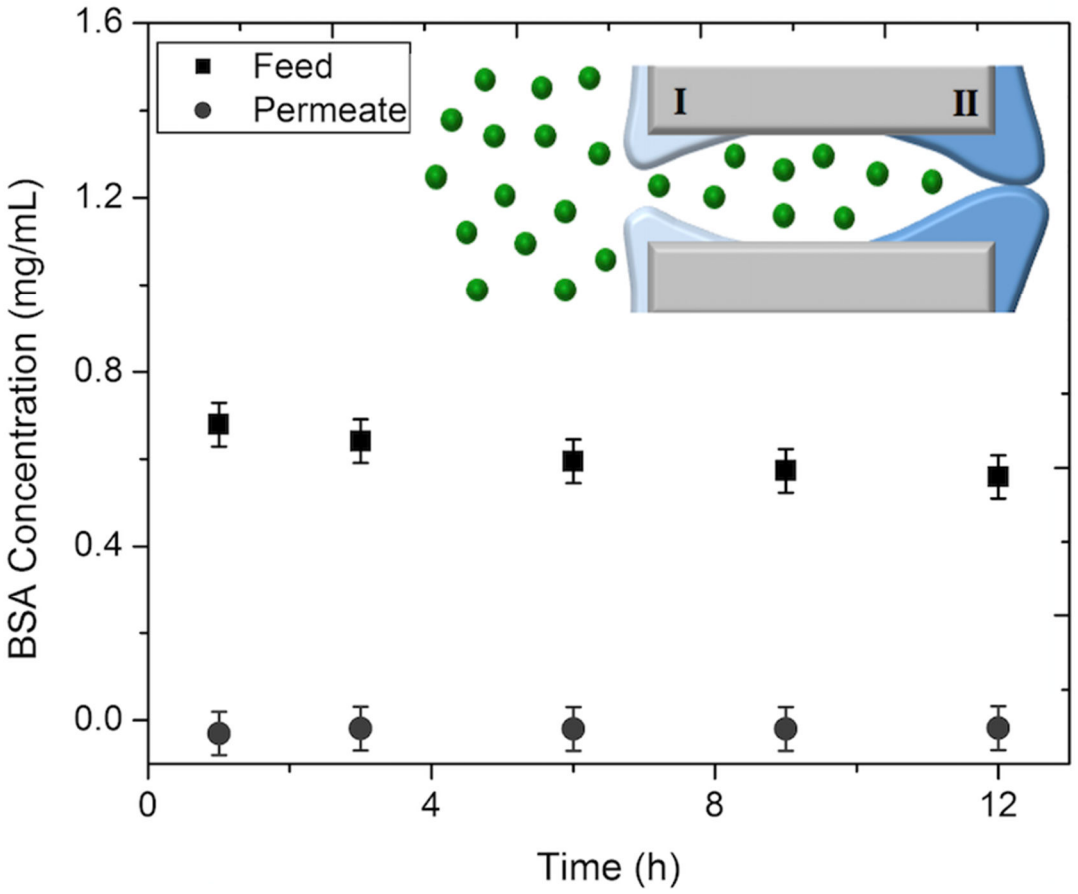

Figure 5.6. Change in the cumulative BSA concentration as a function of time on the feed and the permeate sides when the pH of the feed and permeate sides are 3 and 3, respectively. The protein molecules are hindered from leaving the membrane due to swollen polymer on side II

As the next step, the pH of the solutions on both the feed and the permeate sides of the membrane was changed to pH 3. At pH 3, p(MAA-co-EGDMA) on side I is deprotonated and collapsed, keeping the pores open while p(4VP-co-EGDMA) on side II is protonated and swollen, blocking the pores on the permeate side. Figure 5.6 shows that the BSA concentration on side I gradually decreased in time, from 0.680 mg/mL to 0.550 mg/mL, indicating the diffusion of BSA molecules through the pores into the membrane. On the other hand, the amount of BSA on side II did not change, confirming that there was no release of BSA to permeate side through the pores. The pores on side II remain blocked due to the swollen polymer, p(4VP-co-EGDMA) at pH 3.

In order to test the gating performance of the membrane, the pH of the solution on the feed side was change to pH 9, whereas the pH of the permeate side was maintained at pH 3, ensuring the blocking of the pores at both ends. The BSA concentrations on both sides were monitored for 12 hours. Figure 5.7. shows that at the end of 12 hours, there was no change in the protein concentration on either side, confirming the effective gating of the membrane.

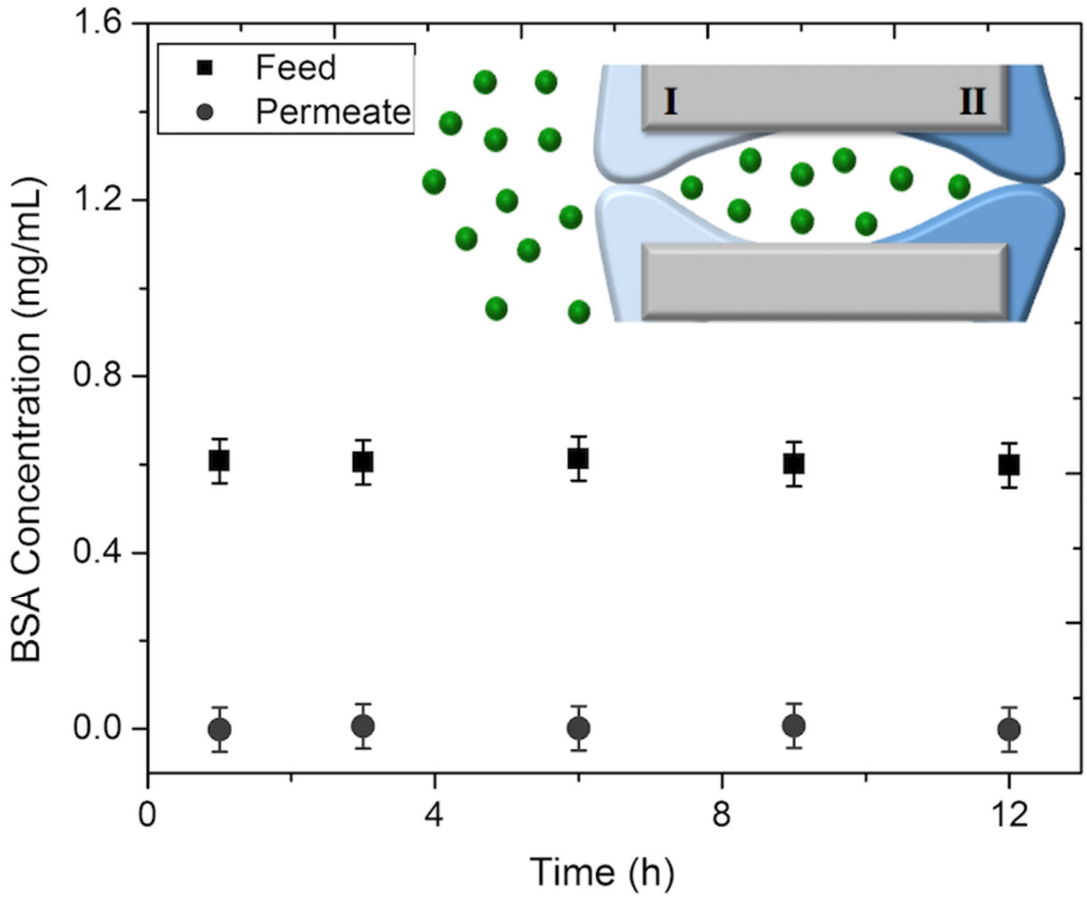

Figure 5.7. Change in the cumulative BSA concentration as a function of time on the feed and the permeate sides when the pH of the feed and permeate sides are 9 and 3, respectively. Swollen polymers on both sides of the membrane close the pore openings, trapping the protein molecules inside

Afterwards, the membrane is put in a diffusion cell with PBS buffer solutions at pH 9 on both sides. At pH 9, side I of the membrane is blocked due to swollen polymer, whereas polymer on side II is collapsed at this pH, resulting in open pores. The UV-Vis measurements show that the BSA concentration on the permeate side of the cell gradually increases whereas the BSA concentration on the feed side does not change in 12 hours (Figure 5.8). The results show that the

protein molecules were released upon trigger only to the permeate side. Therefore, by changing the pH, the release of the proteins from the membrane could be controlled both spatially and temporally. The final protein concentration after 12 hours was 0.04 mg/mL while the amount of protein trapped inside the pores before release experiment was 0.13 mg/mL (as observed in Figure 5.6) i.e. around 30% of proteins trapped inside the membrane pores are released in 12 hours. Once the polymer is collapsed and the pores are open, the protein molecules inside the pores diffuse out due to the concentration gradient between the permeate side and the pore cavities. However, concentration gradient being the sole driving force for diffusion is not sufficient to remove all the protein molecules. Furthermore, the protein molecules may be entrapped in the polymer mesh.

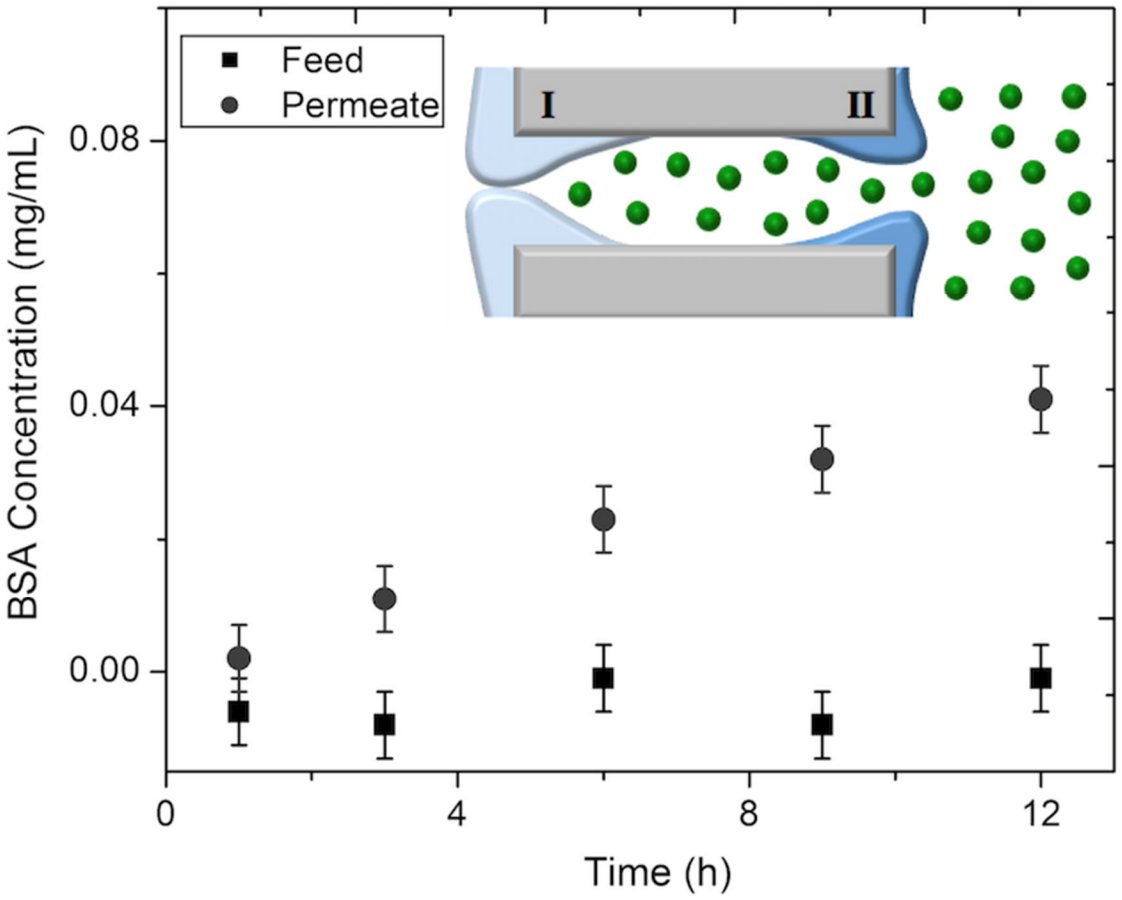

Figure 5.8. Change in the cumulative BSA concentration as a function of time on the feed and the permeate sides when the pH of the feed and permeate sides are 9 and 9, respectively. Upon pH change on the permeate side to 9, p(4VP-co-EGDMA) on side II collapses, unblocking the protein molecules which then diffuse to the permeate side

The gating performance of the membranes was tested also with rose Bengal dye molecules (IUPAC name 4,5,6,7-tetrachloro-3′,6′-dihydroxy-2′,4′,5′,7′ tetraiodospiro (isobenzofuran-1(3H),9′-(9H) xanthen)-3-one), which are smaller in size than the BSA molecules. Rose Bengal is a halogen containing dye which gives out pink color when dissolved in water even at low concentrations. Therefore, rose Bengal is used in this study to visually demonstrate the effectiveness of the membranes in gating small molecules. Experiments are performed first at pH9 on both sides (Figure 5.9 (a)), which results in closed pores on side I and open pores on side II. Figure 5.9 (b) shows that color change was not observed for the first 18 hours, however after 18 hours, color started changing in the permeate side indicating the leakage of the dye molecules through the pores. The color change with rose Bengal dye is observed when the concentration levels in the permeate side reach approximately 0.04 g/L.

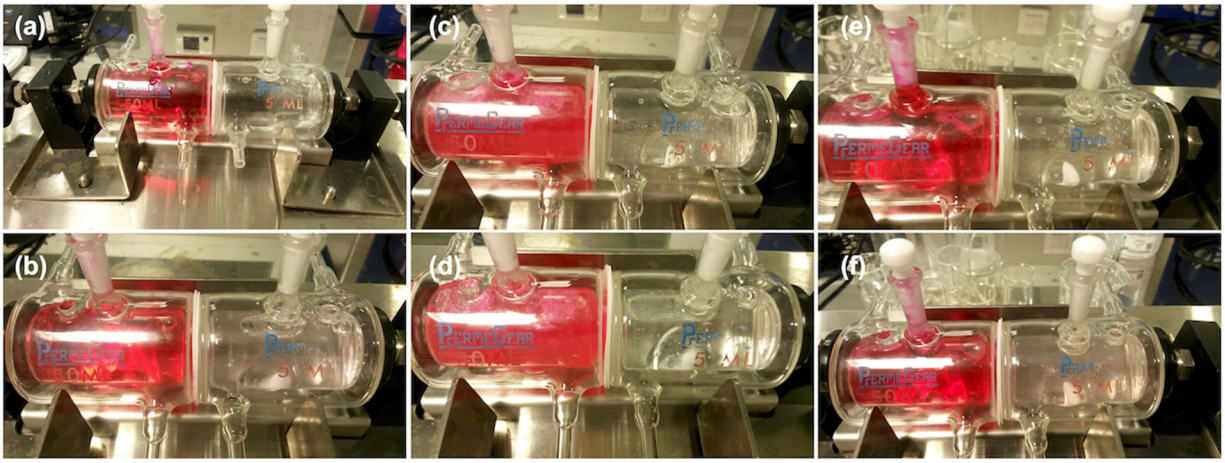

Figure 5.9. Pictures of the diffusion experiments performed with the rose bengal dye in side-by-side diffusion cell set-up. (a,b) Experiments performed at pH 9/pH 9 on both feed and permeate sides show there is leakage after 18 hours (b). (c,d) Experiments performed at pH 3/pH3 show that the membrane could successfully block the molecules for 24 hours (d). (e,f) Experiments performed at pH 9/pH 3 where both ends were open show that the concentration of molecules on the permeate side reached 0.04 g/L. (a,c,e) Pictures of the diffusion cells at the beginning of the experiments

On the other hand, in the similar experiments performed at pH3 (Figure 5.9 (c)), where pores on side II are closed, there was no color change at the end of 24 hours (Figure 5.9 (d)), confirming that the membrane could successfully block the dye molecules from diffusing to permeate side. The successful gating performance of side II compared to that of side I, can be attributed to the higher swelling percentages of p(4VP-co-EGDMA) on side II. The lower swelling percentages of

p(MAA-co-EGDMA) would result in pores not completely closing upon swelling, preventing complete blocking of the small dye molecules. Since the size of the BSA molecules are significantly larger than the dye molecules, leaking of the BSA molecules is not observed under similar experimental conditions. Further experiments are performed at pH9/pH3 where both gates are open (Figure 5.9 (e)) and color change is observed after 9 hours (Figure 5.9(f)).

CHAPTER 6. SYMMETRIC-ASYMMETRIC MEMBRANES

6.1. Introduction

The aim of this chapter is development of gates to diffuse only specific protein in the mixture of two proteins according to their size and effect of nanochannels shapes on the diffusion rate of through the nanochannels. Change in the pores size of the membrane by pH changing especially with the pores size as small as the proteins size triggers selective separation of proteins. Moreover, the shape of nanochannels affects the diffusion rate, and protein separations. Diffusion experiments on LYZ and Hb shows, in addition to protein and channel size, the nanochannels shape and deposited polymer double layer distribution affects the diffusion rates. Diffusion of Hb is controlled and blocked using pH responsive polymers as the negates and only selective sedation of LYZ in Hb and LYZ in protein mixture is achieved.

6.2. Experimental Methods

6.2.1. pH-responsive Membrane Preparation

Membranes were fabricated by conformally coating the pores of the track etched AAO membranes with pH-responsive polymers via the iCVD technique in a vapor phase. The monomer methyl methylacrylic acid (MAA), the crosslinker ethylene glycol dimethyl acrylate (EGDMA), and the initiator tertbutyl peroxide (TBPO) were used without any purification. The flowrates of MAA and EGDMA and TBPO were 1.73sccm, 0.16sccm, and 1sccm respectively. N_2 was introduced into the vacuum chamber at flowrate 1sccm to adjust P_m/P_{sat} for slow deposition and the chamber pressure was kept 100mTorr during depositions. The filament and substrate temperatures were adjusted to 240^{o}C and 25^{o}C, respectively to deposit 30nm p(MAA-co-EGDMA) on Si wafer and in situ film thickness was controlled by reflection of a He/Ne laser beam (633nm) from the thin film.

6.2.2. Membrane Characterization

Fourier transform infrared (Thermo-Nicolet iS10 FTIR) spectroscopy in normal transmission mode was used for the analysis of the polymer chemical composition inside the AAO template pores. FTIR spectra were acquired over the range of 400-4000 cm^{-1} with a 4 cm^{-1} resolution for 64 scans. Field Emission Scanning Electron Microscope (Zeiss, SUPRA VP 35) at 4 kV accelerating voltage was used to capture images of membrane pores from the top and the cross-section planes. The polymer thin film thickness changes with pH on Si wafer was measured using a spectroscopic ellipsometer (M2000 Spectroscopic Ellipsometer J.A. Wollam Co. Inc.) with a heated liquid cell in the incidence angle of 75 degrees. In-situ film thickness variations at pH3 and pH6.8 were monitored for 60 minutes at room temperature following the Cauchy model to measure the film thickness at wavelengths ranging from 315 to 718nm.

6.2.3. Permeation Experiments

Diffusion studies of HB and LYZ through the symmetric and asymmetric membranes were performed at 4 ^{o}C in a side-by-side diffusion cell with an effective membrane area of 0.785 cm^2 and a chamber volume of 5mL. The solvent was 10mM PBS, and pH of solvent was adjusted using NaOH and HCl. 1mg/mL LYZ and Hb solutions in PBS buffer solvent at pH3, and pH6.8 and 1mg/mL LYZ+Hb solution in PBS buffer solvent at pH6.8 were prepared. In each diffusion tests, 1mg/mL of protein solution was filled in feed side while the permeate side was filled with 10mM PBS buffer solution at the same pH and the solutions in both cells were stirred continuously by magnets throughout the experiments. The protein concentration in the feed and permeate sides was measured using a NanoDrop 2000/2000c spectrophotometer (Thermo Fishe Scientific) at specific time intervals.

6.3. Results and Discussion

Figure 6.1 shows FTIR spectra of p(MAA-co-EGDMA) on Si wafer. FTIR spectra confirms the successful copolymerization of MAA and EGDMA. The spectra contain a peak at 1380 cm^{-1} attributed to the methyl bending vibration, 1430 cm^{-1} corresponds to CH_3 deformation mode, and the peak at 2850-3000 cm^{-1} attributed to C-H stretching vibration of p(MAA-co-EGDMA). The peaks at 1700 cm^{-1} and 1730 cm^{-1} correspond to the C=O stretching vibrations of MAA and

EGDMA, respectively [68, 129]. The crosslinker to polymer ratio was calculated using C=O peak area and it was around 49.5%.

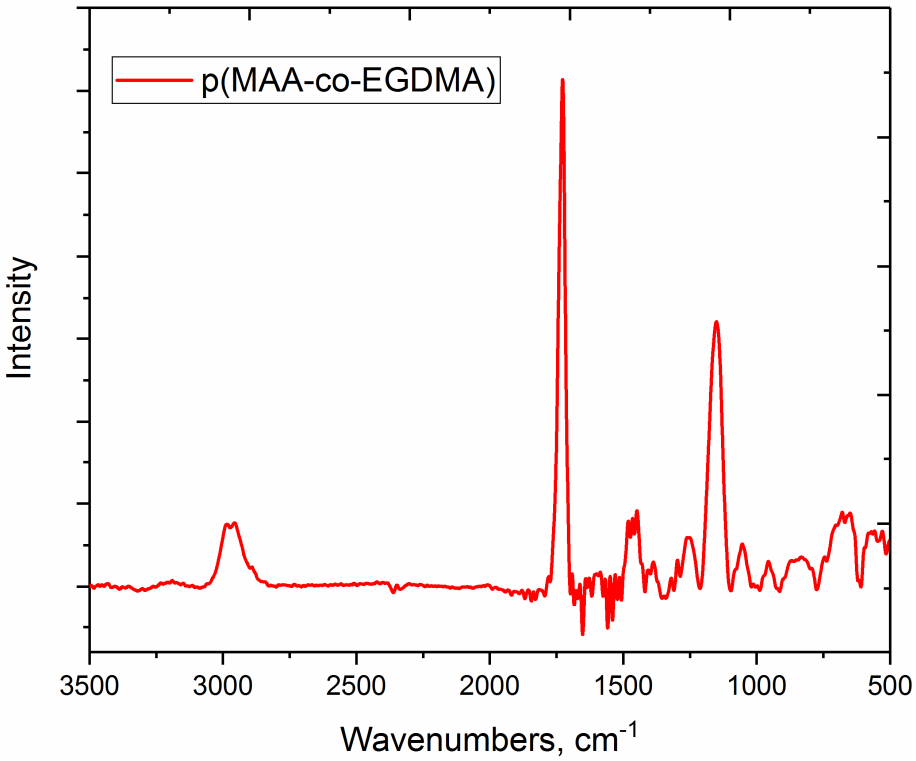

Figure 6.1. FTIR spectra of the p(MAA-co-EGDMA) coating on Si wafer

Figure 6.2 shows the SEM images of the symmetric and asymmetric AAO templates deposited conformally with p(MAA-co-EGDMA) as hybrid membranes. To get conformal depositions the P_m/P_{sat} should be low, here P_m indicates that the monomer partial pressure depends on monomer flowrates and P_{sat} shows the monomer saturated vapor pressure related to substrate temperature. Low P_m/P_{sat} value means the number of monomers adsorbed on the surface is low, resulting in low deposition rate and conformal coatings [79, 130].

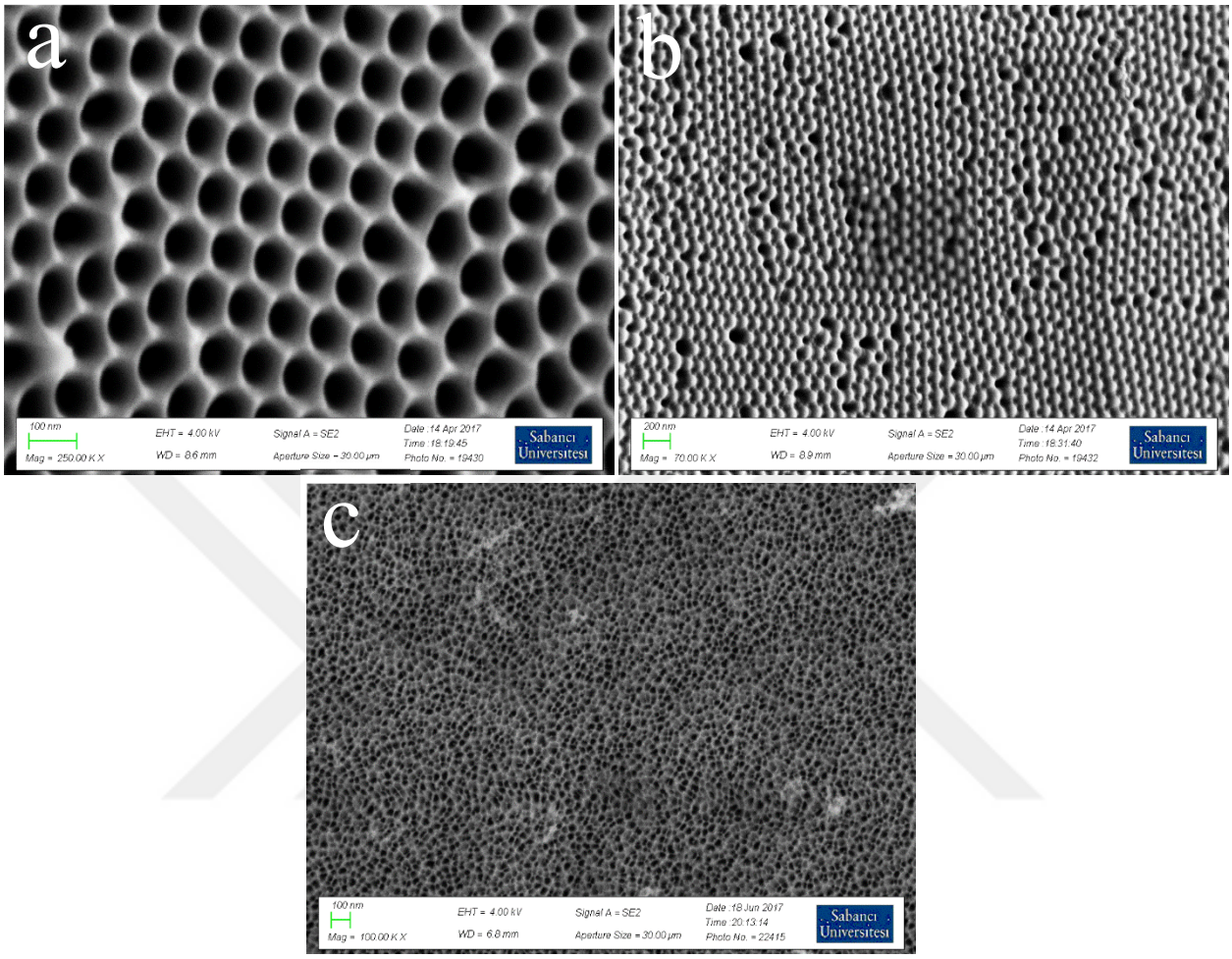

Fig 6.2. SEM images of hybrid membranes a) bottom view of asymmetric AAO template b) top view of asymmetric AAO template c) symmetric AAO template deposited with p(MAA-co-EGDMA) conformally

Swelling studies of p(MAA-co-EGDMA) this films contains 49.5% crosslinker on Si wafer via ellipsometry in dynamic states shows that the thin film is a pH depended polymer and at pH3 it swells 2% while at pH6.8 this value is 20% because of the electrostatic repulsion among the polymer chains. At higher pH values the ionizable carboxyl groups dissociate into carboxylate ions carrying a negative charge. The electrostatic repulsion among these segments leads to the extension of the chains, thus causing the swelling of the polymer. At lower pH values, on the other hand, the acidic groups will be protonated and not be ionized. For the unionized system, the hydrophobic interactions would dominate, resulting in the exclusion of water molecules and thus collapse of the polymer chains [100, 101].

Figure 6.3 shows diffusion of LYZ through the symmetric and asymmetric membranes at pH3. Diffusion of LYZ in the asymmetric membrane is significantly higher than diffusion of LYZ in the symmetric one.

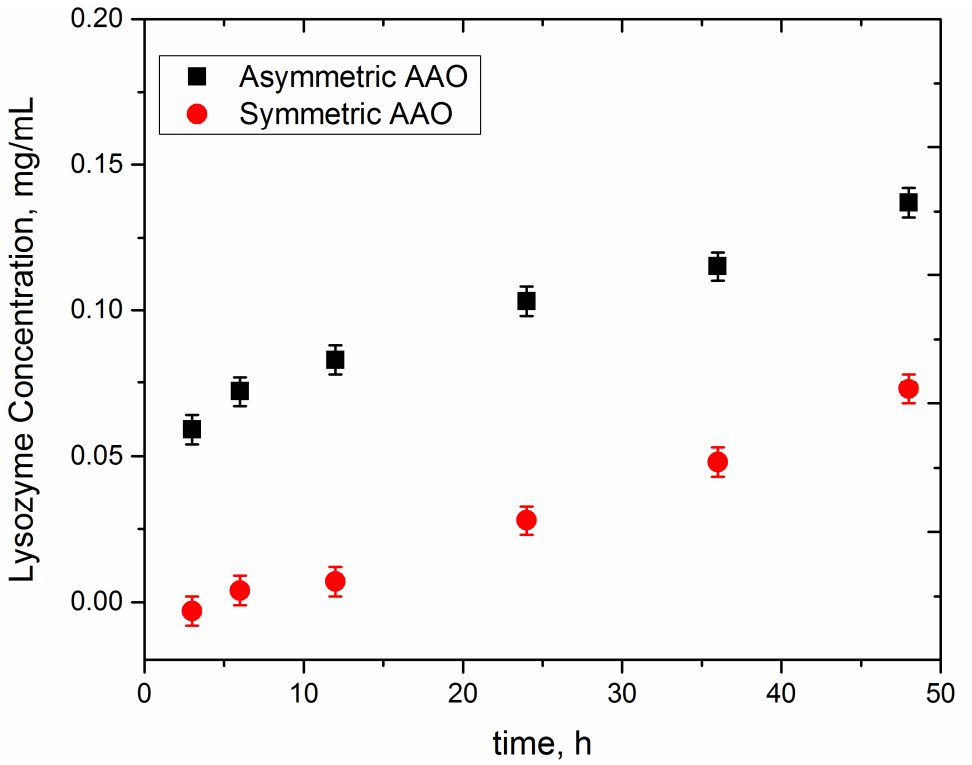

Figure 6.3. LYZ diffusion through the symmetric and asymmetric membrane at pH3

Ion diffusion through nanochannels can induce electrical potential across the membrane which is related to the ion concentration on both sides of the membrane [131]. Moreover, inside the nanochannel ion behavior depends on both ion concentration and electric osmosis as [131]

$$\Psi = -cz\mu\frac{\partial V_x}{\partial x} - \frac{\mu kT}{q}\frac{\partial c}{\partial x} \qquad (6.1)$$

Here, Ψ is ion flux, c is the ion concentration, z is the ion valances, μ is the mobility of ions, V_x is the electrical potential at a distance x from the entrance of nanochannel, q is the charge of each ion, T is the absolute temparature, and k is Boltzmann constant. Electrical osmosis flux resulting from electrical double layer [132, 133], triggers an electrical potential between nanochannel walls and buffer solvent contains ions [134] and this potential, φ, is

$$\Phi = \Phi_w \exp\left({}^{-y}/_{\lambda_D}\right) \quad (6.2)$$

Where, φ_m , is the potential at the walls of the channels, λ_D is Debye length, and y is the distance from the wall. This potential can affect and reduce diffusion of ions along the nanochannels and we can assume an equivalent circuit including capacitors because of the double layer, and resistors because of the Debye-Huckel potential, which both affect the ions travelling inside the bulk solvent [131]. In the symmetric membrane two different points along axial direction of nanochannel have the same,y, so the Debye-Huckel potential and resistance inside the bulk solvent is constant for these two points (Figure 6.4a), while in the asymmetric membrane, two points in axial direction of nanochannels had different y, thus different Debye-Huckel potental, and bulk resistance and amount of potential and resistance decreases from entrance part of the membrane by increasing its diameter (Figure 6.4b), so diffusion of LYZ in the asymmetric membrane is more than the symmetric one.

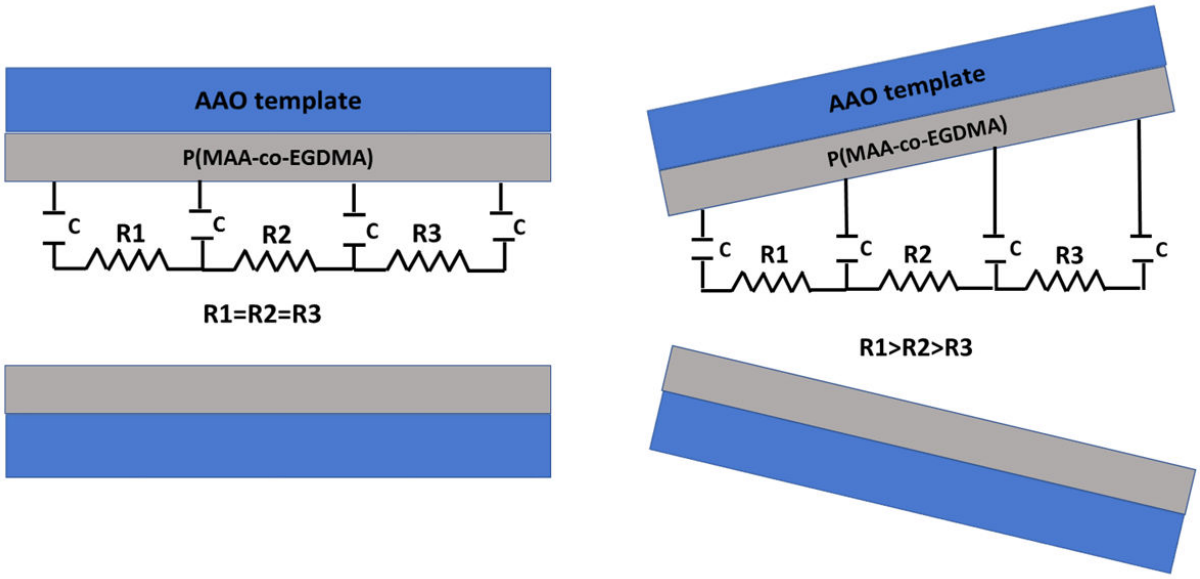

Figure 6.4. Equivalent circuit for a) the symmetric b) the asymmetric membranes

Diffusion of Hb across the symmetric and asymmetric membranes at pH3 is shown in Figure 6.5. There is no difference in diffusion rate of Hb for the symmetric and asymmetric membranes and Hb diffusion rate is less than LYZ diffusion rate.

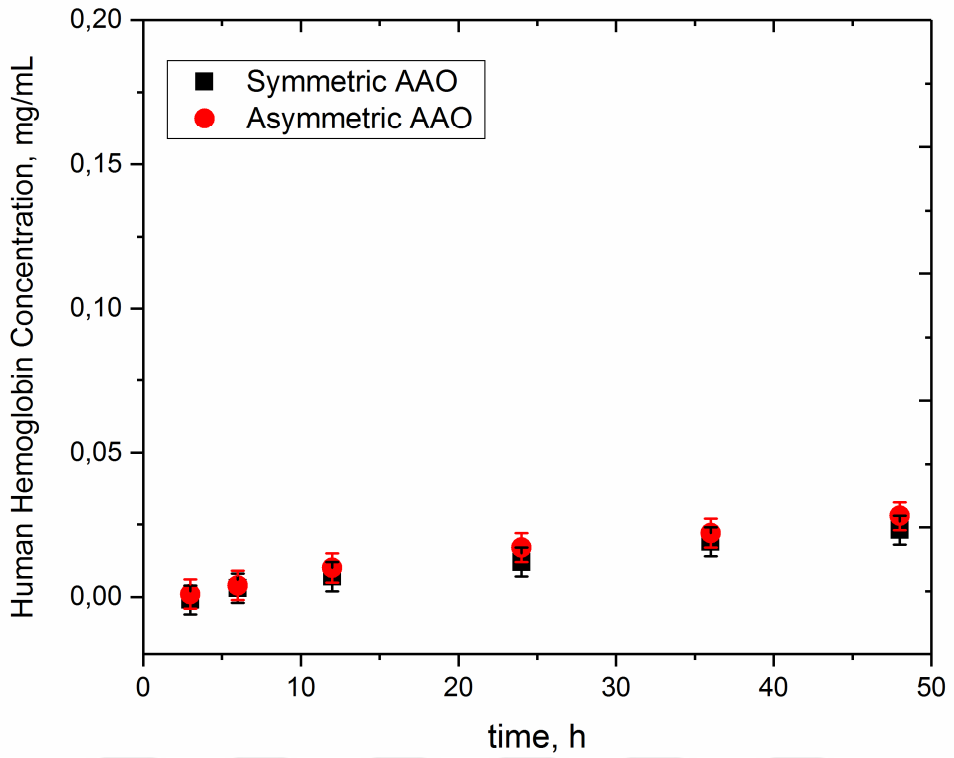

Figure 6.5. Hb diffusion through the symmetric and asymmetric membrane at pH3

Molecular weight and diameter of Hb are around 65kDa and ~6.8nm, respectively [135] and for LYZ these values are 14kDa and ~1.8nm [136], therefore, the diffusion rate for LYZ in both membranes is more than Hb. Moreover, in passive diffusion of proteins through the membrane without any chemical or physical stresses pore size of the membrane is important [137]. When pore size of the membrane is in the range, two or more diffusing molecular cannot pass through the membrane pores at the same time; hence the single-file diffusion (SFD) condition is satisfied by the membrane [138-140]. In this situation, only one protein can enter in the pore so, the pore shape and Debye-Huckel potential distribution do not affect the protein travel along the nanochannels.

Figure 6.6 shows diffusion of LYZ proteins through the symmetric and asymmetric membrane at pH6.8. p(MAA-co-EGDMA) is a pH responsible polymer and at higher pH it swells and decreases the membrane pore sizes because of ionization of carboxyl groups into negatively charged carboxylate groups and polymer chains extension [100, 101].

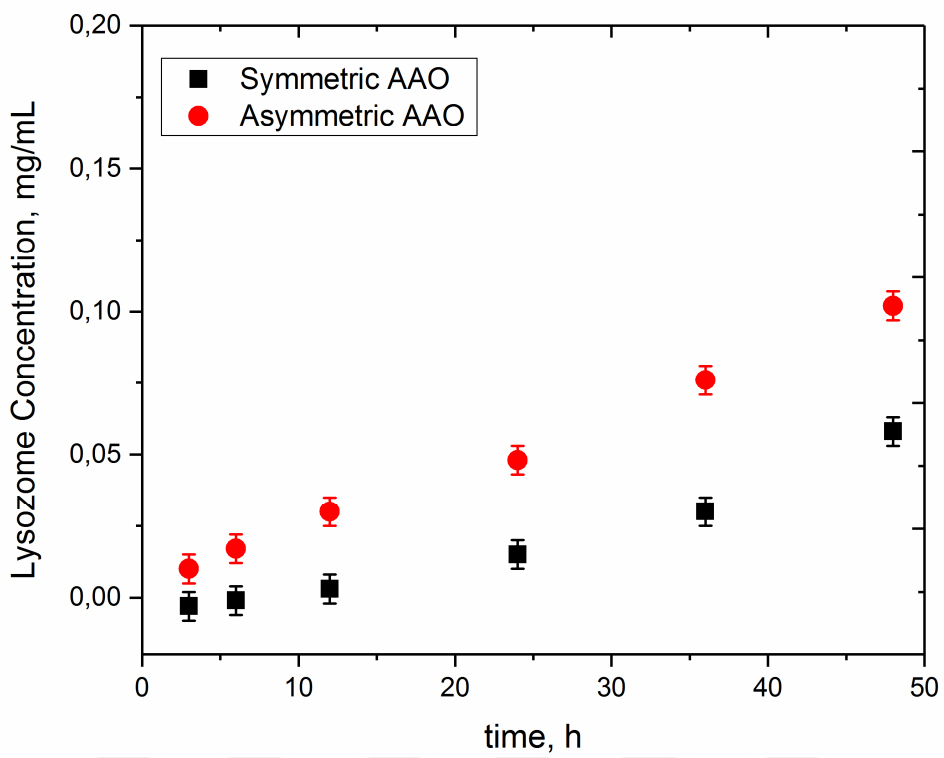

Figure 6.6. LYZ diffusion through the symmetric and asymmetric membrane at pH6.8

In comparison to pH3, LYZ diffusion through the membranes has the same behavior except that its diffusion rate is less because of decreasing membrane pore size at pH6.8. At this pH value, the membrane pores are large enough for LYZ small proteins (diameter in 1.8nm [136]) not to obey single-file diffusion (SFD) mode like Hb diffusion at pH3. Moreover, the less electric osmosis along the nanochannels in the asymmetric membrane because of nanochannels shapes triggers higher passive diffusion rate in this membrane in comparison to the symmetric one.

Diffusion of Hb through the symmetric and asymmetric membrane at pH6.8. is shown at Figure 6.7. At pH 6.8 there is no diffusion of Hb in the both symmetric and asymmetric membranes.

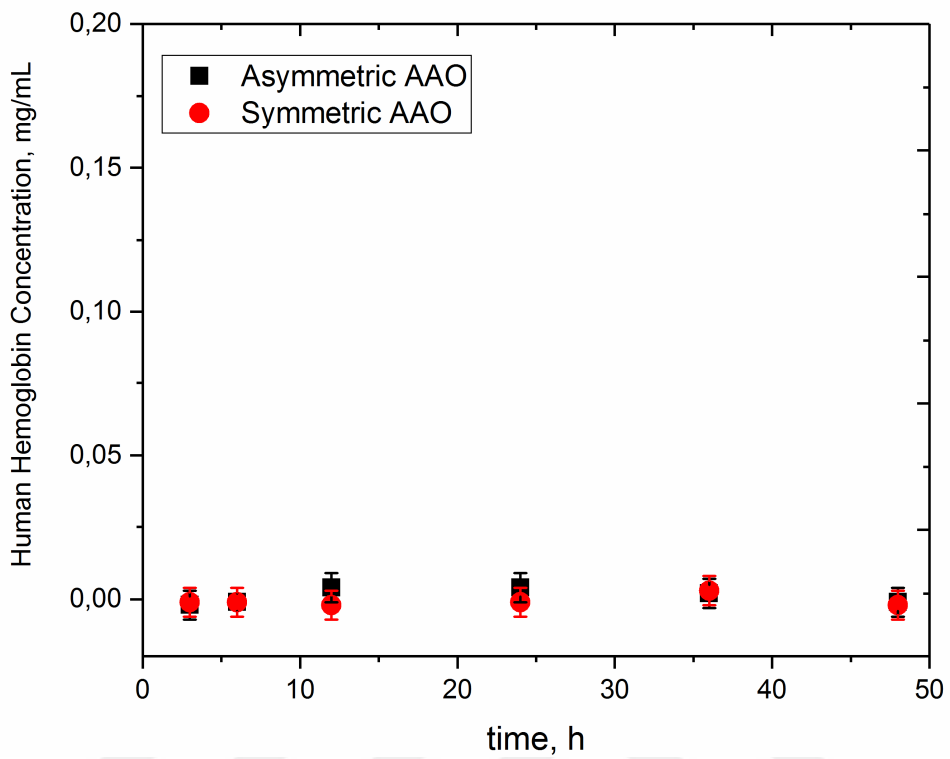

Figure 6.7. Hb diffusion through the symmetric and asymmetric membrane at pH6.8

It seems that swelling of the pH responsive protein polymer at pH6.8 can decrease the pore size of membrane less than Hb diameter (6.8nm [135]) to allow Hb molecules to pass through the membrane as compared to LYZ diffusion at pH6.8 since LYZ diameter is around 4 times smaller than Hb diameter.

Figure 6.8 shows diffusion rate of mixed Hb and LYZ at pH6.8. Isoelectric points for Hb and LYZ are 6.8 and 11, respectively [141, 142]. Therefore at pH6.8, Hb is neutral elecrically but LYZ is positvely charged. At pH6.8 there is no Hb diffusion, so all proteins passing through the membrane are LYZ. In comparison to diffusion of pure LYZ at pH6.8, the diffusion rate of LYZ in the mixture with Hb is less because of the hinderance effect of Hb especially during the first hours of diffusion tests.

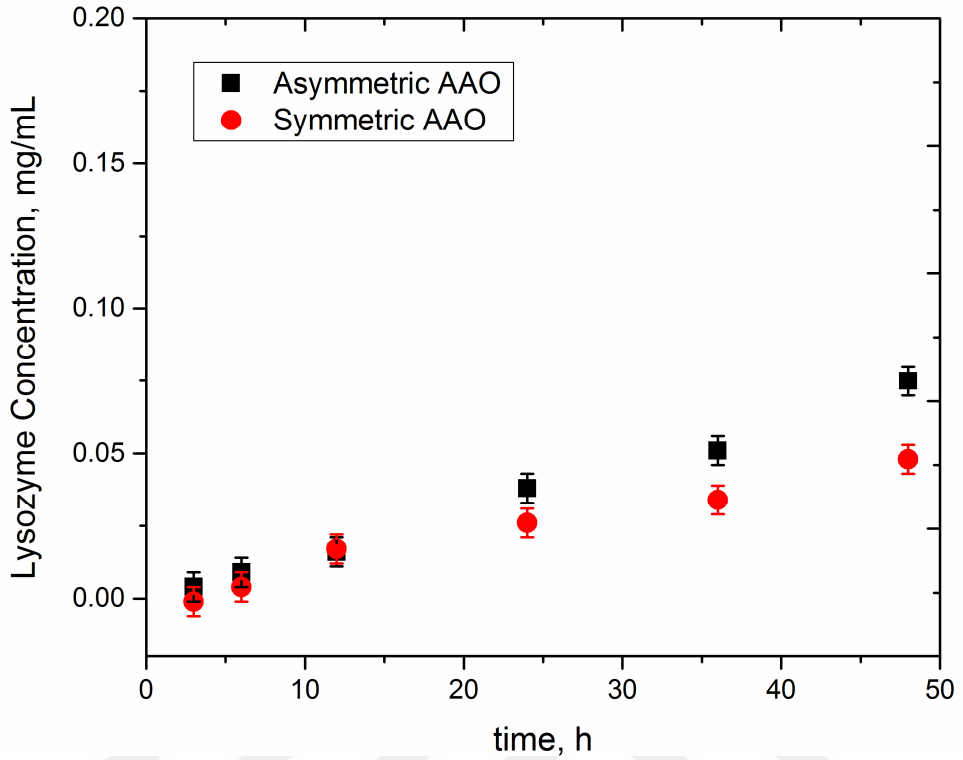

Figure 6.8. LYZ diffusion through the symmetric and asymmetric membrane at pH6.8 in mixed LYZ and Hb

CHAPTER 7. HYBRID AUNPS ATTACHED MEMBRANES

7.1. Introduction

The aim of this chapter is charged-based separation of proteins. Two proteins with the same molecular weight and size, Hb and HAS, are separated according to the membrane and proteins charge as a function of pH. Negatively charged gold NPs are attached on the top and inside the pore of the membrane to get negatively charge membrane. Diffusion behavior of Hb and HSA when they have the same or opposite charge in compare to the negatively charged membrane is investigated. Moreover, selectivity of the negatively charged and neutral membranes for mixture of Hb and HSA when one of the proteins is in its isoelectric point to separate two similar sized proteins is compared.

7.2. Experimental Methods

7.2.1. Membrane Depositions

The track etched AAO membranes (with 100 nm pores) were deposited using the iCVD technique with p(NIPAAm-co-EGDMA), conformally. The monomer N-isopropylacrylamide (NIPAAm), the crosslinker ethylene glycol dimethyl acrylate (EGDMA), and the initiator tertbutyl peroxide (TBPO) and N_2 gas were used without further purification. NIPAAm and EGDMA were vaporized in the jars at 75°C and 90°C, respectively and TBPO was at room temperature. Nitrogen and all vapors were introduced into the iCVD chamber for deposition. NIPAAm flowrate was 1sccm ,EGDMA 0.08sccm, TBPO and N_2 flowrates were fixed at 1sccm. The filament temperature was kept at 240°C. The deposition pressure was set to 200mTorr and substrate temperature was adjusted to 40°C to get P_m/P_{sat} equal to 0.28 and 0.11 for NIPAAM and EGDMA respectively, to conformal deposition inside the pores. The thickness of the samples was controlled by using a laser interferometry to reach 200 nm on the Si wafer.

7.2.2. Negatively Charged AuNPs

20 mL of 1.0 mM gold chloride trihydrate ($HAuCl_4 \cdot 3H_2O$ Sigma Aldrich, Germany) and 2 mL of 1 wt% trisodium citrate dihydrate ($C_6H_5Na_3O_7 \cdot 2H_2O$, Merck, Germany) solutions were prepared in milli-Q water. Gold chloride solution was heated to the boiling temperature under vigorous stirring. Subsequently, trisodium citrate solution was added to the boiling gold chloride solution. As the mixture achieved deep red color, heat and stirring was stopped and the mixture was cooled to RT. The hydrodynamic size distribution and zeta potential of gold nanoparticles, Malvern Zetasizer Nano ZS (Malvern Instruments, Worcestershire, UK) equipped with a polarized He-Ne laser aligned at 173° angle was utilized. The samples were only diluted hundred-fold with milli-Q water without any filtering. Quartz cuvettes were used for dynamic light scattering measurements. Folded capillary cells were used for zeta potential measurements. The acquired data was processed using Zetasizer Software 7.12 by NNLS algorithm for triplicate size measurements of 15 individual scans and triplicate zeta potential measurements of 100 individual scans.

7.2.3. Charging of Membranes

Membranes were immersed inside the solution of negatively charged gold nanoparticles for 48 hours and each 6 hour were rinsed with distilled water to remove unattached nanoparticles then kept inside distilled water for diffusion experiments.

7.2.4. Membrane Characterization

Fourier transform infrared (FTIR) was performed in normal transmission mode to acquire spectra over the range of 400 to 4000 cm^{-1} with a 4 cm^{-1} resolution for 64 scans to analyze the chemical composition of the polymer inside the AAO templates by a Thermo-Nicolet iS10 FTIR spectroscopy. The negatively charged gold nanoparticles attached to the surface and the pores of the membrane were imaged using a Field Emission Scanning Electron Microscope (Zeiss, SUPRA VP 35) at 4 kV accelerating voltage and EDS analysis was done to determine the AuNP at 10kV accelerating voltage and 8.5mm working distance.

7.2.5. Diffusion Experiments

Diffusion tests were done in a side-by-side cell by putting the membrane between two cells, one side was filled with the protein solution and other side was filled with 10mM PBS solution and

solutions were stirred at 4°C with an effective membrane area of 0.785 cm^2. Proteins used were HSA, Hb, and mixture of HSA and Hb with the concentration 1g/L in 10mM PBS buffer. The pH of the solution was adjusted to 3, and 9 for HSA and 3, and 9 for Hb and 4.7 and 6.8 for Hb and HSA mixture using NaOH and HCl. At certain times, the solution of the permeate side was taken and the protein concentration was measured using a NanoDrop 2000/2000c spectrophotometer (Thermo Fishe Scientific).

7.3. Results and Discussion

Figure 7.1 shows the Zeta potential and size distribution of synthesized gold nanoparticles. The average size of gold nanoparticles is 13.6nm and the potential of these naroparticles is -29.5mV.

Figure 7.2 shows FTIR spectra of p(NIPAAm-co-EGDMA) of AAO template. FTIR spectra confirm the successful copolymerization of NIPAAm and EGDMA because the peak showing the vinyl bond at 1620 cm^{-1} is absent. The spectra contain a peak at 3330 cm^{-1} attributed to the NIPAAm secondary amine N-H stretching groups, the peak at 300-2820 cm^{-1} is responsible for isopropyl C-H stretching, the peak at 1530 cm^{-1} corresponds to C-N-H bending (amide II band), and the peak at 1654-1645 cm^{-1} is attributed to C=O stretching (amide II band). The peaks corresponding to C=O stretching of the methacrylate group in EGDMA occurs at 1730 cm^{-1} [143-146].

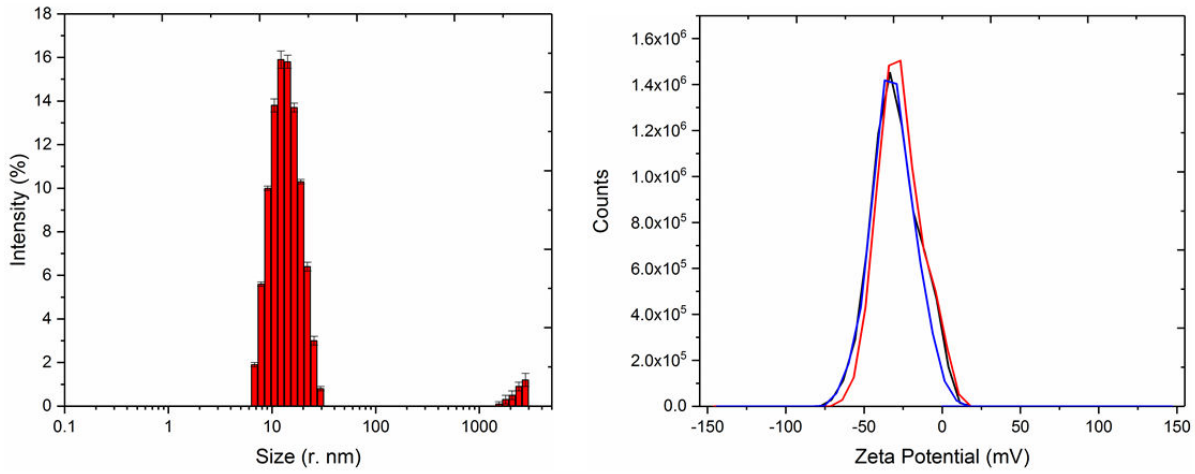

Figure 7.1. Size distribution and zeta potential of AuNPs.

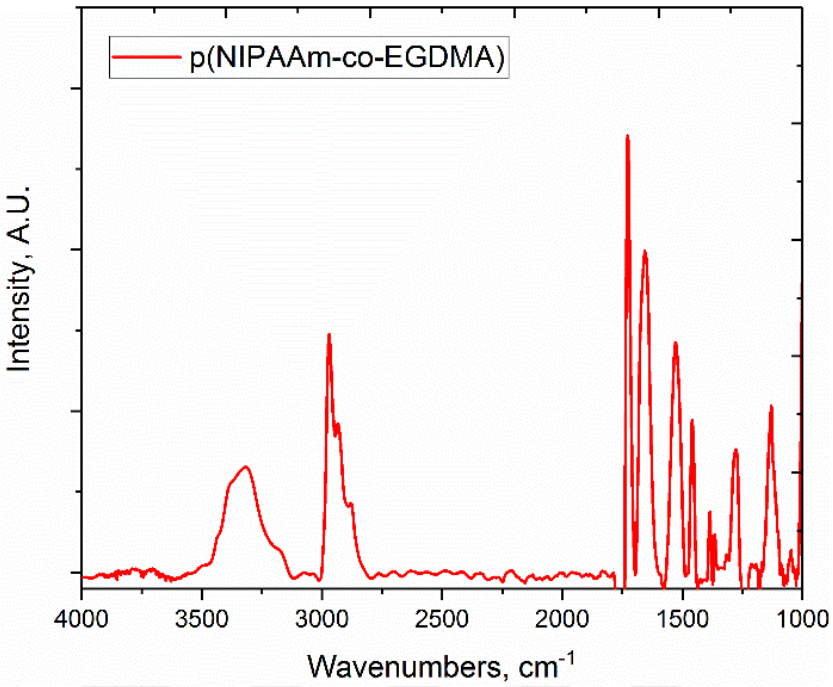

Figure 7.2. FTIR spectra of the p(NIPAAm-co-EGDMA) coating on AAO template

The monomer to crosslinker ratio can be calculated according to the area analysis beneath the C=O stretching peak responsible for NIPAAm and EGDMA according to the relationship [147, 148]:

$$\frac{\text{EGDMA}}{\text{NIPAAm}} = \frac{(A_{C=O}/2)_{\text{EGDMA}}}{(A_{C=O})_{\text{NIPAAm}}} \tag{7.1}$$

Area for EGDMA is divided by two since in EGDMA structure there are two C=O bonds. According to the calculation the amount of crosslinker in the NIPAAm film is 30%.

Figure 7.3 shows the SEM images of the prepared membranes including AAO templates deposited conformally with p(NIPAAm-co-EGDMA) the negatively charged AuNPs are attached on the top and on the walls inside the membrane pores.

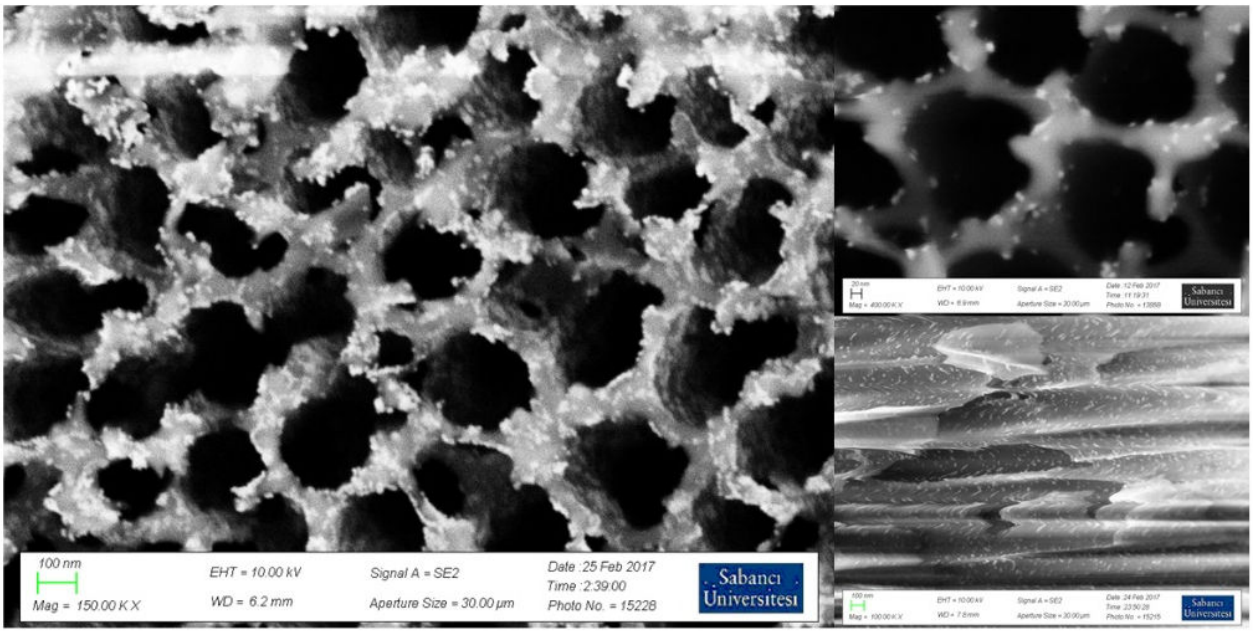

Figure 7.3. SEM image of the p(NIPAAm-co-EGDMA) coating on AAO template and attached AuNPs on a) the membrane top b) large scale the membrane top c) the walls of membrane pores

Figure 7.4 shows the EDS analysis of the prepared membranes. Elemental analysis shows gold distributes on the top and walls of the membrane.

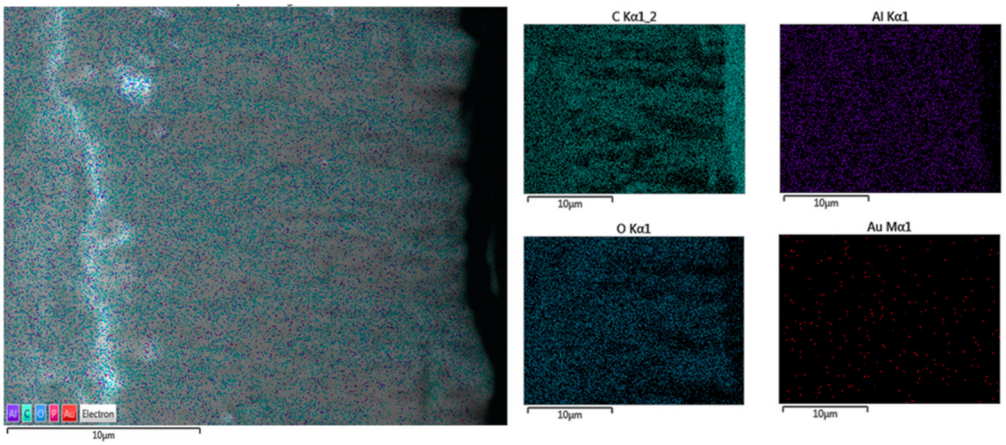

Figure 7.4. EDS analysis of the membrane. Carbon, aluminum, oxygen and gold distribution in the membrane

Free COO^- groups of adsorbed citrate on the surface of gold nanoparticles corresponds to the negative charge of citrate-capped AuNPs [149, 150]. When the membranes are immersed inside the solution of negatively charged citrate-capped AuNPs, the positively charged N-H groups in

NIPAAm electrostatically interacts with some negatively charged COO^- groups in citrate-capped AuNPs [151, 152] and other free COO^- groups give negative charge to the membrane according to Figure 7.5.

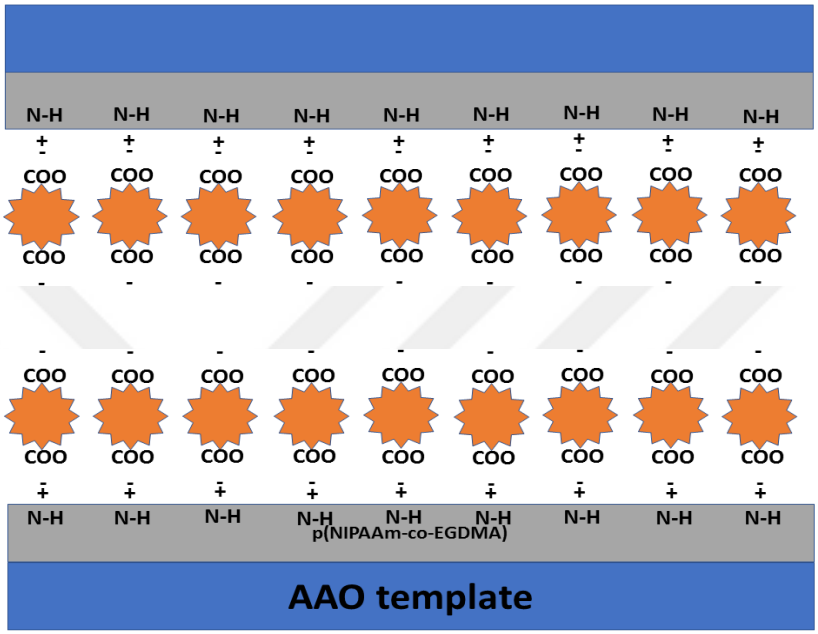

Figure 7.5. Negatively charged citrate-capped AuNPs electrostatically attached to p(NIPAAm-co-EGDMA)

Hb and HSA have nearly the same size, since their molecular weights close each other (Hb 56 kDa and HAS 66 kDa) but their isoelectric points are different i.e. Hb (pl=6.8) and HSA (pl=4.6) where their surface total charge at this pH is neutral [135] but at pH values below pl the protein total charge is positive and at pH values above pl the protein total charge is negative. Figure 7.6 shows diffusion of Hb and HSA proteins through the p(NIAPAAm-co-EGDMA) and p(NIPAAm-co-EGDMA)-Au^- (negatively charged AuNPs attached) membranes at pH 3 where the total charge of both proteins is positive. For both membranes diffusion of Hb is more than HSA. The radius of Hb and HSA is the same thus other factors should affect the proteins diffusion through the membranes.

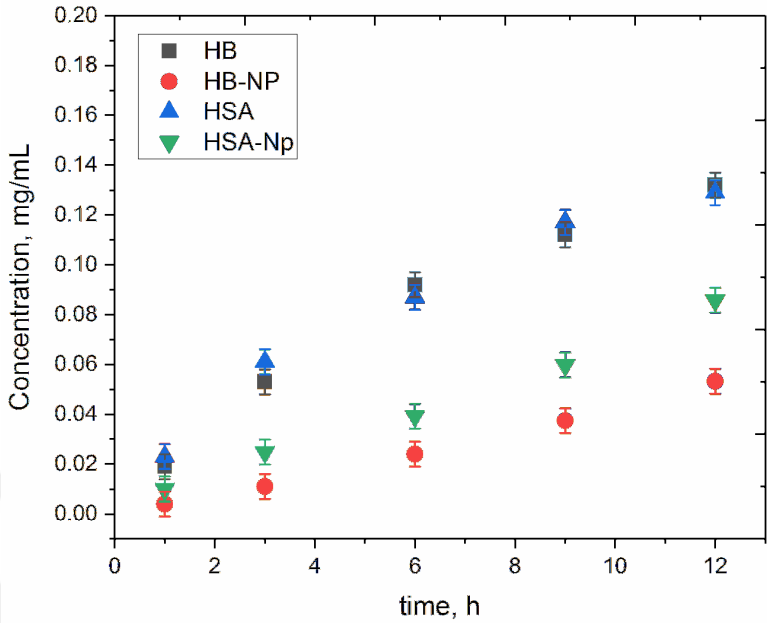

Figure 7.6. Single diffusion of Hb and HSA through p(NIPAAm-co-EGDMA) and p(NIPAAm-co-EGDMA)-Au- at pH 3

The mobility, molecular shape, isoelectric point, and the hydrophilic to hydrophobic ratio of amino acids are important factors that play a role in transport inside nanochannels [109, 153, 154]. The hydrophilic-to-hydrophobic ratio of the amino acids within HSA is 56%, but for Hb this value is 44% [119], therefore HSA is more hydrophilic than Hb. Moreover, the surface and pore walls of the membrane are more hydrophilic according to monomer to crosslinker ratio calculation which is 30% for p(NIPAAm-co-EGDMA) therefore, considering this factor HSA diffusion through the membrane should be more than Hb, while the diffusion rate for both proteins is nearly the same. For nanosize hydrodynamic radius, the surface area to volume ratio and diffusion coefficient of molecules depends on their shape [155] and diffusion coefficient of spheres is more than the diffusion coefficient of cylinders. Hb shape is spherical while HSA has cylindrical shape and according to this conformation, diffusion of Hb is faster than HSA. (in bulk the diffusion coefficient for Hb and HSA is $6.4*10^{-11}$ m^2/s and HSA $5.9*10^{-11}$ m^2/s, respectively [119]). The diffusion rate for Hb and HSA through p(NIPAAm-co-EGDMA) at pH3 is nearly the same hence it seems, more hydrophilicity of BSA than Hb and higher diffusion coefficient of Hb than HSA compensate each other's effects thus causing the diffusion of a single protein through the membranes to be the same. Proteins are large molecules and therefore can be heavily charged [156] therefore strong electrostatic interactions between a protein and charged membrane should occur.

The protein diffusion rates for p(NIPAAm-co-EGDMA)-Au^- is less than uncharged membrane because of attraction of electrostatic interaction between positively charged proteins and negatively charged membranes, consequently electrostatic repulsion of proteins counterions [119]. In this state, the diffusion of Hb is more than HSA probably only diffusion coefficient factor is more important than hydrophilicity factor. Moreover, the average radius of AuNPs is 13.6nm, so the pore size for p(NIPAAm-co-EGDMA)-Au^- membrane is less than p(NIPAAm-co-EGDMA), which can be observed from the water flux plots. (Figure 7.7). Figure 7.8 shows diffusion of Hb and HSA proteins through the p(NIAPAAm-co-EGDMA) and p(NIPAAm-co-EGDMA)-Au^- membranes at pH9 where the total charge of both proteins is negative. Hb and HSA diffusion in p(NIPAAm-co-EGDMA) is nearly the same because of competition of diffusion coefficient and hydrophilicity factors in Hb and HAS [119, 155]. For p(NIPAAm-co-EGDMA)-Au^- membrane, diffusion of HSA is higher than Hb because of protein structure. The electrostatic repulsion between the pore walls and the HSA, the ellipsoid shaped molecule aligns its long axis with axis of the pores but sphere shaped Hb interacts without any alignments inside the pores [119, 135]. Thus, HSA diffuses faster than Hb through the membrane. On the other hand, because of less pore diameter and more interactions, diffusion through p(NIAPAAm-co-EGDMA)-Au^- is slower than p(NIPAAm-co-EGDMA). In comparison with pH3 state, the diffusion rate for both the membranes is higher at pH9. For p(NIPAAm-co-EGDMA) membrane at pH3, the amine groups of NIPAAm is more positive causing the electrostatic reactions between the proteins and the membranes, while at pH9 protonation of N-H groups of NIPAAm is less, therefore less electrostatic interactions promote higher diffusion. For p(NIPAAm-co-EGDMA)-Au^-, it seems that the repulsion between negatively charged AuNPs and proteins, prevents the attraction of proteins to the pore walls.

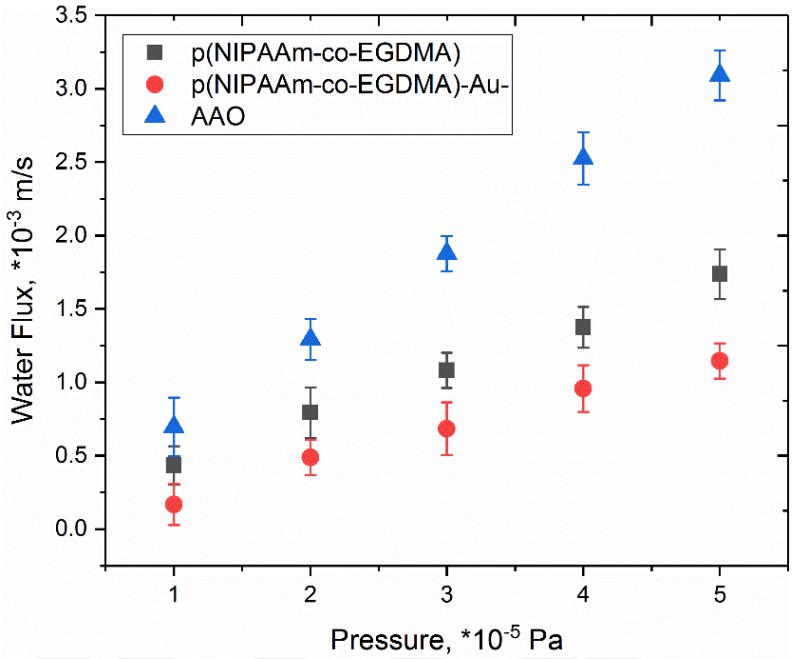

Figure 7.7. Water permeability of uncoated AAO template, p(NIPAAm-co-EGDMA) coated AAO and p(NIPAAm-co-EGDMA)-Au- coated AAO

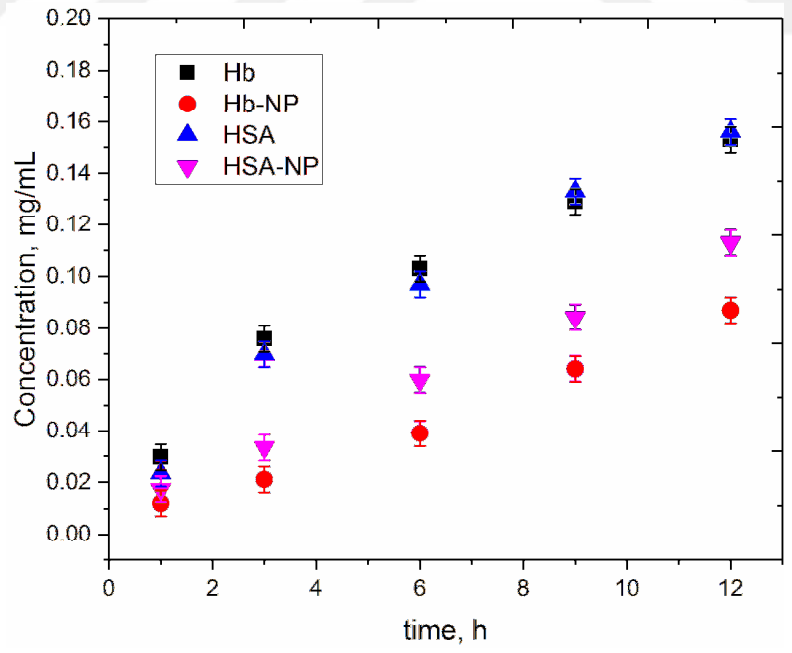

Figure 7.8. Single diffusion of Hb and HSA through p(NIPAAm-co-EGDMA) and p(NIPAAm-co-EGDMA)-Au- at pH 9

Figure 7.9 (a) shows diffusion of a mixture of Hb and HSA at pH values 4.7 (pI of HSA) and 6.8 (pI of Hb) for p(NIPAAm-co-EGDMA) and p(NIPAAm-co-EGDMA)-Au^{-}. For both membranes the diffusion rates of HSA and Hb has decreased. Transport phenomena of mixed proteins are more complex than the single protein, and interactions between the proteins is more complicated even at isoelectric point of the protein. At the isoelectric point of a protein, even though the total charge of the protein is zero, there are positive and negative components that electrostatically interact each other. These positive and negative segments, interact with other charged protein and result in a decrease in the proteins flux [119]. At pH4.7, diffusion of HSA is faster for both membranes because the net charge of HSA is zero and there is less interaction between the membrane and the proteins but less diffusion for p(NIPAAm-co-EGDMA)-Au^{-} which is attributed to smaller pore size of this membrane (Figure 7.7). There is less diffusion for Hb because of its interaction with the membrane especially with the negatively charged one. The electrostatic attraction of Hb and the membrane leading to absorption of Hb then repulsion of counterions causes its diffusion rate to decrease. In addition, again the pore size of the membranes should be considered.

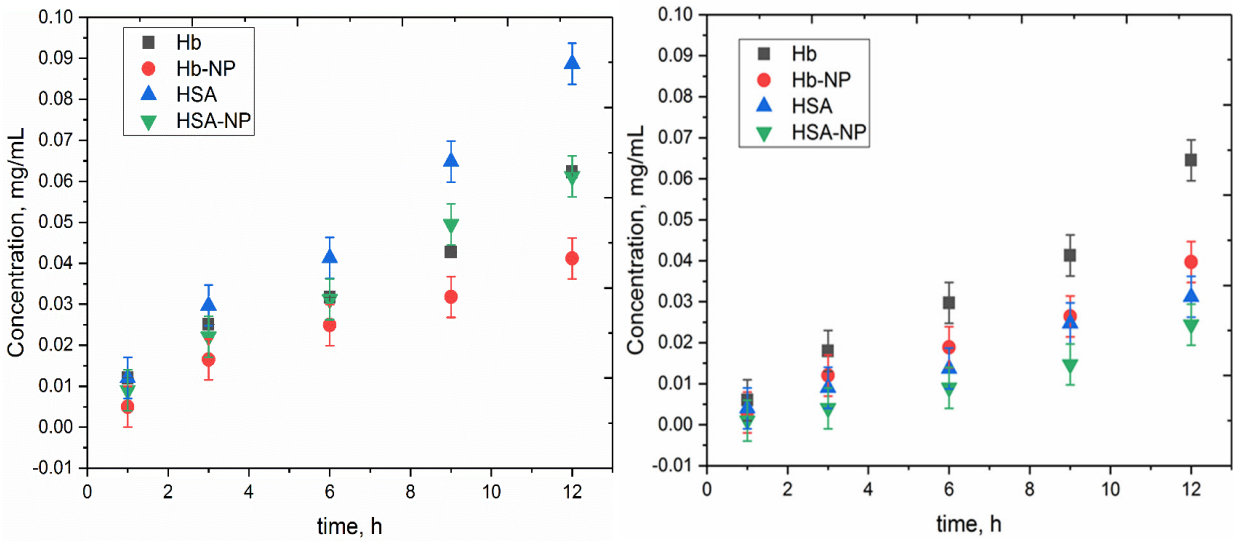

Figure 7.9. Mixed diffusion of Hb and HSA through p(NIPAAm-co-EGDMA) and p(NIPAAm-co-EGDMA)-Au- a) at pH 4.7 b) at pH6.8

At pH6.8, diffusion of Hb is more than HSA for both membranes because of less interactions between the proteins and the membranes (Figure 7.9 (b)). HSA diffusion in p(NIPAAm-co-EGDMA)-Au^- is less than p(NIPAAm-co-EGDMA) for various reasons. The first, the pore size of p(NIPAAm-co-EGDMA) is bigger than charge attached ones. The second, at pH6.8 p(NIPAAm-co-EGDMA) is less protonated so its charge is not important while for p(NIPAAm-co-EGDMA)-Au^-, there are significant repulsion interactions between the proteins and the membrane.

CHAPTER 8. CONCLUSIONS

The main goal of this thesis was to prepare different types of membranes by using vapor polymerization methods to improve the permeability and selectivity of membranes by using functional polymers. Free-standing polymer membranes, double-layered membranes and membranes with functional pores were produced using smart polymers. The separation performance of the membranes was tested under low and high pressures using dye molecules and proteins.

Ultra-thin, free standing hydrogel membranes were prepared to study the permeation of dyes with different size and hydrophilicity. Crosslinker ratio and temperature was shown to have significant impact on the permeation and separation of model dyes.

Hybrid membranes fabricated by coating the pores of commercially available AAO templates were shown to have a great impact on the permeability and selectivity due to stimulation of the membrane.

In the macromolecule studies carried out with proteins and nanoparticles it has been shown that integration of pH responsive smart polymers in separation membranes enabled the control of flux and prevented the proteins from adhering. This control could be further enhanced by preparing Janus membranes with dual pH response on opposite sides. The Janus membranes allowed the control of the flux and release of proteins by opening and closing the gates via changing the pH.

In addition to the pore size, shape of the nanochannels played a significant role in controlling the protein diffusion and selectivity, in the case when the radii of the channels were comparable to the protein size. Selectivity of the membranes could further be improved to separate proteins with similar sizes by attaching charged nanoparticles on the pore walls. These composite membranes, not only improved the selectivity of the membranes, but also reduced protein adhesion, preventing biofouling of the membranes.

Bibliography

1. Taylor, A.W., et al., *High vacuum distillation of ionic liquids and separation of ionic liquid mixtures.* Physical Chemistry Chemical Physics, 2010. **12**(8): p. 1772-1783.
2. Opekar, F., P. Coufal, and K. Stulik, *Rapid Capillary Zone Electrophoresis Along Short Separation Pathways and Its Use in Some Hyphenated Systems: A Critical Review.* Chemical Reviews, 2009. **109**(9): p. 4487-4499.
3. Gu, H.W., et al., *Biofunctional magnetic nanoparticles for protein separation and pathogen detection.* Chemical Communications, 2006(9): p. 941-949.
4. Napoli, M., J.C.T. Eijkel, and S. Pennathur, *Nanofluidic technology for biomolecule applications: a critical review.* Lab on a Chip, 2010. **10**(8): p. 957-985.
5. Fu, J.P., et al., *A patterned anisotropic nanofluidic sieving structure for continuous-flow separation of DNA and proteins.* Nature Nanotechnology, 2007. **2**(2): p. 121-128.
6. Ulbricht, M., *Advanced functional polymer membranes.* Polymer, 2006. **47**(7): p. 2217-2262.
7. Bernardo, P., E. Drioli, and G. Golemme, *Membrane Gas Separation: A Review/State of the Art.* Industrial & Engineering Chemistry Research, 2009. **48**(10): p. 4638-4663.
8. Saxena, A., et al., *Membrane-based techniques for the separation and purification of proteins: An overview.* Advances in Colloid and Interface Science, 2009. **145**(1-2): p. 1-22.
9. Han, J.Y., J.P. Fu, and R.B. Schoch, *Molecular sieving using nanofilters: Past, present and future.* Lab on a Chip, 2008. **8**(1): p. 23-33.
10. Guillen, G.R., et al., *Pore-structure, hydrophilicity, and particle filtration characteristics of polyaniline-polysulfone ultrafiltration membranes.* Journal of Materials Chemistry, 2010. **20**(22): p. 4621-4628.
11. Uyar, T., et al., *Molecular filters based on cyclodextrin functionalized electrospun fibers.* Journal of Membrane Science, 2009. **332**(1-2): p. 129-137.
12. Tsuru, T., *Nano/subnano-tuning of porous ceramic membranes for molecular separation.* Journal of Sol-Gel Science and Technology, 2008. **46**(3): p. 349-361.
13. Li, F.B., et al., *Precise pore size tuning and surface modifications of polymeric membranes using the atomic layer deposition technique.* Journal of Membrane Science, 2011. **385**(1-2): p. 1-9.
14. Yang, Q., et al., *Composites of functional polymeric hydrogels and porous membranes.* Journal of Materials Chemistry, 2011. **21**(9): p. 2783-2811.
15. Tokarev, I. and S. Minko, *Stimuli-Responsive Porous Hydrogels at Interfaces for Molecular Filtration, Separation, Controlled Release, and Gating in Capsules and Membranes.* Advanced Materials, 2010. **22**(31): p. 3446-3462.
16. Ahn, S.K., et al., *Stimuli-responsive polymer gels.* Soft Matter, 2008. **4**(6): p. 1151-1157.
17. Dai, S., P. Ravi, and K.C. Tam, *pH-Responsive polymers: synthesis, properties and applications.* Soft Matter, 2008. **4**(3): p. 435-449.
18. Schild, H.G., *Poly (N-Isopropylacrylamide) - Experiment, Theory and Application.* Progress in Polymer Science, 1992. **17**(2): p. 163-249.
19. Piskin, E., *Molecularly designed water soluble, intelligent, nanosize polymeric carriers.* International Journal of Pharmaceutics, 2004. **277**(1-2): p. 105-118.
20. Stuart, M.A.C., et al., *Emerging applications of stimuli-responsive polymer materials.* Nature Materials, 2010. **9**(2): p. 101-113.
21. Tanaka, S., et al., *Pervaporation characteristics of pore-filling PDMS/PMHS membranes for recovery of ethylacetate from aqueous solution.* Journal of Membrane Science, 2010. **348**(1): p. 383-388.
22. Velleman, L., J.G. Shapter, and D. Losic, *Gold nanotube membranes functionalised with fluorinated thiols for selective molecular transport.* Journal of Membrane Science, 2009. **328**(1-2): p. 121-126.

23. Song, C.F., et al., *pH-sensitive characteristics of poly(acrylic acid)-functionalized anodic aluminum oxide (AAO) membranes.* Journal of Membrane Science, 2011. **372**(1-2): p. 340-345.
24. Bruening, M.L., et al., *Creation of functional membranes using polyelectrolyte multilayers and polymer brushes.* Langmuir, 2008. **24**(15): p. 7663-7673.
25. Wang, W.C., et al., *Thermally On-Off Switching Membranes Prepared by Pore-Filling Poly(N-isopropylacrylamide) Hydrogels.* Industrial & Engineering Chemistry Research, 2010. **49**(4): p. 1684-1690.
26. Adrus, N. and M. Ulbricht, *Novel hydrogel pore-filled composite membranes with tunable and temperature-responsive size-selectivity.* Journal of Materials Chemistry, 2012. **22**(7): p. 3088-3098.
27. Meng, T., et al., *A thermo-responsive affinity membrane with nano-structured pores and grafted poly(N-isopropylacrylamide) surface layer for hydrophobic adsorption.* Journal of Membrane Science, 2010. **349**(1-2): p. 258-267.
28. Lewis, S.R., et al., *Reactive nanostructured membranes for water purification.* Proceedings of the National Academy of Sciences of the United States of America, 2011. **108**(21): p. 8577-8582.
29. Chen, H.Y., Y. Elkasabi, and J. Lahann, *Surface modification of confined microgeometries via vapor-deposited polymer coatings.* Journal of the American Chemical Society, 2006. **128**(1): p. 374-380.
30. Martin, T.P., et al., *Initiated chemical vapor deposition of antimicrobial polymer coatings.* Biomaterials, 2007. **28**(6): p. 909-915.
31. Li, Y.L., I.A. Kinloch, and A.H. Windle, *Direct spinning of carbon nanotube fibers from chemical vapor deposition synthesis.* Science, 2004. **304**(5668): p. 276-278.
32. Zaharias, G.A., H.H. Shi, and S.F. Bent, *Characterization of polyconjugated thin films synthesized by hot-wire chemical vapor deposition of aniline.* Thin Solid Films, 2006. **501**(1-2): p. 341-345.
33. Pyo, S.W., et al., *Electrical effect in organic thin-film transistors using polymerized gate insulators by vapor deposition polymerization (VDP).* Synthetic Metals, 2005. **154**(1-3): p. 141-144.
34. Strijkova, V., et al., *Electrical properties of a thin layer polyimide matrix.* Journal of Optoelectronics and Advanced Materials, 2005. **7**(3): p. 1319-1322.
35. Green, Z.I., et al., *Morphology of Vapor Deposited Polyimides Containing Copper Phthalocyanine.* Chemical Vapor Deposition, 2009. **15**(4-6): p. 106-111.
36. Roualdes, S. and J. Durand, *Experimental design and modelling in the investigation of PECVD parameters effects on the structural and gas transport properties of plasma polysiloxane membranes.* Journal of Membrane Science, 2004. **230**(1-2): p. 39-48.
37. Dobkin, D.M. and M.K. Zuraw, *Principles of chemical vapor deposition*. 2013: Springer Science & Business Media.
38. Im, S.G., et al., *A Directly Patternable, Click-Active Polymer Film via Initiated Chemical Vapor Deposition.* Macromolecular Rapid Communications, 2008. **29**(20): p. 1648-1654.
39. Lau, K.K.S. and K.K. Gleason, *Particle surface design using an all-dry encapsulation method.* Advanced Materials, 2006. **18**(15): p. 1972-+.
40. Anthamatten, M. and K.K.S. Lau, *Vapor Deposition Polymerization*, in *Encyclopedia of Chemical Processing*. 2008.
41. Forch, R., et al., *Recent and expected roles of plasma-polymerized films for biomedical applications.* Chemical Vapor Deposition, 2007. **13**(6-7): p. 280-294.
42. Hiratsuka, A. and I. Karube, *Plasma polymerized films for sensor devices.* Electroanalysis, 2000. **12**(9): p. 695-702.
43. Pierson, H.O., *Handbook of chemical vapor deposition: principles, technology and applications*. 1999: William Andrew.
44. Choy, K.L., *Chemical vapour deposition of coatings.* Progress in Materials Science, 2003. **48**(2): p. 57-170.

45. Pryce Lewis, H.G., D.J. Edell, and K.K. Gleason, *Pulsed-PECVD films from hexamethylcyclotrisiloxane for use as insulating biomaterials.* Chemistry of materials, 2000. **12**(11): p. 3488-3494.
46. Lau, K.K.S., J.A. Caulfield, and K.K. Gleason, *Structure and morphology of fluorocarbon films grown by hot filament chemical vapor deposition.* Chemistry of Materials, 2000. **12**(10): p. 3032-3037.
47. Limb, S.J., et al., *Growth of fluorocarbon polymer thin films with high CF2 fractions and low dangling bond concentrations by thermal chemical vapor deposition.* Applied Physics Letters, 1996. **68**(20): p. 2810-2812.
48. Gupta, M., et al., *Initiated chemical vapor deposition (iCVD) of conformal polymeric nanocoatings for the surface modification of high-aspect-ratio pores.* Chemistry of Materials, 2008. **20**(4): p. 1646-1651.
49. Ozaydin-Ince, G., A.M. Coclite, and K.K. Gleason, *CVD of polymeric thin films: applications in sensors, biotechnology, microelectronics/organic electronics, microfluidics, MEMS, composites and membranes.* Reports on Progress in Physics, 2012. **75**(1).
50. Im, S.G. and K.K. Gleason, *Solvent-free modification of surfaces with polymers: The case for initiated and oxidative chemical vapor deposition (CVD).* AIChE journal, 2011. **57**(2): p. 276-285.
51. Yamada, B. and P.B. Zetterlund, *Handbook of radical polymerization*. 2002: Wiley-Interscience: Hoboken, NJ.
52. Cruden, B.A., K.K. Gleason, and H.H. Sawin, *Relationship of CF 2 concentration to deposition rates in the pyrolytic chemical vapor deposition process.* Journal of Vacuum Science & Technology B: Microelectronics and Nanometer Structures Processing, Measurement, and Phenomena, 2002. **20**(2): p. 690-695.
53. Lewis, H.G.P., J.A. Caulfield, and K.K. Gleason, *Perfluorooctane sulfonyl fluoride as an initiator in hot-filament chemical vapor deposition of fluorocarbon thin films.* Langmuir, 2001. **17**(24): p. 7652-7655.
54. Lau, K.K. and K.K. Gleason, *Initiated chemical vapor deposition (iCVD) of poly (alkyl acrylates): an experimental study.* Macromolecules, 2006. **39**(10): p. 3688-3694.
55. Lau, K.K.S. and K.K. Gleason, *Initiated chemical vapor deposition (iCVD) of poly(alkyl acrylates): A kinetic model.* Macromolecules, 2006. **39**(10): p. 3695-3703.
56. Bakker, R., et al., *Initiated chemical vapour deposition (iCVD) of thermally stable poly-glycidyl methacrylate.* Surface and Coatings Technology, 2007. **201**(22): p. 9422-9425.
57. Mao, Y. and K.K. Gleason, *Vapor-deposited fluorinated glycidyl copolymer thin films with low surface energy and improved mechanical properties.* Macromolecules, 2006. **39**(11): p. 3895-3900.
58. Tenhaeff, W.E. and K.K. Gleason, *Initiated chemical vapor deposition of perfectly alternating poly(styrene-alt-maleic anhydride).* Surface & Coatings Technology, 2007. **201**(22-23): p. 9417-9421.
59. Jo, W., et al., *Photon to thermal response of a single patterned gold nanorod cluster under near-infrared laser irradiation.* Biofabrication, 2011. **3**(1).
60. Chan, K., et al., *Initiated chemical vapor deposition of polyvinylpyrrolidone-based thin films.* Polymer, 2006. **47**(20): p. 6941-6947.
61. Janakiraman, S., et al., *Kinetic analysis of the initiated chemical vapor deposition of poly(vinylpyrrolidone) and poly(4-vinylpyridine).* Thin Solid Films, 2015. **595**: p. 244-250.
62. O'Shaughnessy, W.S., M.L. Gao, and K.K. Gleason, *Initiated chemical vapor deposition of trivinyltrimethylcyclotrisiloxane for biomaterial coatings.* Langmuir, 2006. **22**(16): p. 7021-7026.
63. Achyuta, A.K.H., et al., *Incorporation of Linear Spacer Molecules in Vapor-Deposited Silicone Polymer Thin Films.* Macromolecules, 2009. **42**(6): p. 1970-1978.
64. Ye, Y.M., et al., *Hybrid structure of pH-responsive hydrogel and carbon nanotube array with superwettability.* Journal of Materials Chemistry, 2012. **22**(6): p. 2449-2455.

65. Bose, R.K., A.M. Heming, and K.K.S. Lau, *Microencapsulation of a Crop Protection Compound by Initiated Chemical Vapor Deposition.* Macromolecular Rapid Communications, 2012. **33**(16): p. 1375-1380.
66. Ozaydin-Ince, G. and K.K. Gleason, *Tunable Conformality of Polymer Coatings on High Aspect Ratio Features.* Chemical Vapor Deposition, 2010. **16**(1-3): p. 100-105.
67. Lau, K.K.S. and K.K. Gleason, *Particle functionalization and encapsulation by initiated chemical vapor deposition (iCVD).* Surface & Coatings Technology, 2007. **201**(22-23): p. 9189-9194.
68. Lau, K.K.S. and K.K. Gleason, *All-dry synthesis and coating of methacrylic acid copolymers for controlled release.* Macromolecular Bioscience, 2007. **7**(4): p. 429-434.
69. Montero, L., et al., *Increasing biosensor response through hydrogel thin film deposition: Influence of hydrogel thickness.* Vacuum, 2012. **86**(12): p. 2102-2104.
70. Tenhaeff, W.E., L.D. McIntosh, and K.K. Gleason, *Synthesis of Poly (4-vinylpyridine) Thin Films by Initiated Chemical Vapor Deposition (iCVD) for Selective Nanotrench-Based Sensing of Nitroaromatics.* Advanced Functional Materials, 2010. **20**(7): p. 1144-1151.
71. Martin, T.P., K. Chan, and K.K. Gleason, *Combinatorial initiated chemical vapor deposition (iCVD) for polymer thin film discovery.* Thin Solid Films, 2008. **516**(5): p. 681-683.
72. Bose, R.K., S. Nejati, and K.K.S. Lau, *Initiated Chemical Vapor Deposition (iCVD) of Hydrogel Polymers.* Eurocvd 17 / Cvd 17, 2009. **25**(8): p. 1229-1235.
73. Nejati, S. and K.K.S. Lau, *Integration of polymer electrolytes in dye sensitized solar cells by initiated chemical vapor deposition.* Thin Solid Films, 2011. **519**(14): p. 4551-4554.
74. Lee, K.P., T.C. Arnot, and D. Mattia, *A review of reverse osmosis membrane materials for desalination-Development to date and future potential.* Journal of Membrane Science, 2011. **370**(1-2): p. 1-22.
75. Louie, J.S., et al., *Effects of polyether-polyamide block copolymer coating on performance and fouling of reverse osmosis membranes.* Journal of Membrane Science, 2006. **280**(1-2): p. 762-770.
76. O'Shaughnessy, W.S., et al., *Stable biopassive insulation synthesized by initiated chemical vapor deposition of poly(1,3,5-trivinyltrimethylcyclotrisiloxane).* Biomacromolecules, 2007. **8**(8): p. 2564-2570.
77. Ma, M.L., et al., *Decorated electrospun fibers exhibiting superhydrophobicity.* Advanced Materials, 2007. **19**(2): p. 255-+.
78. Nejati, S. and K.K.S. Lau, *Pore Filling of Nanostructured Electrodes in Dye Sensitized Solar Cells by Initiated Chemical Vapor Deposition.* Nano Letters, 2011. **11**(2): p. 419-423.
79. Baxamusa, S.H. and K.K. Gleason, *Thin Polymer Films with High Step Coverage in Microtrenches by Initiated CVD.* Chemical Vapor Deposition, 2008. **14**(9-10): p. 313-318.
80. Servi, A.T., et al., *The effects of iCVD film thickness and conformality on the permeability and wetting of MD membranes.* Journal of Membrane Science, 2017. **523**: p. 470-479.
81. Asatekin, A. and K.K. Gleason, *Polymeric Nanopore Membranes for Hydrophobicity-Based Separations by Conformal Initiated Chemical Vapor Deposition.* Nano Letters, 2011. **11**(2): p. 677-686.
82. Matin, A., et al., *Reverse osmosis membranes surface-modified using an initiated chemical vapor deposition technique show resistance to alginate fouling under cross-flow conditions: Filtration & subsequent characterization.* Desalination, 2016. **379**: p. 108-117.
83. Warsinger, D.M., et al., *Combining air recharging and membrane superhydrophobicity for fouling prevention in membrane distillation.* Journal of Membrane Science, 2016. **505**: p. 241-252.
84. Guo, F., et al., *Desalination by Membrane Distillation using Electrospun Polyamide Fiber Membranes with Surface Fluorination by Chemical Vapor Deposition.* Acs Applied Materials & Interfaces, 2015. **7**(15): p. 8225-8232.
85. Günzler, H. and H.U. Gremlich, *IR spectroscopy. An introduction.* 2002.

86. Skoog, D.A., F.J. Holler, and S.R. Crouch, *Principles of instrumental analysis*. 2017: Cengage learning.
87. Tompkins, H.G. and W.A. McGahan, *Spectroscopic ellipsometry and reflectometry: a user's guide*. 1999: Wiley.
88. Stokes, D. and Royal Microscopical Society (Great Britain), *Principles and practice of variable pressure/environmental scanning electron microscopy (VP-ESEM)*. 2008, Chichester, U.K.: Wiley. xii, 221 p.
89. Binnig, G., C.F. Quate, and C. Gerber, *Atomic Force Microscope.* Physical Review Letters, 1986. **56**(9): p. 930-933.
90. Chan, K. and K.K. Gleason, *Initiated chemical vapor deposition of linear and cross-linked poly(2-hydroxyethyl methacrylate) for use as thin-film hydrogels.* Langmuir, 2005. **21**(19): p. 8930-8939.
91. Fineman, M. and S.D. Ross, *Linear method for determining monomer reactivity ratios in copolymerization.* Journal of Polymer Science Part A: Polymer Chemistry, 1950. **5**(2): p. 259-262.
92. Peppas, N.A. and A.G. Mikos, *Preparation methods and structure of hydrogels.* Hydrogels in medicine and pharmacy, 1986. **1**: p. 1-27.
93. Baxamusa, S.H., et al., *Protection of Sensors for Biological Applications by Photoinitiated Chemical Vapor Deposition of Hydrogel Thin Films.* Biomacromolecules, 2008. **9**(10): p. 2857-2862.
94. Xu, M., A.V. Goponenko, and S.A. Asher, *Polymerized polyHEMA photonic crystals: pH and ethanol sensor materials.* Journal of the American Chemical Society, 2008. **130**(10): p. 3113-3119.
95. Toomey, R., D. Freidank, and J. Ruhe, *Swelling behavior of thin, surface-attached polymer networks.* Macromolecules, 2004. **37**(3): p. 882-887.
96. Mukherjee, M., et al., *Power law in swelling of ultra-thin polymer films.* Polymer, 2013. **54**(17): p. 4669-4674.
97. Peppas, N.A., H.J. Moynihan, and L.M. Lucht, *The Structure of Highly Crosslinked Poly(2-Hydroxyethyl Methacrylate) Hydrogels.* Journal of Biomedical Materials Research, 1985. **19**(4): p. 397-411.
98. Bose, R.K. and K.K.S. Lau, *Mechanical Properties of Ultrahigh Molecular Weight PHEMA Hydrogels Synthesized Using Initiated Chemical Vapor Deposition.* Biomacromolecules, 2010. **11**(8): p. 2116-2122.
99. Wijmans, J.G. and R.W. Baker, *The Solution-Diffusion Model - a Review.* Journal of Membrane Science, 1995. **107**(1-2): p. 1-21.
100. Mika, A.M. and R.F. Childs, *Calculation of the hydrodynamic permeability of gels and gel-filled microporous membranes.* Industrial & Engineering Chemistry Research, 2001. **40**(7): p. 1694-1705.
101. Ren, C.L., R.J. Nap, and I. Szleifer, *The Role of Hydrogen Bonding in Tethered Polymer Layers.* Journal of Physical Chemistry B, 2008. **112**(50): p. 16238-16248.
102. Igathinathane, C., et al., *Shape identification and particles size distribution from basic shape parameters using ImageJ.* Computers and Electronics in Agriculture, 2008. **63**(2): p. 168-182.
103. Swift, T., et al., *The pH-responsive behaviour of poly(acrylic acid) in aqueous solution is dependent on molar mass.* Soft Matter, 2016. **12**(9): p. 2542-2549.
104. Zhang, W.F., et al., *Primary and tertiary amines bifunctional graphene oxide for cooperative catalysis.* Nanoscale, 2013. **5**(13): p. 6030-6033.
105. Chen, Y., et al., *Stable dispersions of graphene and highly conducting graphene films: a new approach to creating colloids of graphene monolayers.* Chemical Communications, 2009(30): p. 4527-4529.

106. Peeva, P.D., et al., *Performance of Thin-Layer Hydrogel Polyethersulfone Composite Membranes during Dead-End Ultrafiltration of Various Protein Solutions.* Industrial & Engineering Chemistry Research, 2012. **51**(21): p. 7231-7241.
107. Boributh, S., A. Chanachai, and R. Jiraratananon, *Modification of PVDF membrane by chitosan solution for reducing protein fouling.* Journal of Membrane Science, 2009. **342**(1-2): p. 97-104.
108. Vatanpour, V., et al., *Fabrication and characterization of novel antifouling nanofiltration membrane prepared from oxidized multiwalled carbon nanotube/polyethersulfone nanocomposite.* Journal of Membrane Science, 2011. **375**(1-2): p. 284-294.
109. Musale, D.A. and S.S. Kulkarni, *Relative rates of protein transmission through poly(acrylonitrile) based ultrafiltration membranes.* Journal of Membrane Science, 1997. **136**(1-2): p. 13-23.
110. Asatekin, A., et al., *Anti-fouling ultrafiltration membranes containing polyacrylonitrile-graft-poly (ethylene oxide) comb copolymer additives.* Journal of Membrane Science, 2007. **298**(1-2): p. 136-146.
111. Huisman, I.H., P. Pradanos, and A. Hernandez, *The effect of protein-protein and protein-membrane interactions on membrane fouling in ultrafiltration.* Journal of Membrane Science, 2000. **179**(1-2): p. 79-90.
112. Sinha, M.K. and M.K. Purkait, *Preparation and characterization of novel pegylated hydrophilic pH responsive polysulfone ultrafiltration membrane.* Journal of Membrane Science, 2014. **464**: p. 20-32.
113. Tu, Q., et al., *Effects of surface charges of graphene oxide on neuronal outgrowth and branching.* Analyst, 2014. **139**(1): p. 105-115.
114. Xiao, W.M., et al., *Anchoring H3PW12O40 on 3-aminopropyltriethoxysilane modified graphene oxide: enhanced adsorption capacity and photocatalytic activity toward methyl orange.* New Journal of Chemistry, 2015. **39**(5): p. 3719-3727.
115. Hu, X.B., et al., *Effects of particle size and pH value on the hydrophilicity of graphene oxide.* Applied Surface Science, 2013. **273**: p. 118-121.
116. Shih, C.J., et al., *Understanding the pH-Dependent Behavior of Graphene Oxide Aqueous Solutions: A Comparative Experimental and Molecular Dynamics Simulation Study.* Langmuir, 2012. **28**(1): p. 235-241.
117. Jachimska, B. and A. Pajor, *Physico-chemical characterization of bovine serum albumin in solution and as deposited on surfaces.* Bioelectrochemistry, 2012. **87**: p. 138-146.
118. Barbosa, L.R.S., et al., *The Importance of Protein-Protein Interactions on the pH-Induced Conformational Changes of Bovine Serum Albumin: A Small-Angle X-Ray Scattering Study.* Biophysical Journal, 2010. **98**(1): p. 147-157.
119. Chun, K.Y. and P. Stroeve, *Protein transport in nanoporous membranes modified with self-assembled monolayers of functionalized thiols.* Langmuir, 2002. **18**(12): p. 4653-4658.
120. Bayari, S. and S. Yurdakul, *Fourier transform infrared and Raman spectra of 4-vinylpyridine and its transition metal(II) tetracyanonickelate complexes.* Spectroscopy Letters, 2000. **33**(4): p. 475-483.
121. Wu, K.H., Y.R. Wang, and W.H. Hwu, *FTIR and TGA studies of poly(4-vinylpyridine-co-divinylbenzene)-Cu(II) complex.* Polymer Degradation and Stability, 2003. **79**(2): p. 195-200.
122. Fogler, H.S., *Elements of chemical reaction engineering*. 1999, New Jersey: Prentice-Hall International London.
123. Belfiore, L.A., *Transport phenomena for chemical reactor design*. 2003, New York: J. Wiley. xxv, 884 p.
124. Wang, Y., et al., *Highly swellable ultrathin poly(4-vinylpyridine) multilayer hydrogels with pH-triggered surface wettability.* Soft Matter, 2013. **9**(39): p. 9420-9429.
125. Shevate, R., et al., *Polyanionic pH-responsive polystyrene-b-poly(4-vinyl pyridine-N-oxide) isoporous membranes.* Journal of Membrane Science, 2016. **501**: p. 161-168.

126. Nunes, S.P., et al., *Switchable pH-Responsive Polymeric Membranes Prepared via Block Copolymer Micelle Assembly.* Acs Nano, 2011. **5**(5): p. 3516-3522.
127. Nunes, S.P., et al., *From Micelle Supramolecular Assemblies in Selective Solvents to Isoporous Membranes.* Langmuir, 2011. **27**(16): p. 10184-10190.
128. Sun, W., et al., *Surface-active isoporous membranes nondestructively derived from perpendicularly aligned block copolymers for size-selective separation.* Journal of Membrane Science, 2014. **466**: p. 229-237.
129. McInnes, S.J.P., et al., *Combination of iCVD and Porous Silicon for the Development of a Controlled Drug Delivery System.* Acs Applied Materials & Interfaces, 2012. **4**(7): p. 3566-3574.
130. Moni, P., A. Al-Obeidi, and K.K. Gleason, *Vapor deposition routes to conformal polymer thin films.* Beilstein Journal of Nanotechnology, 2017. **8**: p. 723-735.
131. Chien, M.C., G.J. Wang, and W.C. Yu, *Modeling ion diffusion current in nanochannel using infinitesimal distribution resistor-capacitor circuits.* Japanese Journal of Applied Physics Part 1-Regular Papers Brief Communications & Review Papers, 2007. **46**(11): p. 7436-7440.
132. Schoch, R.B., H. van Lintel, and P. Renaud, *Effect of the surface charge on ion transport through nanoslits.* Physics of Fluids, 2005. **17**(10).
133. Smalley, J.F., M.D. Newton, and S.W. Feldberg, *An informative subtlety of itemperature-jump or coulostatic responses for surface-attached species.* Electrochemistry Communications, 2000. **2**(12): p. 832-838.
134. Gervasi, C.A., et al., *Electron transfer across anodic films formed on tin in carbonate-bicarbonate buffer solution.* Electrochimica Acta, 2005. **50**(5): p. 1113-1119.
135. Qiu, X.Y., H.Z. Yu, and K.V. Peinemann, *Selective separation of similarly sized proteins with tunable nanoporous block copolymer membranes.* Euromembrane Conference 2012, 2012. **44**: p. 461-463.
136. Colvin, J.R., *The size and shape of lysozyme.* Canadian Journal of Chemistry, 1952. **30**(11): p. 831-834.
137. Yang, S.Y., et al., *Single-File Diffusion of Protein Drugs through Cylindrical Nanochannels.* Acs Nano, 2010. **4**(7): p. 3817-3822.
138. Kukla, V., et al., *NMR studies of single-file diffusion in unidimensional channel zeolites.* Science, 1996. **272**(5262): p. 702-704.
139. Lutz, C., M. Kollmann, and C. Bechinger, *Single-file diffusion of colloids in one-dimensional channels.* Physical Review Letters, 2004. **93**(2).
140. Wei, Q.H., C. Bechinger, and P. Leiderer, *Single-file diffusion of colloids in one-dimensional channels.* Science, 2000. **287**(5453): p. 625-627.
141. Koepke, J.A., J.F. Thoma, and R.M. Schmidt, *Identification of human hemoglobins by use of isoelectric focusing in gel.* Clinical chemistry, 1975. **21**(13): p. 1953-1955.
142. Price, W.S., F. Tsuchiya, and Y. Arata, *Lysozyme aggregation and solution properties studied using PGSE NMR diffusion measurements.* Journal of the American Chemical Society, 1999. **121**(49): p. 11503-11512.
143. Huang, X., B.R. Nayak, and T.L. Lowe, *Synthesis and characterization of novel thermoresponsive-co-biodegradable hydrogels composed of N-isopropylacrylamide, poly (L-lactic acid), and dextran.* Journal of Polymer Science Part A: Polymer Chemistry, 2004. **42**(20): p. 5054-5066.
144. Martins, G.V., J.F. Mano, and N.M. Alves, *Dual responsive nanostructured surfaces for biomedical applications.* Langmuir, 2011. **27**(13): p. 8415-8423.
145. Maeda, Y., T. Higuchi, and I. Ikeda, *Change in hydration state during the coil- globule transition of aqueous solutions of poly (N-isopropylacrylamide) as evidenced by FTIR spectroscopy.* Langmuir, 2000. **16**(19): p. 7503-7509.
146. Gao, F.X., et al., *A pH and temperature dual-responsive macroporous molecularly imprinted cryogel for enhanced recognition capability towards ovalbumin.* Analytical Methods, 2013. **5**(23): p. 6700-6708.

147. Alf, M.E., T.A. Hatton, and K.K. Gleason, *Novel N-isopropylacrylamide based polymer architecture for faster LCST transition kinetics.* Polymer, 2011. **52**(20): p. 4429-4434.
148. Alf, M.E., et al., *Sharp hydrophilicity switching and conformality on nanostructured surfaces prepared via initiated chemical vapor deposition (iCVD) of a novel thermally responsive copolymer.* Macromolecular rapid communications, 2010. **31**(24): p. 2166-2172.
149. Yuce, M., et al., *Employment of nanomaterials in polymerase chain reaction: insight into the impacts and putative operating mechanisms of nano-additives in PCR.* RSC Advances, 2014. **4**(69): p. 36800-36814.
150. Park, J.W. and J.S. Shumaker-Parry, *Structural study of citrate layers on gold nanoparticles: role of intermolecular interactions in stabilizing nanoparticles.* Journal of the American Chemical Society, 2014. **136**(5): p. 1907-1921.
151. Rani, M., et al., *Understanding the mechanism of replacement of citrate from the surface of gold nanoparticles by amino acids: a theoretical and experimental investigation and their biological application.* RSC Advances, 2016. **6**(21): p. 17373-17383.
152. Zare, D., A. Akbarzadeh, and N. Bararpour, *Synthesis and functionalization of gold nanoparticles by using of poly functional amino acids.* International Journal of Nanoscience and Nanotechnology, 2010. **6**(4): p. 223-230.
153. Küpcü, S., M. Sára, and U.B. Sleytr, *Influence of covalent attachment of low molecular weight substances on the rejection and adsorption properties of crystalline proteinaceous ultrafiltration membranes.* Desalination, 1993. **90**(1): p. 65-76.
154. Van den Berg, G.B. and C.A. Smolders, *Concentration polarization phenomena during dead-end ultrafiltration of protein mixtures. The influence of solute-solute interactions.* Journal of membrane science, 1989. **47**(1): p. 1-24.
155. Ozaydin-Ince, G., et al., *Microworm optode sensors limit particle diffusion to enable in vivo measurements.* Proceedings of the National Academy of Sciences, 2011. **108**(7): p. 2656-2661.
156. Pujar, N.S. and A.L. Zydney, *Electrostatic effects on protein partitioning in size-exclusion chromatography and membrane ultrafiltration.* Journal of Chromatography A, 1998. **796**(2): p. 229-238.